

Multimodality Photoacoustic and Raman Imaging

by

Wei Shi

A thesis submitted in partial fulfillment of the requirements for the degree of

Doctor of Philosophy

in

Biomedical Engineering

Department of Electrical and Computer Engineering
University of Alberta

© Wei Shi, 2014

Abstract

Tumor metastasis is referred to the spread of cancer from one to another unadjacent part of the body, which results in more than 90% of tumor deaths, and however is still poorly understood. Circulating tumor cells (CTCs) have been proposed as an important biomarker of tumor metastasis. Many approaches have been developed for detection of CTCs, but each has its own advantages and disadvantages. With the aid of nanoparticles (NPs), photoacoustic detection along with efficient magnetic enrichment of CTCs demonstrated high sensitivity. However, differentiation of photoacoustic signals is non-trivial hence specificity can be poor. Surface-enhanced-Raman-scattering (SERS) NPs were used for detection of CTCs with high multiplexing capability. However, the lack of enrichment of CTCs limits its application for *in vivo* detection. High sensitivity and high specificity *in vivo* methods of detecting CTCs are in urgent need. A hallmark signature of metastasis is angiogenesis, the proliferation of vessel networks growing from pre-existing vasculature. Imaging angiogenesis is important for cancer research since angiogenesis is regarded as a necessity for tumor growth and tumor metastasis. Photoacoustic imaging (PAM) is a promising technique for imaging angiogenesis due to intrinsic high optical contrast between blood and tissues, and high spatial resolution at adequate penetration depth. Optical-resolution photoacoustic imaging (OR-PAM) pushed the lateral resolution limit of PAM to micron or submicron level, which enables imaging of single capillaries, the finest vasculature elements. However, the low imaging speed of OR-PAM may limit its application in the clinic, and for practical pre-clinical imaging of animal models.

A single modality tool for studies on tumor metastasis is unlikely to be able to fulfill these needs. Therefore, the long term goal of this dissertation is to develop a multimodality imaging tool for imaging tumor metastasis and detecting of CTCs with high specificity and high sensitivity.

Specially, we focused on the approach of combing PAM with a Raman imaging technology for this purpose. For the task of detecting CTCs, the photoacoustic subsystem could aid in placement of a magnet for trapping of such CTCs and gaging the flow rate for optimal optical and multiplexed detection with the Raman sub-system. The photoacoustic sub-system could also be used for detecting absorption signatures from nanoparticles on tumor cells. For detecting metastases, the Raman imaging subsystem could be used to detect multiple flavors of nanoparticles targeted to (non-circulating) tumor cells and the photoacoustic sub-system could be used to detect neoplasm angiogenesis.

We aimed to push limits of OR-PAM imaging frame-rate, to develop a novel CTC detection technique with high sensitivity and high specificity, and to further build a multimodality photoacoustic-Raman imaging tool for high sensitivity and high specificity molecular imaging.

Our work presented in this dissertation can be divided into three parts. First, we worked on developing realtime OR-PAM using various high pulse repetition rate lasers and combined with a fast optical scanning galvanometer mirror systems. We reported the first near realtime volumetric OR-PAM with 4 frames per second (fps) imaging speed and $\sim 6 \mu\text{m}$ lateral resolution by employing a fiber laser with up to 600 kHz pulse repetition rate. Further, we demonstrated *in vivo* near realtime sustained OR-PAM imaging of dynamic process and 30 fps realtime imaging of cardiac-induced microhemodynamics in murine microvasculature. In addition, we studied the scanning speed dependence of photoacoustic signals which may lead to a super-resolution technique in the future. Second, we demonstrated for the first time the magnetic enrichment and detection of CTCs in circulating PBS or rat blood with high specificity and high sensitivity by targeting tumor cells with both SERS NPs and magnetic NPs (MNPs). Third, we presented a multimodality imaging

system consisting of PAM and SERS imaging which may advance the research of tumor metastasis in the future.

Preface

Chapter 3 of this thesis has been published as W. Shi, S. Kerr, I. Utkin, J. C. Ranasinghesagara, L. Pan, Y. Godwal, R. J. Zemp, and R. Fedosejevs, “Optical resolution photoacoustic microscopy using novel high-repetition-rate passively Q-switched microchip and fiber lasers,” *J. Biomed. Opt.* 15, 056017 (2010). I was responsible for the experiment design, data collection and the manuscript composition. S. Kerr contributed to experiments, data analysis, and the manuscript composition. I. Utkin, J. C. Ranasinghesagara, L. Pan, and Y. Godwal contributed to experiment design and contributed to manuscript edits. R. Fedosejevs and R. J. Zemp were the supervisory authors and were involved with concept formation and manuscript composition.

Chapter 4 of this thesis has been published as W. Shi, P. Hajireza, P. Shao, A. Forbrich, and R. J. Zemp, “*In vivo* near-realtime volumetric optical-resolution photoacoustic microscopy using a high-repetition-rate nanosecond fiber-laser,” *Opt. Express* 19, 17143(2011). I was responsible for the experiment design, data collection, data analysis and the manuscript composition. P. Hajireza and P. Shao contributed to experiments and manuscript edits. A. Forbrich contributed to data processing and manuscript edits. R. J. Zemp was the supervisory author and was involved with concept formation and manuscript composition.

Chapter 5 of this thesis has been published as W. Shi, P. Shao, P. Hajireza, A. Forbrich, and R. J. Zemp, “*In vivo* dynamic process imaging using real-time optical-resolution photoacoustic microscopy”, *J. Biomed. Opt.* 18, 026001 (2013). I was responsible for the experiment design, data collection, data analysis and the manuscript composition. P. Shao contributed to experiments and manuscript edits. P. Hajireza contributed to experiment design and manuscript edits. A. Forbrich contributed to data processing and manuscript edits. R. J. Zemp was the supervisory authors and was involved with concept formation and manuscript composition.

Chapter 6 of this thesis has been published as W. Shi, P. Shao, and R. J. Zemp, “Investigation of Photoacoustic Signal Strength as a Function of Scan-Speed and Laser-Repetition-Rate”, 2013 Joint UFFC, EFTF and PFM Symposium, 1534 (Prague, 2013). I was responsible for the experiment design, data collection, data analysis and the manuscript composition. P. Shao contributed to experiments and manuscript edits. R. J. Zemp was the supervisory author and was involved with concept formation and manuscript composition.

Chapter 7 of this thesis has been published as W. Shi, R. J. Paproski, R. Moore, and R. J. Zemp, “Detection of circulating tumor cells using targeted surface-enhanced Raman scattering nanoparticles and magnetic enrichment”, *Journal of Biomedical Optics* 19(5), 056014, (2014). I was responsible for the experiment design, data collection, data analysis and the manuscript composition. R. J. Paproski contributed to experiment design and manuscript edits. R. Moore and R. J. Zemp were the supervisory authors and were involved with concept formation and manuscript composition.

Chapter 8 of this thesis has been published as W. Shi, P. Shao, R. J. Paproski, A. Forbrich, R. Moore, and R. J. Zemp, “Multimodality photoacoustic and Raman imaging of magnetically-trapped tumor cells”, *Proc. SPIE* 8943, 894367 (SPIE Photonics West, San Francisco, 2014). I was responsible for the experiment design, data collection, data analysis and the manuscript composition. P. Shao contributed to experiments and manuscript edits. R. J. Paproski contributed to experiment design and manuscript edits. A. Forbrich contributed to data collection and manuscript edits. R. Moore and R. J. Zemp were the supervisory authors and were involved with concept formation and manuscript composition.

In vivo experiments procedures involving animals described in Chapter 4, 5 and 8 in this dissertation followed the laboratory animal protocol approved by the University of Alberta Animal Use and Care Committee.

Acknowledgements

First of all, a huge “thank you” to my supervisor, Dr. Roger J. Zemp for his guidance, encouragement, patience, and support during my doctoral program. It has been a real pleasure to work with him, approaching compelling research problems with frequent insights. Thanks for his being always patient and encouraging, and his selfless dedication to both my personal and academic development. I also admire his ability to balance research interest and personal pursuits, which sets an example for me.

Special thanks are given to Dr. Robert Fedosejevs and Dr. Ray Decorby, my supervisory committee members for their helpful suggestion and critical comments, which lead me to the improvement on the weakness of my dissertation.

Also, I would like to sincerely acknowledge our collaborator Dr. Ronald Moore from Faculty of Medicine, for his great help and support on my research. Thanks also go to Dr. Hua Chen and Ivy Ma from Dr. Ronald Moore’s lab for their kindly help from the experimental perspective.

Furthermore, I am deeply thankful to my co-authors: Shaun Kerr, Ilya Utkin, Janaka Ranasinghesagara, Lei Pan, Yogesh Godwal, Roger J. Zemp, Robert Fedosejevs, Parsin Hajireza, Peng Shao, Alexander Forbrich, Robert J. Paproskia, and Ronald Moore, for their insight, help, support and valuable input in my publications.

Additionally, I appreciate the help and support from people in the Department of Electrical and Computer Engineering, especially Pinder Bains, Wing Hoy, Rick McGregor, Herbert Dixel, Kathleen Forbes and Linda Jiao.

Many thanks to the University of Alberta, and the Department of Electrical and Computer Engineering for their academic and technical support, to Prostate Cancer Canada Movember Discovery Grant, NSERC, Terry- Fox Foundation and the Canadian Cancer Society, the Alberta Cancer Research Institute, Leaders Opportunity Fund, the Alberta Cancer Board, the Canada Foundation for Innovation, Leaders Opportunity Fund, Microsystems Technology Research Initiative, University of Alberta Startup Funds, Alberta Advanced Education & Technology, MPB Technologies Inc., Small Equipment Grants Program, Alberta Ingenuity and Alberta Innovates scholarships for graduate students, Canadian Federation of University Women Edmonton Margaret Brine Graduate Scholarships for Women, IEEE UFFC Travel Support, SPIE Optics and Photonics Education Scholarship and FGSR Travel Awards, for their generous support and financial assistance.

I am also thankful to my colleagues in our lab not mentioned above: Yan Jiang, Huihong Lu, Tyler Harrison, Peiyu Zhang, Alex Sampaleanu, Ryan Chee, and Tarek Kaddoura, for their support and companionship.

In addition, I would like to express my heartfelt gratitude to my friends for providing constant support and spiritual encouragement.

And finally, but not least, I am profoundly indebted to my whole family, especially my parents, my husband, my son and my brother. Their unconditional care, love and support have been an important and indispensable source of spiritual support.

Contents

1. Introduction.....	1
1.1 Metastasis and angiogenesis in cancer.....	1
1.2 Problem statement and motivation.....	1
1.2.1 Imaging angiogenesis.....	1
1.2.2 Detection of circulating tumor cells.....	2
1.2.3 Long-term vision and goal of this dissertation	3
1.3 Major contributions for this dissertation	5
1.3.1 Realtime optical-resolution photoacoustic microscopy (OR-PAM).....	5
1.3.2 CTC detection	6
1.3.3 Multimodality imaging with PAM and SERS detection.....	6
1.4 Organization of this dissertation	7
Bibliography.....	9
2. Background.....	13
2.1 Angiogenesis and metastasis.....	13
2.1.1 Angiogenesis.....	13
2.1.2 Progress on angiogenesis imaging.....	14
2.1.3 Metastasis.....	16
2.1.4 Progress on detection of circulating tumor cells.....	17
2.2 Optical resolution photoacoustic imaging.....	18
2.2.1. Photoacoustic wave generation	18
2.2.2. Photoacoustic Imaging	20
2.2.3. Optical resolution photoacoustic microscopy.....	22
2.2.4. Challenges of OR-PAM.....	23
2.3. Detection of circulating tumor cells.....	24
2.3.1. Photoacoustic detection of CTCs	24
2.3.2. SERS detection of CTCs	25
2.3.3. Folate targeting.....	28
2.3.4. Challenge of detecting circulating tumor cells	29
Bibliography.....	30

3. Optical resolution photoacoustic microscopy using novel high-repetition-rate passively Q-switched microchip and fiber lasers	46
3.1 Introduction	46
3.2 Methods.....	47
3.2.1 Probe design.....	47
3.2.2 Experimental setup with microchip laser.....	50
3.2.3 Passively Q-switched fiber laser experimental setup.....	52
3.3 Results	53
3.3.1 Microchip laser experimental results	53
3.3.2 Fiber laser experimental results	55
3.4 Discussion	56
3.5 Conclusion.....	57
Bibliography.....	58
4 <i>In vivo</i> near-realtime volumetric optical-resolution photoacoustic microscopy using a high-repetition-rate nanosecond fiber-laser	60
4.1 Introduction	60
4.2 Methods.....	62
4.3 Results	63
4.4 Discussion	65
Bibliography.....	69
5 <i>In vivo</i> dynamic process imaging using real-time optical-resolution photoacoustic microscopy.....	71
5.1 Introduction.....	71
5.2 Methods.....	72
5.3 Results.....	74
5.4 Discussion	77
5.5 Conclusion.....	79
Bibliography.....	80
6 Investigation of photoacoustic signal strength as a function of scan-speed and laser-repetition-rate	83

6.1	Introduction	83
6.2	Theory	84
6.2.1	Thermal Confinements and Stress Confinements.....	84
6.2.2	Gruneisen Parameter	84
6.2.3	Temperature Rise	85
6.3	Methods.....	85
6.4	Experiments and results	86
6.5	Discussion and conclusion	87
	Bibliography.....	89
7	Detection of circulating tumor cells using targeted surface-enhanced-Raman-scattering nanoparticles and magnetic enrichment	91
7.1	Introduction	91
7.2	Materials and methods	93
7.2.1	Folate receptor targeting	93
7.2.2	MNPs	93
7.2.3	SERS NPs	94
7.2.4	Magnetic trapping system	94
7.2.5	Raman imaging system	95
7.3	Experiments and results	96
7.3.1	Sensitivity	96
7.3.2	Crosstalk	98
7.3.3	Non-specific binding.....	98
7.3.4	Magnetic trapping at 1cm/s mean flow velocity.....	99
7.3.5	Magnetic trapping at different flow velocities.....	102
7.3.6	Detection of discrete trapping events in blood	103
7.4	Discussion	104
7.5	Conclusion.....	106
	Bibliography.....	107
8	Multimodality photoacoustic and Raman imaging of magnetically-trapped tumor cells.....	110

8.1	Introduction	110
8.2	Methods	112
8.2.1	System description	112
8.2.2	Nanoparticles and cell preparation.....	113
8.3	Results	114
8.3.1	System performance.....	114
8.3.2	Phantom studies	114
8.3.3	<i>In vivo</i> experiments	115
8.4	Discussion and conclusions.....	116
	Bibliography.....	117
9.	Conclusion and future prospects.....	119
9.1	Work done in this dissertation.....	119
9.1.1	Realtime OR-PAM.....	119
9.1.2	Detection of CTCs	120
9.1.3	Multimodality imaging system	120
9.2	Possible applications	120
9.3	Direction of future work.....	121
	Appendix	122
	Bibliography.....	124

List of Tables

6.1. Two sets of experimental parameters in our experiments, referred as condition 1 and condition2, corresponding to non-overlapped and overlapped mode respectively.....	86
6.2. Average photoacoustic signals from black tape, human hair and rat blood, under condition 1 and condition 2 respectively.....	87

List of Figures

Chapter 2

2.1. (a) Schematic of the OR-PAM light focusing system (a: condenser lens; b: pinhole; c: microscope objective lens; d: ultrasound transducer; e: correcting lens; f: isosceles prism; g: acoustic lens; h: silicon oil); (b) <i>in vivo</i> image of micro-vasculatures of a nude mouse ear with the OR-PAM system	23
2.2. <i>In vivo</i> magnetic enrichment using two-colour photoacoustic detection of CTCs: either laserbeam incidents near the external magnet or through a hole in the magnet by a fiber-based delivery system.....	24
2.3. Demonstration of deep-tissue multiplexed imaging 24 h after intravenous (i.v.) injection of five unique SERS nanoparticle batches simultaneously. (A) Graph depicting five unique Raman spectra, each associated with its own SERS batch: S420 (red), S421 (green), S440 (blue), S466 (yellow), and S470 (orange). (B) Raman image of liver overlaid on digital photo of mouse, showing accumulation of all five SERS batches accumulating in the liver after 24 h post i.v. injection. Panels below depict separate channels associated with each of the injected SERS nanoparticle batches. Individual colors have been assigned to each channel, and the resulting mixture shows a purple color that represents a mixture of the five SERS nanoparticle batches accumulating simultaneously.....	27
3.1. (a) Minimal-loss probe design (OL: objective lens, P: prism, IMF: index-matching fluid, UST: ultrasound transducer, M: ~25- μm -thick Saran Wrap membrane, F: focal point of both light and ultrasound). Ultrasound transducer faces a downfacing optical prism such that photoacoustic signals directed upwards to the prism's diagonal will be deflected to the transducer. An optical index-matching fluid ensures that light can be focused without refraction at the prism's diagonal interface, and provides a low acoustic-loss medium for acoustic signal propagation. (b) Computed curve of acoustic power reflection coefficient C_w (i.e. fraction of incident power reflected) versus incident angle of ultrasound signal on prism. This calculation was made using the acoustic impedances of the fused silica and index-matching fluid media, as based on the speed of sound in, and density of, these materials. Vertical dashed lines represent the acceptance angles of our transducer (about the optical or acoustic axis).....	48
3.2. To study the effects of the prism-index-fluid layer of Fig.3.1 on the potential optical focusing power of the system, we performed a ray-tracing simulation. We simulated a doublet lens ($f = 18$ mm, $\lambda = 532$ nm) focusing a top-hat beam through a 1-cm prism-index-fluid slab with air between the lens and the slab. The dashed curve is the spot size at the focus versus input beam diameter. The solid curve represents the spot size possible according to diffraction theory if no aberrating layer were present. The intersection of the curves represents a region where diffraction-limited performance is possible.....	49

3.3 (a) Experiment setup for the photoacoustic imaging system employing our microchip laser (ML: microchip laser, DL: diode pump laser, L1: 8-mm lens, L2: 11-mm lens, A: Nd:Cr:YAG microchip, F1: long-pass filter blocking 808 nm pump light, L3: 10-cm lens, M: mirror, L4: 10-cm lens, KTP: KTP frequency-doubling crystal, L5: 30-cm lens, G: glass, PD: photodiode, F2: short-pass filter blocking 1064 nm light, SM: scanning mirror, OL: objective lens, Pr: imaging probe, UST: ultrasound transducer). A diode-pumped Nd: Cr: YAG Micro-chip laser is frequency-doubled by a KTP frequency doubling crystal to 532 nm output. (b) Photograph of the fast-scanning mirror, objective lens, and imaging probe.....50

3.4. (a) Experimental setup for the photoacoustic imaging system employing a fiber laser (PL: pump laser, Fb: fiber, L1:11-mm lens, DM1: dichroic mirror reflecting 1075 nm light, L2:8-mm lens, DF: Yb-doped single mode fiber, L3:6.24-mm lens, L4:15-mm lens, SA: saturable absorber, L5:15-mm lens, HRM: high reflectivity mirror, L6:10-cm lens, KTP: KTP frequency-doubling crystal, DM2: dichroic mirror reflecting 537 nm light, L7:15-cm lens, SM: scanning mirror, OL: objective lens, Pr: imaging probe, UST: ultrasound transducer). A Yb-doped fiber of ~6.5 μm mode diameter with an external saturable absorber is pumped by a 976 nm diode laser. The 1075 nm output pulses are coupled out of the laser using a dichroic mirror, and then frequency-doubled with a KTP crystal. The minimal-loss probe with a 10-MHz ultrasound transducer was used for photoacoustic signal detection. (b) Fiber laser signals as measured by a fast photodiode and oscilloscope: 250 ns pulse duration, 100 kHz repetition rate.....52

3.5. Photoacoustic signals (circles) at 1.5 mm depth below the probe membrane with Gaussian fits (lines) (a) in clear water, FWHM = 7.9 μm, amplitude = 1.9 V; (b) in turbid medium with $\mu_s' = 3.33\text{cm}^{-1}$, FWHM = 11.3 μm, amplitude = 1.2 V; (c) in turbid medium with $\mu_s' = 6.67\text{cm}^{-1}$, FWHM = 7.5 μm, amplitude = 0.9 V.....54

3.6 Optical resolution as a function of full width at half maximum (FWHM) of measured photoacoustic signal. This plot was generated by taking the convolution of a 2D Gaussian with a rectangle (simulating the beam spot and carbon fiber, respectively). The photoacoustic FWHM is larger than the corresponding beam FWHM due to the non-zero width (7 – 8 μm) of the carbon fiber targets; the true optical resolution of the system is found to be 7 μm for the measured photoacoustic FWHM of 9 μm.....55

Fig.3.7. Edge-spread function of photoacoustic signal from graphite foil; lateral 10% - 90% PA resolution is $15\pm 5\mu\text{m}$55

4.1. Experiment setup for the photoacoustic imaging system with focused transducer (FL: fiber laser; FLD: fiber laser driver; RM: high reflectivity mirror; GS: glass slide; PD: photodiode; FG1, FG2: function generator; DX, DY: galvanometer scanning mirror driver; SM1, SM2: scanning mirror; OL: 18-mm objective lens; P: prism; IF: index-matching fluid; M: membrane; UST: ultrasound transducer; Amp: amplifier). A diode-pumped pulsed Ytterbium fiber laser generates

532 nm output. A glass slide was inserted to reflect some light into high speed photodiode detector. We used 2D fast scanning mirrors and an objective lens to realize scanning and focusing. We used a uniquely designed minimal-loss probe with a 10 MHz ultrasound transducer (US-TX) for photoacoustic signal detection.....63

4.2. (a) Image of a human hair; (b) Image of a 7.5- μm carbon fiber target positioned 1.5 mm below the probe membrane; (c) Photoacoustic signal (circles) of a slice of data selected perpendicular to the carbon fiber on 2D image with Gaussian fit (line) in clear water, FWHM = 9 μm65

4.3. (a) *in vivo* image of microvasculature in a Swiss Webster mouse ear acquired at 2 fps, which shows an image of a pair of parallel arteries or veins surrounded by capillaries; Video 1 shows the volumetric visualization of the Swiss Webster mouse ear microvasculatures by OR-PAM; (b) Another *in vivo* image of microvasculature in a Swiss Webster mouse ear; Video 2 shows corresponding volumetric visualization of the Swiss Webster mouse ear microvasculature.....66

5.1. Experiment setup of the real-time OR-PAM system (FL: fiber laser; RM: high reflectivity mirror; GS: glass slide; PD: photodiode; SM1, SM2: scanning mirror; DX, DY: galvanometer scanning mirror driver; FG: 2-channel function generator; DAQ: data acquisition card; OL: 18-mm objective lens; P: prism; IF: index-matching fluid; M: membrane; UST: ultrasonic transducer; Amp: amplifier; HSD: high speed digitizer).....74

5.2. (a) An *in vivo* image of micro-vasculatures obtained from a hairless SCID mouse ear to demonstrate the imaging capability of our imaging system; (b) A snapshot from the *in vivo* movie composed of 41 frame 1mm \times 1mm images of microvasculature in a SCID hairless mouse ear when the mouse was in a vertical movement; video 1 displays at 2fps while the actual system frame rate is about 0.5 fps; some small capillaries come out and disappear during the vertical translation.....75

5.3. (a) A snapshot from the *in vivo* movie composed of 42 frame 250 μm \times 250 μm images of microvasculature in a SCID hairless mouse ear acquired at 30 fps; video 2 displays at 15 fps, while microvasculature motions and blood intensity changes are clear to see. (b) Mean photoacoustic signal amplitude inside the dash box A indicated area in (a) versus time. (c) Mean photoacoustic signal amplitude inside the dash box B and C indicated area in (a) respectively versus time.....76

6.1. Experiment setup (FL: fiber laser; RM: high reflectivity mirror; GS: glass slide; PD: photodiode; SM1, SM2: scanning mirror; DX, DY: galvanometer scanning mirror driver; FG: 2-channel function generator; DAQ: data acquisition card; OL: 18-mm objective lens; P: prism; IF: index-matching fluid; UST: ultrasonic transducer; A: amplifier; HSD: high speed digitizer)... 86

7.1 Diagrammatic representations of the conjugated (a) MNP and (b) SERS NP. PEG, polyethylene glycol; Mal, maleimide; FA, folate.....93

7.2 Schematic diagram of Raman imaging system.....	95
7.3 Linearity of estimated SERS NP concentration with actual SERS NP concentration.....	96
7.4 Sensitivity of detected SERS NP.....	97
7.5 Photograph setup used to measure maximum penetration depth.....	97
7.6 Detection of S440 and S421 SERS NPs mixed with concentration ratio of 1:3.....	98
7.7 SERS signal due to 780 nm excitation wavelength from HeLa cells incubated with medium only, HeLa cells incubated with SERS NPs in medium, HeLa cells incubated with folate targeted SERS NPs in medium, ZR-75-1 cells incubated with medium only, ZR-75-1 cells incubated with SERS NPs in medium, and ZR-75-1 cells incubated with folate targeted SERS NPs in medium, respectively.....	99
7.8 SERS spectrum from HeLa cells targeted with both SERS NPs and MNPs at different magnetic trapping time for 1cm/s flow velocity inside 1-mm diameter Tygon tubing.....	100
7.9 Estimated SERS NP concentration at focal zone detected at different magnetic trapping time for 1cm/s flow velocity inside 1-mm diameter Tygon tubing. Three types of cell preparation were made: HeLa cells incubated with SERS NPs only, HeLa cells incubated with MNPs only, and HeLa cells incubated with both SERS NPs and MNPs, respectively.....	101
7.10 Estimated SERS NP concentration at focal zone detected at different magnetic trapping time for different labelled cell concentrations	102
7.11 Discrete events observed in SERS signals from low cell concentration samples.....	102
7.12 Relationship between estimated SERS NP concentrations in focal zone and cell concentrations, at magnetic trapping time of 900 seconds and 1200 seconds respectively.....	103
7.13 Estimated SERS NP concentration at focal zone detected from HeLa cells targeted with both folate-conjugated SERS NPs and MNPs as a function of magnetic trapping time inside 1-mm diameter Tygon tubing for different flow velocities.....	103
7.14 Estimated SERS NP concentration at focal zone detected from HeLa cells targeted with both SERS NPs and MNPs at different magnetic trapping time mixed with 10 ml rat blood inside 1-mm diameter Tygon tubing.....	104
8.1. Schematic diagram of photoacoustic and Raman imaging system.....	112
8.2. Diagrammatic figures of the conjugated (a) SERS NP and (b) MNP. PEG, polyethylene glycol; Mal, maleimide; FA, folate.....	113

8.3 Co-registered image with pseudo-color showing 2mm×2mm image of rat blood with targeted HeLa cells floating inside a 200- μ m inner-diameter acrylic capillary tubing. Signal intensity is normalized. PAM and SERS signals are shown in red and blue color maps, respectively.....115

8.4 Co-registered image with pseudo-color showing 2mm×2mm image of rat ear subcutaneous injected with HeLa cells bound with SERS NPs and MNPs. Signal intensity is normalized. PAM and SERS signals are shown in red and blue color maps, respectively.....115

1. Introduction

1.1 Metastasis and angiogenesis in cancer

Tumor metastasis is the spread of cancer cells from one organ or part of the body to another non-adjacent organ or tissue, which accounts for more than 90% of tumor death [1]. A critical event during metastasis is the transportation of tumor cells through blood vessels to reach a distant site. These tumor cells, therefore, are called circulating tumor cells (CTCs). Detection of CTCs is an important way to understand the biology of tumor metastasis and may be developed into a useful tool for cancer prognosis and treatment. In this dissertation we develop multimodality imaging tools to study metastases and CTCs.

CTCs and metastases often have unique biomarker signatures which can be targeted with imaging agents and nanoparticles (NPs). One focus of this dissertation will be to develop multiplexed targeting strategies to provide specific detection of CTCs and to non-invasively image these biomarker profiles in metastases. Besides unique biomarker profiles, metastases often possess another hallmark signature: angiogenesis.

Angiogenesis is referred to the biological process whereby new blood vessels form from pre-existing vasculature [2]. It occurs in embryogenesis, wound healing and menstrual cycle in ovaries, but otherwise rarely happens in healthy status [3]. However, angiogenesis is well-appreciated as a necessity to tumor growth and progression [4]. Without the independent blood network providing nutrients and oxygen and removing waste products, the growth of solid tumors is limited to a few millimeters due to the equilibrium between the tumor cell proliferation and apoptosis [4][5]. Imaging angiogenesis is of great importance for cancer diagnosis, therapy and understanding the cancer biology process.

1.2 Problem statement and motivation

1.2.1 Imaging angiogenesis

A variety of modalities have been used for imaging angiogenesis includes x-ray computed tomography (CT), magnetic resonance imaging (MRI), positron emission tomography (PET), ultrasound imaging, optical imaging [6]. CT imaging is capable of imaging blood flow, blood

volume and vessel permeability [7]. However, the radiation exposure limits the CT imaging applications especially for children [8]. MRI is a non-ionizing imaging technique which provides anatomic and functional information of angiogenesis with excellent temporal resolution. The spatial resolution of MRI can reach 80 ~100 μm resolution which, however, is still not enough for imaging capillaries of several microns [9]. PET is a quantitative angiogenesis imaging tool with high sensitivity to picomolar concentration tracer molecules, while its spatial resolution is poor compared to CT or MRI [10-11]. Ultrasound imaging can be used for imaging tumor vasculatures at low cost, however, with low spatial resolution compared to CT and MRI [12]. Optical imaging is able to provide structural and functional imaging of angiogenesis based on bioluminescence or light absorption differences, which however, is limited to restricted field of view (FOV) and imaging depth due to strong optical scattering in tissue [13-15].

Photoacoustic imaging has emerged as a promising technique combining the virtues of ultrasound imaging and optical imaging, which is able to provide higher contrast imaging of blood vasculature compared to ultrasound imaging, with higher spatial resolution and deeper imaging depth compared to optical imaging [16-18]. Recently developed optical-resolution photoacoustic microscopy (OR-PAM) pushed the lateral resolution limit of photoacoustic imaging to micron or submicron levels, enabling the imaging of single capillaries [19]. However, low imaging speeds limit the applications of OR-PAM in diagnosis, therapy and biological studies [20].

1.2.2 Detection of circulating tumor cells

There are several approaches used to detect CTCs: nucleic-acid based methods, physical-property based methods and immunological approaches [21][22]. The specificity of nucleic-acid methods is poor for distinguishing a true positive signal from strong background noise [23]. The approaches based on physical properties meet the challenge of variations of heterogeneous CTC sizes in clinical specimens [22]. CellSearch system (VeridexTM, Warren, PA) is a FDA (Food and Drug Administration)-approved method using antibodies against cell surface antigens to enrich and capture CTCs, which is however, limited by its low sensitivity [24-26].

In vivo detection of CTCs is difficult due to its low concentration (1- 10 CTCs per mL) in blood stream with millions of white blood cells and almost 1 billion red blood cells per mL [27]. Recently, photoacoustic detection of magnetically captured CTCs *in vivo* was reported by using

NPs to target cell surface antigens [28][29]. However, this approach was based on photoacoustic signals, hence lacked specificity. Detecting CTCs by using surface-enhanced-Raman-scattering (SERS) NPs was demonstrated with potentially high multiplexing capability [30]. However, *in vivo* detection was not reported due to lack of enrichment of CTCs.

1.2.3 Long-term vision and goal of this dissertation

The long-term goal of this dissertation is to develop multi-modality multiplexed optical and photoacoustic imaging tools for detecting CTCs and imaging metastases. A major shortcoming of many previous efforts to detect tumor cells amidst a deluge of other cells is specificity of detection. To address this problem we proposed the idea that multiple species of surface-enhanced Raman scattering NPs could be targeted to different cancer-upregulated cell surface receptors on CTCs or metastases. The SERS NPs offer unique spectral fingerprints and have previously been shown to have high multiplexing capability while being largely immune to tissue autofluorescence and photobleaching. Because spectral linewidths are narrow and signals from these NPs are bright, SERS NPs avoid spectral overlap problems encountered in fluorescence imaging and offer imaging at several mm depth in biological tissues. The long term goal is to use the high multiplexing abilities of these SERS NPs for detecting multiple cell markers to improve detection specificity. Improved detection specificity could lead to improved diagnostic tests for cancer to enable personalized medicine since these CTCs can reveal much about tumor phenotypes and provide valuable biomarker information that clinicians can use for tailoring therapeutic regimens. For example, in breast cancer it is critical to know whether tumors are positive for Estrogen Receptor, Progesterone Receptor, and HER2, yet the biomarker profiles of CTCs and metastases may vary significantly from the primary tumor. Such biomarkers can also reveal much about prognosis and predict the aggressiveness of the cancer. This too is important to know as a more aggressive and timely treatment may be chosen if the tumor is aggressive in nature. The ability to use CTCs as a source of biomarkers is already a reality in clinical research but progress is limited by the ability to detect small numbers of CTCs in blood with high sensitivity and specificity. Additionally we lack sensitive and specific tools for imaging and detecting these CTCs even in preclinical research using animal models.

We envision multiple imaging and sensing modalities as being critical for detecting CTC and metastasis and imaging their microenvironment and biomarker profiles. In this dissertation we focus on photoacoustic and Raman imaging tools for this purpose. Photoacoustic imaging is an emerging hybrid bio-imaging technology that offers high contrast high-resolution imaging with optical absorption as the primary contrast mechanism. As the dominant absorbing chromophores in tissue are oxy- and deoxy-hemoglobin (the red pigment in red-blood cells) photoacoustic imaging can produce exquisite images of the microcirculation, can quantify oxygen saturation of hemoglobin for functional imaging, and can be used to image blood flow. Exogenous contrast agents can be used including NPs to provide additional signal contrast. These agents can be targeted to bind to cell receptors to provide molecular information. In this dissertation we focus on one hallmark of tumor metastases: angiogenesis (the growth of new blood vessels). We develop imaging systems with the capability to image superficial vasculature for the purpose of imaging angiogenesis in metastatic neoplasms and for the purpose of visualizing the vascular context of CTC or metastasis-targeted NP agents to be imaged with Raman multispectral imaging. The Raman sub-system will be used to image and detect tumor cells targeted with SERS NPs for multiplexed imaging aimed at leading to high specificity and sensitivity. For immobile metastases we envision these SERS NPs targeting the metastasis to reveal its location and biomarker profile non-invasively, with photoacoustic imaging providing the structural and functional vascular context. For CTCs we aim to target the CTCs with not only SERS NPs but also magnetic NPs to enable magnetic trapping and enrichment. The long-term vision is that a patient could wear a magnet to trap CTCs which could then be detected using Raman or photoacoustic methods, with multiplexed multispectral imaging enabling non-invasive biomarker profiling. Trapping could also facilitate extraction of detected CTCs for subsequent genetic profiling using polymerase chain reaction (PCR), ELISAs, or other methods. Some of these molecular biology methods need only a single CTC or a few copies of DNA, mRNA, or miRNA to provide a plethora of information about the CTC phenotype.

The scope of this dissertation does not aim to meet all the objectives in this long-term vision, but rather to further develop the current state-of-the art in multi-modality photoacoustic and Raman imaging and to demonstrate key points of feasibility for the larger vision of tackling metastasis.

1.3 Major contributions for this dissertation

Work described in this dissertation can be divided into the following three parts.

1.3.1 Realtime optical-resolution photoacoustic microscopy (OR-PAM)

- Our work helped to pioneer the use of fiber lasers and microchip lasers for OR-PAM. We demonstrated for the first time using a passively Q-switched fiber laser for OR-PAM, which is quite inexpensive compared with many competing laser architectures, and could be developed into highly compact and rugged systems, offering the advantage of fiber-coupling [31]. Laser repetition rate is a crucial factor affecting the imaging speed. Before our report, typically OR-PAM systems used low laser repetition rate (<1kHz) providing very low frame-rate imaging, which limits clinical utility. Lasers with high repetition rates and suitable pulse durations and energies are not widely available and can be cost-prohibitive and bulky. Present flashlamp-pumped laser systems offer repetition rates of 10-100 Hz while diode-pumped solid-state Q-switched lasers can provide kHz-level repetition rates. These repetition rates are inadequate for real-time frame-rates which are desirable for clinical applications. Since our report in 2010, people started to use high repetition rate fiber lasers and microchip lasers for OR-PAM, which could pave the way of using OR-PAM for many significant clinical and biological applications [32].
- We pioneered high-frame-rate OR-PAM. We first reported near real-time OR-PAM system with ~4 fps 3D imaging and ~6 μm resolution using a commercial fiber laser with up to 600 kHz PRR and a fast, dual mirror optical scanning system [33]. This imaging speed may be adequate for some clinical applications and is one to two orders of magnitude faster than previous systems.
- We developed a fast volumetric, realtime (30 frames per second) OR-PAM system which enables both sustained imaging and real-time imaging [34]. By using this system, we reported *in vivo* label-free reflection-mode real-time OR-PAM imaging of micro-hemodynamics correlated with cardiac pulsations. Before our report, using a high-speed OR-PAM with Au NP-assisted sub-diffraction-limited resolution was reported to achieve *in vivo* imaging of microcirculation in mouse skin at 18 three-dimensional volumes per second [35]. However, the applications of their setup for thick soft tissue is limited due to its configuration working only in transmission mode. Also, NP agents are needed for imaging microcirculation in their system. An immersible MEMS-mirror scanning system capable of high volumetric frame rates was demonstrated [36]. However, they

only demonstrated imaging of carbon particles and red blood cells, but did not correlate microvascular hemodynamics with cardiac pulsations, which could be important in pulse-wave velocity studies and studying tumor hemodynamic pressures. The capabilities of the system may also lead to a future role in functional imaging studies of neuronal-hemodynamic coupling.

- In our realtime OR-PAM studies, we demonstrated the dependence of photoacoustic signal strength on laser repetition rate and scanning speed in OR-PAM system, due to the temperature dependence effects of Gruneisen parameter induced by overlapping of adjacent laser pulses in laser scanning [37]. This technique may be used for improving imaging quality and lead to a novel super-resolution technique in the future. We are developing this work into a journal paper.

1.3.2 CTC detection

- We demonstrated for the first time using both SERS NPs and magnetic NPs (MNPs) to achieve magnetic enrichment and trapping of cancer cells mixed with circulating PBS or blood [38]. Targeted MNPs and SERS probes were used to achieve high sensitive and specific detection of CTCs. Single cell trapping events were indicated by discrete SERS signals detected in the magnetic trapping zone from a mixture of flowing dual-NP labeled HeLa cells and Phosphate buffered saline (PBS) or rat blood. This work could be used in both *ex vivo* and *in vivo* applications. It is important for future SERS-based multiplex detection of CTCs, which and may pave the way to create new tools for cancer research, molecular diagnostics and personal medicine.

1.3.3 Multimodality imaging with PAM and SERS detection

- We first reported a multimodality photoacoustic and Raman imaging system to achieve co-registered PAM and SERS imaging by using both SERS NPs and MNPs [39]. This system presented the virtue of high specificity and multiplexing capabilities due to SERS imaging compared with previously reported PAM. Also, since single modality imaging may be insufficient for efficient metastasis research, combing the structural and functional information of angiogenesis provided by PAM with molecular information inside vasculatures by SERS imaging may be prove a promising technique for further clinical and biology research on tumor metastasis. We are developing this work into a journal paper.

1.4 Organization of this dissertation

The rest of the dissertation is organized as following:

Chapter 2 provides background information on imaging tumor angiogenesis and detection of CTCs, principle of photoacoustic imaging, and literature review on the development of OR-PAM and detection of CTCs. The work presented in this dissertation can be divided into three parts. The first part (chapter 3-6) is focused on real-time OR-PAM. The second part (chapter 7) is focused on techniques for detection of CTCs. The third part (chapter 8) is focused on multimodality imaging system development. Chapter 9 is a summary of contributions, offers conclusions and discusses future work.

Contents of this dissertation (chapter 3 to 8) are drawn from the publications with permissions listed as following:

- [1] W. Shi, S. Kerr, I. Utkin, J. C. Ranasinghesagara, L. Pan, Y. Godwal, R. J. Zemp, and R. Fedosejevs, "Optical resolution photoacoustic microscopy using novel high-repetition-rate passively Q-switched microchip and fiber lasers," *J. Biomed. Opt.* 15, 056017(2010).
- [2] W. Shi, P. Hajireza, P. Shao, A. Forbrich, and R. J. Zemp, "*In vivo* near-realtime volumetric optical-resolution photoacoustic microscopy using a high-repetition-rate nanosecond fiber-laser," *Opt. Express* 19, 17143(2011).
- [3] W. Shi, P. Shao, P. Hajireza, A. Forbrich, and R. J. Zemp, "*In vivo* dynamic process imaging using real-time optical-resolution photoacoustic microscopy", *J. Biomed. Opt.* 18, 026001 (2013)
- [4] W. Shi, P. Shao, and R. J. Zemp, "Investigation of Photoacoustic Signal Strength as a Function of Scan-Speed and Laser-Repetition-Rate", 2013 Joint UFFC, EFTF and PFM Symposium, 1534 (Prague, 2013).
- [5] W. Shi, R. J Paproski, R. Moore, and R. J. Zemp, "Detection of circulating tumor cells using targeted surface-enhanced Raman scattering nanoparticles and magnetic enrichment", *Journal of Biomedical Optics* 19(5), 056014 (2014)
- [6] W. Shi, P. Shao, R. J. Paproski, A. Forbrich, R. Moore, and R. J. Zemp, "Multimodality photoacoustic and Raman imaging of magnetically-trapped tumor cells", *Proc. SPIE* 8943, 894367 (SPIE Photonics West, San Francisco, 2014).

Bibliography

- [1] G. P. Gupta¹ and J. Massagué, “Cancer Metastasis Building a Framework”, *Cell*, vol 127, 680 (2006)
- [2] N. Nishida, H. Yano, T. Nishida, T. Kamura, M. Kojiro, “Angiogenesis in cancer”, *Vascular Health and Risk Management*, vol 2(3), 213–219 (2006)
- [3] A. L. Harris, “Antiangiogenesis for cancer therapy”, *Lancet*, vol 349 (suppl II), 13-15 (1997)
- [4] J. Folkman, “Tumor Angiogenesis”, *Advan. Cancer Res.*, vol 19, 331-357(1974)
- [5] L. Holmgren, MS O'Reilly, J. Folkman, “Dormancy of micrometastases: balanced proliferation and apoptosis in the presence of angiogenesis suppression”, *Nat Med*, vol 1, 149-153 (1995)
- [6] J. C. Miller , H. H. Pien , D. Sahani , A. G. Sorensen, J. H. Thrall, “Imaging Angiogenesis Applications and Potential for Drug Development”, *Journal of the National Cancer Institute*, vol 97, 172 (2005)
- [7] KA Miles, BB Kelley, “CT measurements of capillary permeability within nodal masses: a potential technique for assessing the activity of lymphoma”, *Br J Radio1*, vol 70, 74-79 (1997)
- [8] MS Pearce, JA Salotti, MP Little, et al., “Radiation exposure from CT scans in childhood and subsequent risk of leukaemia and brain tumours: a retrospective cohort study”, *Lancet*, vol 380, (9840), 499–505 (2012)
- [9] M Rudin, PMJ McSheehy, PR Allegrini, M Rausch, D Baumann, M Becquet, et al., “Ptk787/zk222584, a tyrosine kinase inhibitor of vascular endothelial growth factor receptor, reduces uptake of the contrast agent gddota by murine orthotopic b16/bl6 melanoma tumours and inhibits their growth *in vivo*”, *NMR Biomed*, vol 18, 308e321 (2005)
- [10] G. Niu, X. Chen, “PET Imaging of Angiogenesis”, *PET Clin*, vol 4, 17–38 (2009)
- [11] EM Rohren, TG Turkington, RE Coleman, “Clinical applications of PET in oncology”, *Radiology*, vol 231, 305 - 32. (2004)
- [12] W. W. Li, “Tumor Angiogenesis: Molecular Pathology, Therapeutic Targeting, and Imaging”, *Acad Radiol*, vol 7, 800-811 (2000)

- [13] G Vassaux, T. Groot-Wassink, “*In vivo* noninvasive imaging for gene therapy”, J Biomed Biotechnol vol 2003, 92–101 (2003)
- [14] Q Zhu, N Chen, SH Kurtzman, “Imaging tumor angiogenesis by use of combined near-infrared difNSfusive light and ultrasound”, Opt Lett, vol 28, 337–339 (2003)
- [15] EB Brown, RB Campbell, Y Tsuzuki, L Xu, P Carmeliet, D Fukumura, et al., “*In vivo* measurement of gene expression, angiogenesis and physiological function in tumours using multiphoton laser scanning microscopy”, Nat Med, vol 7:,864e868, (2001)
- [16] G. Ku, X. Wang, G. Stoica, and L.-H. Wang, “Multiple-Bandwidth Photoacoustic Tomography”, Phys. Med. Biol., vol 49, 1329-1338 (2004)
- [17] G. Ku, X. Wang, X. Xie, G. Stoica, and L.-H. Wang, “Imaging of tumor angiogenesis in rat brains *in vivo* by photoacoustic tomography”, Appl. Opt., vol 44, 770-775 (2005)
- [18] X. Wang, Y. J. Pang, G. Ku, X. Y. Xie, G. Stoica, and L.-H. V. Wang, “Noninvasive laser-induced photoacoustic tomography for structural and functional *in vivo* imaging of the brain”, Nat. Biotechnol., vol 21, 803-806 (2003).
- [19] K. Maslov, H. F. Zhang, S. Hu and L. H., V., Wang, “Optical-resolution photoacoustic microscopy for *in vivo* imaging of single capillaries”, Opt. Lett. 33, 929-931 (2008)
- [20] S. Hu, K. Maslov, and L. V. Wang, “Second-generation optical-resolution photoacoustic microscopy with improved sensitivity and speed”, Opt. Lett., vol 16, 1134 (2011)
- [21] K. Pantel, R. H. Brakenhoff, and B. Brandt, “Detection, clinical relevance and specific biological properties of disseminating tumour cells”, Nat Rev Cancer, vol 8, 329-40 (2008)
- [22] M. Yu, S. Stott, M. Toner, S. Maheswaran, and D. A. Haber, “Circulating tumor cells: approaches to isolation and characterization”, J. Cell Biol., vol. 192, 373–382 (2011)
- [23] B. Mostert, S. Sleijfer, J. A. Foekens, J. W. Gratama, “Circulating tumor cells (CTCs): Detection methods and their clinical relevance in breast cancer”, Cancer Treatment Reviews, vol 35 463–474 (2009)
- [24] S. Riethdorf, H. Fritsche, V. Müller, T. Rau, C. Schindlbeck, B. Rack, W. Janni, C. Coith, K. Beck, F. Jänicke, et al., “Detection of circulating tumor cells in peripheral blood of patients with

metastatic breast cancer: a validation study of the CellSearch system”, Clin. Cancer Res., vol 13, 920– 928 (2007)

[25] W.J. Allard, J. Matera, M.C. Miller, M. Repollet, M.C. Connelly, C. Rao, A.G. Tibbe, J.W. Uhr, and L.W. Terstappen, “Tumor cells circulate in the peripheral blood of all major carcinomas but not in healthy subjects or patients with nonmalignant diseases”, Clin. Cancer Res., vol 10, 6897–6904 (2004)

[26] G. Attard, J.F. Swennenhuis, D. Olmos, A.H. Reid, E. Vickers, R. A’Hern, R. Levink, F. Coumans, J. Moreira, R. Riisnaes, et al., “Characterization of ERG, AR and PTEN gene status in circulating tumor cells from patients with castration-resistant prostate cancer”, Cancer Res., vol 69, 2912– 2918 (2009)

[27] M. C. Miller, G. V. Doyle, L. W. Terstappen, “Significance of Circulating Tumor Cells Detected by the CellSearch System in Patients with Metastatic Breast Colorectal and Prostate Cancer”, J. of oncology, vol. 2010, 617421, 8 pages, (2010)

[28] E.I. Galanzha, E.V. Shashkov, T. Kelly, J.W. Kim, L. Yang, and V.P. Zharov, “*In vivo* magnetic enrichment and multiplex photoacoustic detection of circulating tumour cells”, Nat. Nanotechnol. vol 4, 855–860 (2009)

[29] E.I. Galanzha, E.V. Shashkov, P.M. Spring, J.Y. Suen, and V.P. Zharov. “*In vivo*, noninvasive, label-free detection and eradication of circulating metastatic melanoma cells using two-color photoacoustic flow cytometry with a diode laser”, Cancer Res., vol 69, 7926–7934 (2009)

[30] X. Wang, X. Qian, J. J. Beitler, G. Chen, F. R. Khuriet, M. M. Lewis, H. J. C. Shin, S. Nie, D. M. Shin, “Detection of Circulating Tumor Cells in Human Peripheral Blood using Surface-Enhanced Raman Scattering Nanoparticles”, Cancer Res., 71(5), 1526–1532 (2011)

[31] W. Shi, S. Kerr, I. Utkin, J. C. Ranasinghesagara, L. Pan, Y. Godwal, R. J. Zemp, and R. Fedosejevs, “Optical resolution photoacoustic microscopy using novel high-repetition-rate passively Q-switched microchip and fiber lasers”, J. Biomed. Opt. 15, 056017(2010).

[32] Y. Wang, K. Maslov, Y. Zhang, S. Hu, L. Yang, Y. Xia, J. Liu, and L. H., V. Wang, “Fiber-laser-based photoacoustic microscopy and melanoma cell detection”, J. Biomed. Opt., vol 16, 011014 (2011)

- [33] W. Shi, P. Hajireza, P. Shao, A. Forbrich, and R. J. Zemp, “*In vivo* near-realtime volumetric optical-resolution photoacoustic microscopy using a high-repetition-rate nanosecond fiber-laser”, *Opt. Express*, vol 19, 17143(2011).
- [34] W. Shi, P. Shao, P. Hajireza, A. Forbrich, and R. J. Zemp, “*In vivo* dynamic process imaging using real-time optical-resolution photoacoustic microscopy”, *J. Biomed. Opt.*, vol 18, 026001 (2013)
- [35] B. Rao, K. Maslov, A. Danielli, R. Chen, K. K. Shung, Q. Zhou, and L. H. V. Wang, “Real-time four-dimensional optical-resolution photoacoustic microscopy with Au nanoparticle-assisted subdiffraction-limit resolution”, *Opt. Lett.* 36(7), 1137-1139 (2011).
- [36] J. Yao, C. H. Huang, L. Wang, J. M. Yang, L. Gao, K. I. Maslov, J. Zou and L. V. Wang, “Wide-field fast-scanning photoacoustic microscopy based on a water-immersible MEMS scanning mirror”, *J. Biomed. Opt.* 17(8), 080505 (2012)
- [37] W. Shi, P. Shao, and R. J. Zemp, “Investigation of Photoacoustic Signal Strength as a Function of Scan-Speed and Laser-Repetition-Rate”, 2013 Joint UFFC, EFTF and PFM Symposium, 1534 (Prague, 2013).
- [38] W. Shi, R. J Paproski, R. Moore, and R. J. Zemp, “Detection of circulating tumor cells using targeted surface-enhanced Raman scattering nanoparticles and magnetic enrichment”, *Journal of Biomedical Optics* 19(5), 056014 (2014)
- [39] W. Shi, P. Shao, R. J. Paproski, A. Forbrich, R. Moore, and R. J. Zemp, “Multimodality photoacoustic and Raman imaging of magnetically-trapped tumor cells”, *Proc. SPIE* 8943, 894367 (SPIE Photonics West, San Francisco, 2014).

2. Background

It was reported by International Agency for Research on Cancer (IARC) of the World Health Organization (WHO) that there were 14.4 million new cancer cases with 8.2 million cancer deaths in 2012 worldwide [1]. Cancer is the second leading cause of death worldwide after cardiovascular diseases, while the annual cancer cases are estimated to rise from 14 million in 2012 to 22 million within the next two decades [1]. The term cancer is usually applied to malignant tumors that are capable of invading into adjacent parts of the body and spreading by invasion and metastasis. The earliest description of cancer can be traced back to about 3000 BC in Egypt [2]. However, till now, the causes, the pathophysiology, the prevention, the diagnosis, and the treatment of cancer are still not clear. Therefore, cancer research is in urgent need for identifying the causes and developing strategies for prevention, diagnosis and treatments.

2.1 Angiogenesis and metastasis

2.1.1 Angiogenesis

It is well-appreciated that solid tumor growth is usually discontinuous which can be divided into avascular stage and vascular stage [3]. In avascular stage without independent blood network supplying nutrients and oxygen and removing waste products, most solid tumors can grow by simple diffusion of oxygen and nutrients from existing vasculature but are restricted to the size of several mm in diameter then die or enter dormancy [4]. The term dormancy here indicates the equilibrium between proliferation and apoptosis of cancer cells or the growth arrest of solidary tumor cells, which may last for months or even years [5]. While in vascular stage, tumor cells expand exponentially and invade tissues locally by stimulating growth of new blood vessels from existing microvessels, which is termed angiogenesis. The purpose of tumor angiogenesis is to obtain sufficient oxygen and nutrients for its rapid growth [6-9].

Angiogenesis was assumed to be induced by hypoxia and possibly a factor associated with low oxygen saturation or inflammation [10]. Hypoxia occurs as a result from deficient vascular supply to meet the perfusion demands of rapidly growing tumors [11][12]. Hypoxia induces gene expression of the angiogenic molecules such as vascular endothelial growth factor (VEGF), fibroblast growth factor (FGF), transforming growth factor- β (TGF- β), platelet-derived growth

factor (PDGF), and others [7]. Sensing the angiogenic signals, activated endothelial cells produce matrix metalloproteinases (MMPs), a special class of enzymes which help degrade the proteins that keep the vessel walls solid [13]. The MMPs break down the basement membrane and extracellular matrix (ECM, support material providing structural and biochemical support around the surrounding cells), permitting the migration of endothelial cells. The permeability of endothelial cell layer increases by VEGF, which enhances trans-endothelial migration and invasion [14]. Subsequently, endothelial cells migrate into surrounding tissues, align in loose groups and begin to divide. Lumen formation occurs by vacuole formation and curving of the endothelial skeleton [6]. Blood flow will start when these sprouts connect [15][16]. Gradually, these sprouts evolve into high-order blood vessels that generate new sprouts, supporting continuous expansion of the tumor vascular bed and tumor mass [17][18].

Angiogenesis seldom occurs in healthy situation, except for embryogenesis, wound healing and the menstrual cycle [19]. However, an increase in angiogenesis happens in many diseases, including cancer. Further, angiogenesis is indispensable for tumor growth and metastasis. Therefore, the understanding of angiogenesis biology, the imaging of angiogenesis, and the development of anti-angiogenic therapies are of great importance for cancer research.

2.1.2 Progress on angiogenesis imaging

There is a clear clinical need for imaging angiogenesis since angiogenesis is an important marker of cancer useful in diagnosis and prognosis [20]. For primary tumors, the microvessel density in localized areas can be used as an independent prognostic factor for overall and disease-free survival [6, 21-28]. Angiogenesis imaging may play a key role in clinical evaluation of the progress of cancer therapy in a sensitive and specific manner [9][29].

There are several modalities mainly used to image angiogenic vasculature: x-ray computed tomography (CT), magnetic resonance imaging (MRI), positron emission tomography (PET), ultrasound imaging, optical imaging and photoacoustic imaging [30]. With contrast agents, CT imaging can be used for imaging blood flow, blood volume and capillary permeability [31]. The introduction of spiral or helical CT in 1990 enabled volumetric imaging, which allowed the capture of transient enhancement of the vascular system after intravenous injection [32][33]. With further development of multidetector CT technique, CT angiography demonstrated its application in

imaging the inflow and out-flux of the entire brain vasculature, the thoracoabdominal aortoiliac system, the lower extremity arterial system, the upper extremity arterial system, and coronary arteries [34-37]. However, higher spatial resolution in CT imaging requires larger radiation dose, the concerns of which limit the growth of CT imaging applications particularly in children [38]. CT primarily is capable of imaging large vessels and cannot resolve capillary networks with acceptable doses.

MRI is capable of anatomic and functional imaging with good temporal and spatial resolution and without ionizing radiation exposure [20]. MRI can be used for providing information about blood volume, blood flow, transendothelial permeability and angiogenesis-specific molecules with or without intravenous contrast agent [39-41]. Rudin et. al, in 2005, demonstrated *in vivo* imaging of tumor vasculature using magnetic resonance imaging (MRI) with 80 ~100 μm resolution[42]. However, the resolution is not high enough for imaging the smallest vascular components - capillaries of several microns.

PET is a quantitative imaging technique which is sensitive to very low concentrations of tracer molecules on the order of picomolars [43]. Moreover, due to short half-life time of many PET radiotracers, PET allows for repetitive imaging over time [43]. However, the spatial resolution of PET is poor compared to CT or MRI [30][44].

Ultrasound imaging is a low cost, portable and widely available technique which can be used for imaging tumor vasculatures [9]. By using microbubbles as contrast agents, ultrasound imaging provides blood volume and perfusion information [45]. Color flow Doppler ultrasound imaging has been used to characterize large tumor vasculature in xenografts in mice and solid tumors in patients [46-48]. 3D power Doppler ultrasound was proved to be able to image oral carcinomas surrounding tissue vasculature in 2007 by Rebol et. al [49][50]. However, the low spatial resolution compared to CT or MRI is a limitation of the application of ultrasound imaging for visualization of small vessels under 100 microns. Optical imaging technologies have been developed to depict tumor physiologic processes in general and angiogenesis in particular [51]. Among them, bioluminescence imaging was used for assessment of angiogenesis through detecting bioluminescent light from internal sources in living tissues [52][53]. Near-infrared light imaging has been used for functional imaging of blood vessel based on the light absorption differences of

oxyhemoglobin and deoxyhemoglobin in near-infrared window. In 2001, Brown et al. reported *in vivo* experiments of using two photon microscopy to analyse physiological signals in tumors, which however, limited to restricted field of view (FOV) and only about 200 μm in depth [54]. Many other confocal and fluorescence microscopy methods, optical coherence tomography methods, and multi-photon microscopy approaches have been used to image microvasculature in model systems and human subjects. Fluorescence approaches require injection of exogenous contrast agents, which is not always desirable. Optical coherence tomography uses Doppler and speckle-tracking methods to image the microvasculature, however, is not sensitive to oxygen saturation of hemoglobin. Optical imaging methods are limited by photon scattering which degrades spatial resolution drastically beyond a mean free path inside tissues [55].

Photoacoustic imaging has been used for imaging angiogenesis with the virtue of high optical contrast between blood and tissue at deeper depths compared with pure optical imaging due to much lower ultrasound scattering than optical scattering in tissue. Photoacoustic tomography was used to perform structural imaging of tumor angiogenesis in brains, and functional imaging of cerebral hemodynamic changes [56-58]. Optical-resolution photoacoustic microscopy (OR-PAM) with micron-level lateral resolution demonstrated its ability to image single capillaries [59]. However, high imaging rates are needed for future clinic applications of OR-PAM. In general, there is no agreement on which method is most suitable for imaging tumor angiogenesis. Some may have advantages over the others for specific disease or information. Also, combined or hybrid imaging technique may be developed in the future.

2.1.3 Metastasis

Tumor metastasis is the spread of cancer cells from one organ or part of the body to another non-adjacent organ or body. Carcinoma metastases are formed by epithelial cells in primary tumors following several biological events: (1) Local invasion: carcinoma cells from primary tumor breach the basement membrane, then invade through surrounding ECM and stromal cell layers, and afterwards enter the adjacent tissue parenchyma; (2) Intravasation: carcinoma cells enter the lumen of lymphatic or blood vessels; (3) Survival in circulation: tumor cells in circulation must overcome a variety of stresses, resist the hemodynamic shear forces and evade capture from the immune system before arriving at distant sites; (4) Arrest at distant organ sites: circulating tumor

cells (CTCs) lodge in the microvessels of distant organs; (5) Extravasation: carcinoma cells penetrate the endothelial cells and pericyte layers, and enter into the tissue parenchyma; (6) Micrometastasis formation: through a complex mechanism, carcinomas modify the microenvironment and cells, and adapt autonomously to foreign tissues so as to survive and form micrometastasis at distant loci; (7) Metastatic Colonization: by overcoming microenvironmental incompatibilities and switching on self-renewal pathways, very few carcinoma cells may be able to reinitiate their proliferative programs at metastatic sites, developing macroscopic, clinically detectable metastases [60-62].

Due to its systematic nature and the resistance of disseminated tumor cells to existing therapeutic agents, metastatic tumors are much more difficult to cure compared with primary tumors which can be well treated by surgical resection and adjuvant therapy [60]. More than 90% of cancer death is due to metastasis rather than primary tumors [61]. However, only recently the molecular and cell-biology mechanisms of metastases emerged, while many details remain poorly understood and need to be explored in patients. Therefore, understanding the biological details of metastatic mechanisms, and developing strategies to prevent and treat tumor metastasis are in urgent need for cancer research.

2.1.4 Progress on detection of circulating tumor cells

During tumor metastasis, circulating tumor cells (CTCs) are often detected, which are an indicator of poor prognosis [4][63]. Circulating tumor cells are cells in blood presenting antigenic or genetic characters of a particular tumor type, which were cited in the American Society of Clinical Oncology 2007 updated recommendation for the use of tumor markers in breast cancer [64]. CTC detection is reported as an indication of the prognosis in early-stage breast cancer patients, and early systemic tumor cell metastasis [65-69]. Also, CTC level changes may provide a minimally invasive method to assess patients' response to drug treatments by therapeutic agents [68]. In addition, the genetic characterization of CTCs is believed to be a key to figure out the relationship between primary tumors and metastatic tumors, which may make detection of CTCs an important clinical tool for diagnosing and treatment of tumor metastasis [14][70].

A variety of approaches have been used to detect CTCs, while most of them require enrichment or isolation of CTCs before detection [71]. Nucleic-acid based methods use the detection of genetic

alternations that are specific for cancer cells to identify CTCs [72-75]. The detection of free tumor-derived DNA in serum/plasma of prostate cancer patients was proposed to relate to the presence of CTCs [76][77]. However, nucleic-acid based methods present low specificity since it is hard to distinguish from a true positive signal due to the strong background noise caused by expression of markers in normal cells [78]. Detections of CTCs were also performed by separating CTCs from red blood cells based on their relative larger size and differences in density, charge, migratory properties [79-82]. These techniques, however, still need further validation with clinical specimens, in which variations of heterogeneous CTC size and resistance to filtering shear stress exist [83]. Antibodies against cell surface antigens are widely used for capture of CTCs. CellSearch system (Veridex™, Warren, PA) is a FDA (Food and Drug Administration)-approved method which conjugates antibodies against epithelial cell adhesion molecule (EpCAM) to ferrofluids and purifies CTCs through a magnetic field [84]. This platform, however is limited by its low sensitivity [85][86]. High throughput microscopic scanning methods have been used for CTC detection. Both fiber-optical-array scanning approach and laser-scanning cytometry identify unpurified viable CTCs deposited on a glass slide, which enable cytological evaluation of CTCs without pre-selection bias but is less conducive for further molecular and biological characterization [87-89]. Recently, flowmetry has been used for *in vivo* detection of CTCs [90-93]. Among these, photoacoustic flowmetry was reported to be used for detecting melanoma cells [91]. Photoacoustic detection of magnetically captured CTCs was demonstrated by using nanoparticles (NPs) to target cell surface antigens, which however, lacked specificity [92][93]. Surface-enhanced-Raman-scattering (SERS) NPs were used for *in vivo* CTC detection with potentially high specificity due to high multiplexing capability of SERS NPs, while enrichment of CTCs was not included [94]. As a whole, existing CTC detection techniques each has unique advantages and limits. New technologies need to be further developed to detect CTCs with efficient capture, high sensitivity and specificity.

2.2 Optical resolution photoacoustic imaging

2.2.1. Photoacoustic wave generation

The photoacoustic effect was first reported by Alexander Graham Bell in 1880, which refers to the generation of acoustic waves by absorption of electromagnetic (EM) energy, especially optical energy in this report [95]. When a target is irradiated by short laser pulses, the absorbed pulse

energy is converted to heat, hence leads to a local temperature rise which induces pressure waves through thermo-elastic expansion. The pressure wave, termed photoacoustic waves, detected by ultrasound transducer can thus be used to determine optical properties of the target.

Optical properties include optical scattering and optical absorption, which are related to molecular constituents and structures of biological tissues. Optical absorption coefficients of biological tissues vary between 0.1 cm^{-1} and 10 cm^{-1} in the visible to near-infrared region. The intrinsic high optical absorption contrast of hemoglobin to surrounding tissues makes optical absorption based techniques excellent candidates for imaging the microvasculature. In addition, optical absorption in tissues is sensitive to molecular composition. This can be useful for functional imaging, for example the absorption spectrum difference between oxygenated hemoglobin and deoxygenated hemoglobin can be used to estimate oxygen saturation of hemoglobin [96]. Optical scattering is strong in biological tissues, which limits the imaging depth of high resolution optical imaging to $\sim 1\text{mm}$ due to drastically resolution degradation.

Thermal and stress confinements are two crucial conditions for efficiently generating photoacoustic signals [97]. Thermal relaxation time, $\tau_{th} = d_c^2/\alpha_{th}$, characterizes the thermal diffusion of absorbed optical energy, where d_c is the characteristic dimension, α_{th} is the thermal diffusivity of heated area [98]. Stress relaxation time, $\tau_s = d_c/v_s$, characterizes the pressure propagation in the heated area, where, v_s is the speed of sound. When the laser excitation is in both the thermal and stress confinements, the local pressure rise immediately induced by optical absorption via thermal expansion can be expressed as [2][3]:

$$p_0 = \frac{\beta v_s^2}{c_p} \mu_a F = \Gamma \mu_a F \quad (1)$$

where β denotes the thermal coefficient of volume expansion in K^{-1} , C_p denotes the specific heat capacity at constant pressure in $\text{J}/(\text{kg K})$, μ_a is the optical absorption coefficient in cm^{-1} , F is the optical fluence in J/cm^2 . $\Gamma = \frac{\beta v_s^2}{c_p}$, is the Gruneisen parameter. The speed of sound and thermal coefficient of volume expansion are both temperature dependent, hence the Gruneisen parameter is temperature dependent. An empirical formula can be used to estimate Gruneisen parameter for water and aqueous solutions as following [98]:

$$\Gamma_w(T_0) = 0.0043 + 0.0053T_0 \quad (2)$$

where T_0 is the temperature in degree Celsius. Thus, the strength of photoacoustic signals is proportional to optical absorption coefficient, optical fluence, Gruneisen parameter, and is related to temperature.

The attenuation of ultrasound in soft tissue increases with the frequency. The ultrasonic attenuation coefficient, $\mu = af^b$, where a and b are constants, and f is the ultrasonic frequency [99]. Neglecting the inhomogeneity of acoustic speed, the speed of sound in most soft tissues is relatively constant at 1.5 mm/ μ s with a small variation of less than 10% [99][100]. Based on the temporal photoacoustic signal, we can get the depth-dependent tissue information.

2.2.2. Photoacoustic Imaging

Photoacoustic has been developed rapidly in the last decade for biomedical applications, involving vascular biology, oncology, neurology, ophthalmology, dermatology, gastroenterology, and cardiology [101-116]. This is in part due to the benefits of photoacoustic imaging, including safety, high contrast, and high spatial resolution at relatively deep imaging depths. Photoacoustic imaging employs nonionizing waves which pose no health hazard compared with ionizing CT or PET. Along with its non-destructive, non-invasive nature, photoacoustic imaging is an ideal candidate for *in vivo* applications. Photoacoustic imaging is based on intrinsic high optical absorption contrast with no back ground while the mechanical contrast based ultrasound imaging is less informative for some tasks [96]. In addition, photoacoustic signals are sensitive to hemoglobin concentration and to oxygen saturation due to different optical absorption spectra of oxygenated and deoxygenated hemoglobin, which can be used for functional imaging as well. The spatial resolution of photoacoustic imaging can outperform that of optical imaging in the quasi-diffusive or diffusive regime in biological tissues since optical scattering in soft tissues is two or three orders stronger than ultrasound scattering which impaired resolution remarkably with increasing depth [96].

Currently, photoacoustic imaging systems can be divided into two main categories: computational photoacoustic tomography (PAT) and photoacoustic microscopy (PAM). PAT is a reconstruction-based imaging technique. Since temporal photoacoustic signals detected at different locations offer 1D information about photoacoustic source in axial direction, 2D surface scan can provide sufficient information for a 3D reconstruction of photoacoustic source. Usually,

a full-field illumination is employed to induce optical absorption from a relatively large tissue volume in PAT. The generated ultrasonic waves are then detected by a mechanically-scanned ultrasound receiver or array of receivers when they propagate to the tissue surface [117]. Various inverse algorithms have been developed to reconstruct PAT resource from the detected photoacoustic signals [117]. Up to 50Hz cross-sectional imaging frame rate was reported in using PAT [118]. However, the imaging resolution of PAT is usually limited to several hundreds of micrometers owing to the low frequency ultrasound used [119].

In photoacoustic microscopy (PAM), usually a focused ultrasound detector and/or a focused laser beam are confocally configured to achieve maximum sensitivity. A 1D depth-resolved image, termed an A-line, is generated by each laser pulse. Therefore, a 3D image can be formed by 2D transverse scanning of ultrasonic detector or laser beam or the target, and then putting all acquired 1D images together. There is no need for inverse reconstruction algorithm in PAM. The axial resolution of PAM is determined by the temporal profile of induced acoustic signals and is limited by the bandwidth of the transducer, while the lateral resolution is determined by the optical or ultrasonic focal spots, depending on the depth and illumination configuration [101][120]. Based on whether the optical or ultrasonic focus is finer, PAM is further divided into acoustic-resolution PAM (AR-PAM) and optical-resolution PAM (OR-PAM). In AR-PAM, resolution is determined by ultrasonic focusing and limited by the ultrasonic diffraction limit. It is not limited by optical scattering and may use a broad illumination pattern. Therefore, high resolution at depths beyond the optical transport mean free path and up to a few centimeters can be achieved with diagnostic frequencies or to depths of a few mm at higher frequencies. Using a 50 MHz high frequency ultrasound transducer to achieve tight acoustic focus, AR-PAM was demonstrated capable of *in vivo* imaging at 3mm depth with 15 μm lateral resolution and 45 μm axial resolution [121]. However, further improving the resolution by increasing the ultrasonic frequency is difficult due to strong propagation loss of ultrasonic waves at high frequencies, which limits the penetration depth of acoustic waves to only a few hundred micrometers in tissue for hundreds of MHz frequencies to rival resolutions achievable with optical focusing [101]. To solve this problem, OR-PAM was proposed [59].

2.2.3. Optical resolution photoacoustic microscopy

By tightly focusing a laser beam into superficial depths of a target, photoacoustic imaging pushes the limits of the lateral resolution to micron-scale, which is determined by the size of a focused light spot (limited by diffraction-limited focal spot size) rather than the width of the ultrasonic focal zone in AR-PAM. This novel imaging technology for visualizing optically-absorbing superficial structures with high contrast and high micron-scale lateral resolution is referred to as optical resolution photoacoustic microscopy (OR-PAM). OR-PAM is depth-limited to approximately one transport mean-free path (~ 1 mm in tissue) since diffraction-limited focusing is difficult to achieve past this depth due to multiple scattering. The ability to resolve capillaries enables OR-PAM to detect earlier stages of cancer than AR-PAM.

Maslov et al first demonstrated using OR-PAM to achieve micron-level lateral resolution at an imaging depth >0.7 mm (Fig.2.1) [59]. In their experiment, a $25 \mu\text{m}$ diameter pinhole was used to spatially filter the laser pulses from a dye laser and then was imaged to a focal spot by an objective lens. A plano-concave lens was used for achieving ultrasonic focusing. The optical objective lens and 75 MHz ultrasonic transducer were aligned coaxially and confocally. Volumetric images were generated by a two-dimensional (2D) raster scan along the x-y plane. Lateral resolution of $\sim 5 \mu\text{m}$ and imaging depth of at least $700 \mu\text{m}$ were achieved. Fig.2.1. (b) showed the *in vivo* OR-PAM image of microvasculature in a nude mouse ear within $1 \text{ mm} \times 1 \text{ mm}$ field of view (FOV), using 10 min acquisition time. Later, Xie et al. developed a laser-scanning OR-PAM (LS-OR-PAM) system based on the pioneering work of L.V. Wang's group [122]. In Xie's studies, fast-scanning mirrors was used to scan the optical spot relative to a fixed ultrasound transducer. A lateral resolution of $7.8 \mu\text{m}$ in a 6 mm-diameter circular field-of-view (FOV) was achieved. Because scanning of an optically-focused laser spot is required, the imaging speed of OR-PAM is limited by laser pulse-repetition rate.

More studies on using novel OR-PAM techniques for structural [123] and functional [123-127] imaging were reported. OR-PAM has demonstrated its potential applications for neuro-functional imaging, oxygen saturation imaging [124][125], blood velocity imaging[126], transcranial imaging of whole brain murine cortical capillary networks[127]. In addition, OR-PAM was reported to realize *in vivo* imaging of amyloid plaques in a transgenic mouse model of Alzheimer's

disease [107], as well as longitudinal monitoring of angiogenesis in a transgenic mouse model [102][103], demonstrating the potential to monitor the efficacy of anti-angiogenic therapies.

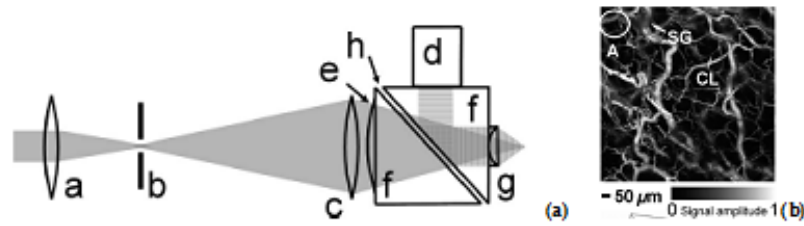


Fig.2.1. (a) Schematic of the OR-PAM light focusing system (a: condenser lens; b: pinhole; c: microscope objective lens; d: ultrasound transducer; e: correcting lens; f: isosceles prism; g: acoustic lens; h: silicon oil); (b) *in vivo* image of micro-vasculatures of a nude mouse ear with the OR-PAM system [59].

2.2.4. Challenges of OR-PAM

As a promising technique for imaging tumor angiogenesis, photoacoustic imaging has the features of non-invasiveness, non-ionizing radiation and is able to provide high contrast angiogenesis imaging due to intrinsic strong optical contrast between hemoglobin and tissues. Originated from photoacoustic imaging, OR-PAM has been developed as an imaging technology for visualizing optically-absorbing superficial vascular structures *in vivo* with lateral spatial resolution determined by optical focusing rather than acoustic detection. Micron-level resolution makes OR-PAM a promising method for imaging angiogenesis to its finest vascular components – capillaries. However, it also faces challenges preventing its clinical applications.

First, long acquisition times of OR-PAM limits its application in the clinic. Further, realtime imaging can be a useful tool for anti-angiogenic therapies due to the ability to monitor the efficacy of a drug candidate in real time, and can be also important to observe biological dynamic process. In OR-PAM with micron-level lateral resolution, the pixel number needed for even a small imaging field of view (FOV) is large. For example, 10 μm resolution for a 1 mm \times 1 mm imaging area requires tens of thousands of pixels, which means tens of thousands of photoacoustic A-scan lines need to be collected for each frame. Recently, 70 minutes acquisition time was reported to imaging a 7.8 mm \times 10mm area at 2.5 μm step size using the second generation OR-PAM system [128]. This acquisition speed is still not enough for clinical applications. No realtime volumetric OR-PAM imaging was reported until the work done by our group which is listed in the thesis.

Second, the imaging depth of OR-PAM is limited to $\sim 1\text{mm}$ with micron-scale resolution. Therefore, OR-PAM is usually used for super-facial imaging on the skin surface. To broaden the application of OR-PAM, OR-PAM endoscopy is a promising candidate which uses multimode optical fiber combined with miniature lens and/or ring transducer and/or miniature scanning mirrors [114][129].

Third, high laser pulse repetition rate employed in OR-PAM may cause overlapping of adjacent laser pulses on targets. Therefore, the temperature rise caused by previous laser pulses may change the Gruneisen parameter, subsequently inducing higher photoacoustic signals. Further work need to be done on the effects of scanning speed and laser-repetition-rate on photoacoustic signal especially for fast imaging speed OR-PAM.

2.3. Detection of circulating tumor cells

2.3.1. Photoacoustic detection of CTCs

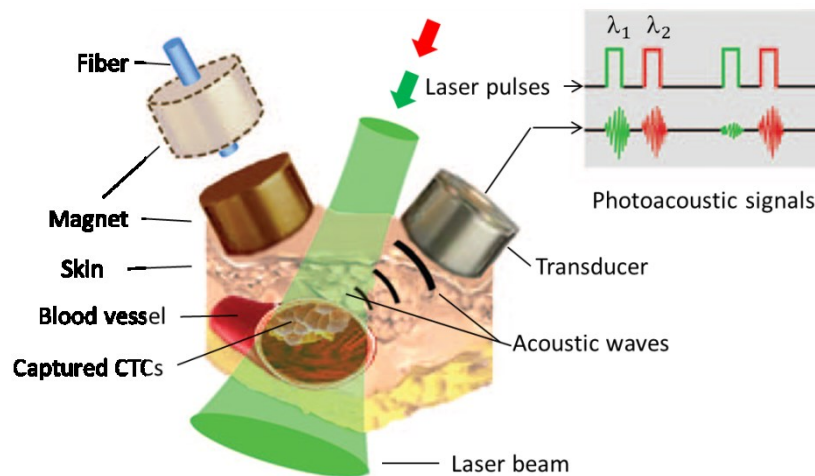


Fig.2.2. *In vivo* magnetic enrichment using two-colour photoacoustic detection of CTCs: either laser beam incidents near the external magnet or through a hole in the magnet by a fiber-based delivery system [92].

In 2009, V. Zharov's group reported *in vivo* rapid photoacoustic detection of magnetically captured CTCs (Fig.2.2) [92]. In their experiment, circulating breast cancer cells were targeted by both magnetic nanoparticles and carbon nanotubes, and were captured under a magnet. The magnetic nanoparticles were functionalized to target urokinase plasminogen activator receptors which are highly expressed on many kinds of cancer cells but are lowly expressed on normal blood and endothelial cells. In addition to serving as magnetic contrast agents, the magnetic nanoparticles

were also used as photoacoustic contrast agents due to their intrinsic optical absorption. Also, functionalized gold-plated carbon nanotubes acted as a second photoacoustic contrast agent for targeting folate receptors which are at high level in cancer cells compared to much lower levels in normal blood. Their experiment demonstrated the ability to concentrate and detect CTCs from a large volume of blood with high sensitivity *in vivo*, in realtime.

Recently M. O'Donnell's group at University of Washington demonstrated magnetically trapping and manipulating of CTCs-mimicking flowing polystyrene beads [130]. To achieve efficient magnetic trapping, a dual magnet system was used to produce a homogeneous magnetic field to magnetize contrast agents, along with a high magnetic field gradient to exert strong magnetic trapping force to magnetized contrast agents. Magneto-sensitive nanospheres and optical absorptive gold nanorods were used for targeting the polystyrene beads which mixed with a water-ink solution circulating inside a Teflon tube to mimic circulating tumor cells. Their results showed efficient magnetically trapping in a stream with a flow rate up to 12 ml / min, with minimum detectable bead number of about 50 beads. However, similar to Zharov's group, their setup did not show multiplexing ability to improve specificity of detection.

2.3.2. SERS detection of CTCs

Surface-enhanced Raman scattering

Raman scattering was first reported in 1928 by C. V. Raman etc. [131]. It is the inelastic scattering of a photon from an atom or a molecule when light interacts with matters. According to the frequency shift of the scattered photon related to incident photon, the scattering is also called Stokes (lower frequency) or Anti-Stokes (higher frequency) scattering respectively. Raman scattering provides rich information on the structure and composition of the atom or molecule, providing a spectral fingerprint.

Raman spectroscopy is based on the measurement of the vibrational energy levels of chemical bonds through Raman scattering. It is a non-destructive and non-invasive technique which can also be carried out under a wide range of conditions [132]. However, Raman spectroscopy is not widely used for practical applications due to its extremely weak signal (~1 photon is inelastically scattered for every 10^7 elastically scattered photons). In 1974, Fleischmann, Hendra and Mcquillan first reported a strong Raman signal from a monolayer of pyridine adsorbed on an electrochemically

roughened silver electrode [133]. This phenomenon was later called surface-enhanced Raman scattering (SERS), which is due to laser excitation of molecules adsorbed on nano-patterned metal surfaces or nanoparticles. The enhancement factor of 10^6 - 10^8 has been reported from typical experimental conditions, which allows the technique to be sensitive enough to detect single molecules.

Surface-enhanced Raman spectroscopy using SERS nanoparticles

In recent years, the biomedical research community has realized that for a specific disease process a single targeting agent may not be able to provide sufficient information. As a result, a lot of research has focused on developing techniques to realize sensitively and simultaneously detection of multiple targets. Lately, sensitive imaging of nanoparticles for both diagnostic and therapeutic applications has emerged as a hot topic [134-138]. Surface-enhanced Raman spectroscopy with SERS nanoparticles has recently been reported and offers ultralow background and very high multiplexing capabilities, important for specificity [139-141].

S. Gambhir's group at Stanford University recently showed that they could detect and classify multiple types of Raman nanoparticles injected into live mice with picomolar sensitivities (Fig.2.3) [142]. This work demonstrates the ability to detect a multiplicity of optical probes with high sensitivity *in vivo*. In their experiment, each SERS nanotag comprised a 60nm diameter Au core coated with a monolayer of Raman-active organic molecule and encapsulated with 30nm silica shell. Raman measurements were performed with a Reinshaw microscope system along with an x-y translation stage for raster scanning. Spectral classification algorithms were used to identify species of nanoparticles which were detected *in vivo* up to depths of several-mm.

In 2013, B. C. Wilson's group at University of Toronto reported *in vivo* multiplexed SERS imaging by using a tunable-filter-based widefield Raman imaging system with acquisition times orders of magnitude faster than achievable with comparable point-scanned methodologies [143]. In their experiment, four types of SERS reporter molecules were detected and separated after being implanted subcutaneously into a nude mouse. The ability to quantitatively analyze the amount of each reporter molecule with high fidelity was also demonstrated.

Other optical methods for probing biology *in vivo* such as fluorescence methods can spectrally resolve two or three probes. Now with SERS nanoparticles it may be possible to visualize several

(if not many) different probes simultaneously. Targeting these probes to molecules of interest may reveal significant insights into complex biological pathways *in vivo*.

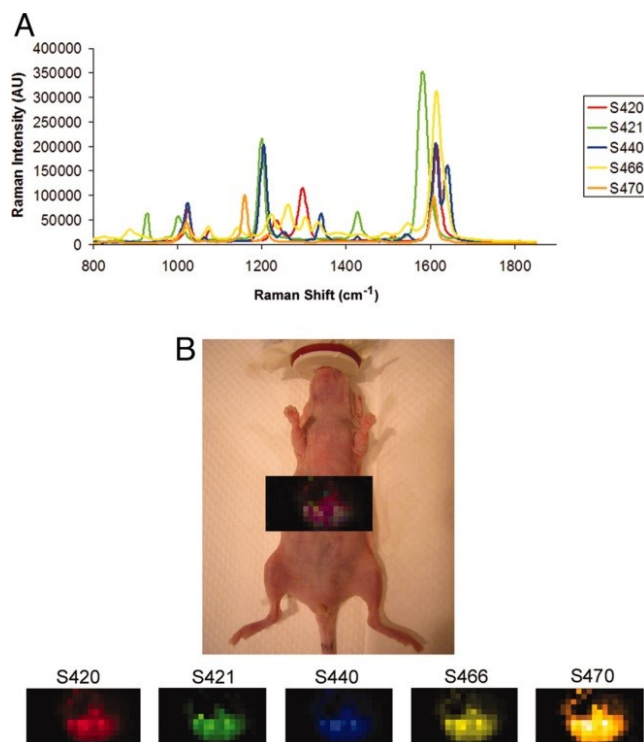


Fig.2.3. Demonstration of deep-tissue multiplexed imaging 24 h after intravenous (i.v.) injection of five unique SERS nanoparticle batches simultaneously. (A) Graph depicting five unique Raman spectra, each associated with its own SERS batch: S420 (red), S421 (green), S440 (blue), S466 (yellow), and S470 (orange). (B) Raman image of liver overlaid on digital photo of mouse, showing accumulation of all five SERS batches accumulating in the liver after 24 h post i.v. injection. Panels below depict separate channels associated with each of the injected SERS nanoparticle batches. Individual colors have been assigned to each channel, and the resulting mixture shows a purple color that represents a mixture of the five SERS nanoparticle batches accumulating simultaneously [142].

Detection of CTCs using SERS

In 2011, Wang et al., reported rapid detection of CTCs in human peripheral blood by using SERS NPs [94]. In their experiment, density-gradient centrifugation was used for isolating CTCs and leukocytes from whole blood. After incubation with bioconjugated epidermal growth factor (EGF)-SERS nanoparticles and centrifugations, SERS signals were detected from the remaining cell pellet as an indication of CTC numbers. The results showed the detection sensitivity was 5 to 50 tumor cells per mL of blood, and also indicated higher targeting specificity compared to whole antibody targeting. Their experiment demonstrated identification of CTCs in the peripheral blood of 19 cancer patients with CTC concentrations ranging from 1 to 720 CTCs per mL of whole blood.

However, their method lacked an enrichment technique, which limited their application for *in vivo* detection.

Silica-encapsulated magnetic NPs (M-SERS dots) were reported to generate strong SERS signals, hence can be potentially used for targeting cancer-cells, and also be useful for cancer-cell separation due to their magnetic properties [144]. In 2014, Quaresma et al., reported using star shaped gold-coated magnetic nanoparticles for detecting SERS signals from Astra Blue, and for magnetically separating a histidine-tagged maltose binding protein from a crude cell-extract [145]. However, magnetic trapping of CTCs were not studied in both approaches. In addition, false positive signals may be introduced during magnetic trapping due to existing free nanoparticles.

2.3.3. Folate targeting

To increase the binding of nanoparticles to tumor cells, reduce the non-specific adsorption by normal cells, and overcome the poor solubility and stability *in vivo*, usually nanoparticle surfaces need to be modified with a high-affinity targeting ligand [146]. One of the best-characterized ligands to target tumor cells is a water-soluble vitamin named folate, which is important for the survival of proliferating cells [147].

Folate is frequently employed as a targeting ligand due to several features: 1) the expression of folate receptor is significant on cancer cells of the lung, breast, ovary, kidney, brain, uterus, testes, colon and myelogenous leukemias, while it is low on most normal cells (typically more than 500 times less) [148-155]; 2) the affinity of folate receptor binding to folate is high, hence potentially a low dose of folate-agent is needed for saturating all available folate receptors; 3) folate conjugates are removed rapidly from receptor negative tissues, which may lower non-specific background [156]; 4) folate is a highly stable, inexpensive, non-immunogenic chemical with small molecular size [157].

Recently, folate functionalized liposomes derivations, superparamagnetic particles, polymer nanoparticles, gold nanoparticles, gadolinium nanoparticles, and core-shell nanostructures have been reported [158-165]. Various folate-conjugated agents have developed as low molecular weight cytotoxic drugs, liposomes with entrapped drugs, protein toxins, therapeutic genes, immunotherapeutic agents, nanoparticles and enzymes for prodrug therapy [166-183]. To prevent the aggregation, improve biocompatibility, and facilitate binding to cell-surface receptors,

poly(ethylene glycol) (PEG) spacer has been reported to help develop conjugated folate for cancer targeting [184-186].

2.3.4. Challenge of detecting circulating tumor cells

CTCs are regarded as “liquid biopsy” of cancer due to its potential to represent the overall disease more than primary tumor biopsies [187]. Research on CTCs may help to understand metastasis development mechanisms, assist cancer diagnosis & prognosis, and monitor response to therapy [71]. However, due to the rarity of CTCs in blood (~1- 10 CTCs per mL compared to millions of white blood cells and almost 1 billion of red blood cells per mL), methods with both high sensitivity and specificity are in urgent need for detection of CTCs.

Secondly, multimodality imaging and/or detection may be needed for efficient research on tumor metastasis. A forte of photoacoustic imaging is high resolution and optical absorption contrast, however, differentiation of signals is non-trivial hence specificity can be poor. In contrast, SERS imaging has the nature of high specificity, high sensitivity, and is an ideal tool for molecular imaging. Developing multimodality imaging methods, combining the advantages of existing imaging approaches is crucial for cancer research, molecular diagnostics and personal medicine.

Bibliography

- [1]. IARC, “Globocan 2012: Estimated Cancer Incidence, Mortality and Prevalence Worldwide in 2012,” http://globocan.iarc.fr/Pages/fact_sheets_cancer.aspx (accessed May 8, 2014)
- [2]. SI Hajdu, MJ Thun, LM Hannan, A Jemal, “A note from history: landmarks in history of cancer, part 1”, *Cancer* 117 (5), 1097–102. (2011)
- [3] J. Folkman, “Tumor Angiogenesis”, *Advan. Cancer Res.*, vol 19, 331- 357 (1974)
- [4] K. Pantel and R.H. Brakenhoff, “Dissecting the metastatic cascade”, *Nat. Rev. Cancer*, vol 4, 448–456 (2004)
- [5] J.A. Aguirre-Ghiso, “Models, mechanisms and clinical evidence for cancer dormancy”, *Nat. Rev. Cancer*, vol 7, 834–846 (2007)
- [6] HMW Verheul, EE Voest, and RO Schlingemann, “Are tumors angiogenesis-dependent”, *J Pathol* 202, 5–13 (2004)
- [7] E.J. Battegay, “Angiogenesis: mechanistic insights, neovascular diseases and therapeutic prospects”, *J Mol Med*, vol 73, 333-346 (1995)
- [8] J Rak, J Filmus, RS Kerbel, “Reciprocal paracrine interactions between tumour cells and endothelial cells: the "angiogenesis progression" hypothesis”, *Eur J Cancer* 32A, 2438-2450 (1996)
- [9] W. W. Li, “Tumor Angiogenesis: Molecular Pathology, Therapeutic Targeting, and Imaging”, *Acad Radiol*, vol 7, 800-811 (2000)
- [10] J Folkman, Y Shing, “Angiogenesis”, *J Biol Chem*, vol 267, 10931 – 10934 (1992)
- [11] KH Plate, G Breier, B Millauer, A Ullrich, W Risau, “Up-regulation of vascular endothelial growth factor and its cognate receptors in a rat glioma model of tumor angiogenesis”, *Cancer Res.*, vol 53,5822-5827 (1993)
- [12] D Shweiki, A Itin, D Soffer, E Keshet, “Vascular endothelial growth factor induced by hypoxia may mediate hypoxia-initiated angiogenesis”, *Nature* 359, 843-845 (1992)
- [13] P. Carmeliet and R. K. Jain, “Molecular mechanisms and clinical applications of angiogenesis nature”, *Nature*, vol 473, 298 (2011)
- [14] L. Wan, K. Pantel, and Y. Kang, “Tumor metastasis moving new biological insights into the clinic”, *Nature Medicine*, vol 19, 1450-1464 (2013)
- [15] W. Risau, “Mechanisms of angiogenesis”, *Nature* 386, 671–674 (1997)

- [16] P Carmeliet, RK Jain, “Angiogenesis in cancer and other diseases”, *Nature* vol 407, 249–257 (2000)
- [17] RO Schlingemann, FJ Rietveld, RM de Waa, et al., “Leukocyte antigen CD34 is expressed by a subset of cultured endothelial cells and on endothelial abluminal microprocesses in the tumor stroma”, *Lab Invest*, vol 62, 690–696 (1990)
- [18] RO Schlingemann, FJ Rietveld, RM deWaal, S Ferrone, DJ Ruiters, “Expression of the high molecular weight melanoma-associated antigen by pericytes during angiogenesis in tumors and in healing wounds”, *Am J Pathol*, vol 136, 1393–1405 (1990)
- [19] A. L. Harris, “Antiangiogenesis for cancer therapy”, *Lancet*, vol 349 (suppl II), 13-15 (1997)
- [20] C. Li, “A targeted approach to cancer imaging and therapy”, *Nature Materials*, vol 13, 110-115 (2014)
- [21] N Weidner, J Folkman, F Pozza, et al., “Tumor angiogenesis: a new significant and independent prognostic indicator in early-stage breast carcinoma”, *J Natl Cancer Inst*, vol 84, 1875–1887 (1992)
- [22] N. Weidner, “Tumoural vascularity as a prognostic factor in cancer patients: the evidence continues to grow”, *J Pathol*, vol 184, 119–122 (1998)
- [23] G Gasparini, M Toi, M Gion, et al., “Prognostic significance of vascular endothelial growth factor protein in node-negative breast carcinoma”, *J Natl Cancer Inst*, vol 89, 139–147 (1997)
- [24] P Macchiarini, G Fontanini, MJ Hardin, F Squartini, CA Angeletti, “Relation of neovascularization to metastasis of non-small-cell lung cancer”, *Lancet* 340, 145- 146 (1992)
- [25] MK Brawer, RE Deering, M Brown, SD Preston, SA Bigler, “Predictors of pathologic stage in prostatic carcinoma”, *Cancer* 73, 678-687 (1994)
- [26] EJ Hannen, JA Van Der Laak, JJ Manni, HP Freihofer, PJ Slootweg, R Koole, PC de Wilde, “Computer assisted analysis of the microvasculature in metastasised and nonmetastasised squamous cell carcinoma of the tongue”, *Head Neck*, vol 24, 643-650 (2002)
- [27] G Ascani, P Balercia, M Messi, L Lupi, G Goteri, A Filosa, et al., “Angiogenesis in oral squamous cell carcinoma”, *Acta Otorhinolaryngol Ital*, vol 25, 13-17 (2005)
- [28] AM Pabst, M Ackermann, W Wagner, D Haberthür, T Ziebart, MA Konecny, “Imaging angiogenesis: Perspectives and opportunities in tumour research - A method display”, *Journal of Cranio-Maxillo-Facial Surgery*, 1-9 (2014)

- [29] N McKenna, “*In vivo* imaging shines”, Genetic Engineering & Biotechnology News, vol 34, 28-30 (2014)
- [30] J. C. Miller , H. H. Pien , D. Sahani , A. G. Sorensen, J. H. Thrall, “Imaging Angiogenesis Applications and Potential for Drug Development”, Journal of the National Cancer Institute, vol 97, 172 (2005)
- [31] KA Miles, BB Kelley, “CT measurements of capillary permeability within nodal masses: a potential technique for assessing the activity of lymphoma”, Br J Radio1, vol 70, 74-79 (1997)
- [32] WA Kalender, W Seissler, E Klotz, P Vock, “Spiral volumetric CT with single-breathhold technique, continuous transport, and continuous scanner rotation”, Radiology, 176(1), 181–183 (1990)
- [33] CR Crawford and KF King, “Computed tomography scanning with simultaneous patient translation”, Med Phys 17(6), 967–982 (1990)
- [34] GD Rubin, MC Shiau, AN Leung, ST Kee, LJ Logan, MC Sofilos, “Aorta and iliac arteries: single versus multiple detector-row helical CT angiography”, Radiology 215(3), 670–676 (2000)
- [35] GD Rubin, AJ Schmidt, LJ Logan, et al., “Multidetector-row CT angiography of lower extremity occlusive disease: a new application for CT scanning”, Radiology 210(P), 588 (1999)
- [36] MA Bogdan, MB Klein, GD Rubin, TR McAdams, J Chang, “CT angiography in complex upper extremity reconstruction”, J Hand Surg, 29(5), 465–469 (2004)
- [37] GD. Rubin, J Leipsic, UJ Schoepf, D Fleischmann, S Napel, “CT Angiography after 20 Years: A Transformation in Cardiovascular Disease Characterization Continues to Advance”, Radiology, vol 271, 633-652 (2014)
- [38] MS Pearce, JA Salotti, MP Little, et al., “Radiation exposure from CT scans in childhood and subsequent risk of leukaemia and brain tumours: a retrospective cohort study”, Lancet 380 (9840), 499–505 (2012)
- [39] AC Silva, SG Kim, M Garwood, “Imaging blood flow in brain tumors using arterial spin labeling”, Magn Reson Med, vol 44, 169–173 (2000)
- [40] R Abramovitch, D Frenkiel, M Neeman, “Analysis of subcutaneous angiogenesis by gradient echo magnetic resonance imaging”, Magn Reson Med, vol 39, 813-824 (1998)
- [41] R. C. Brasch, K. C. P. Li, et al., “*In vivo* monitoring of tumor angiogenesis with MRI”, Acad Radiol, vol 7, 812-823 (2000)

- [42] M Rudin, PMJ McSheehy, PR Allegrini, M Rausch, D Baumann, M Becquet, et al., “PTK787/ZK222584, a tyrosine kinase inhibitor of vascular endothelial growth factor receptor, reduces uptake of the contrast agent GdDOTA by murine orthotopic B16/Bl6 melanoma tumours and inhibits their growth *in vivo*”, *NMR Biomed*, vol 18, 308-321 (2005)
- [43] G. Niu, X. Chen, “PET imaging of angiogenesis”, *PET Clin*, vol 4, 17–38 (2009)
- [44] EM Rohren, TG Turkington, RE Coleman, “Clinical applications of PET in oncology”, *Radiology*, vol 231, 305 – 32 (2004)
- [45] F Kiessling, M Krix, M Heilmann, S Vosseler, M Lichy, C Fink, et al., “Comparing dynamic parameters of tumor vascularization in nude mice revealed by magnetic resonance imaging and contrast-enhanced intermittent power Doppler sonography”, *Invest Radiol*, vol 38, 516 – 524 (2003)
- [46] N Lassau, C Paturel-Assehn, JM Guinebretiere, et al., “New hemodynamic approach to angiogenesis: color and pulsed Doppler ultrasonography”, *Invest Radiol*, vol 34, 194-198 (1999)
- [47] WF Cheng, CN Lee, JS Chu, et al., “Vascularity index as a novel parameter for the *in vivo* assessment of angiogenesis in patients with cervical carcinoma”, *Cancer*, vol 85, 651-657 (1999)
- [48] WF Cheng, TM Chen, CA Chen, et al., “Clinical application of intratumoral blood flow study in patients with endometrial carcinoma”, *Cancer* 82, 1881-1886 (1998)
- [49] J Rebol, B Brkljacic, Z Bumber, S Psenicnik, P Povalej, “3D power Doppler analysis of the vascularisation in tumours of the oral cavity”, *Ultraschall Med*, vol 28, 40-44 (2007)
- [50] J Rebol, “The vascularisation of oral cavity tumours and tumour shell tissue determined by three-dimensional power Doppler sonography”, *Ultrasound Med Biol* 33, 493-499 (2007)
- [51] JM. Provenzale, “Imaging of angiogenesis clinical techniques and novel imaging methods”, *American Journal of Roentgenology*, vol 188, 11-23 (2007)
- [52] G Vassaux, T Groot-Wassink, “*In vivo* noninvasive imaging for gene therapy”, *J Biomed Biotechnol*, vol 2003, 92–101 (2003)
- [53] Q Zhu, N Chen, SH Kurtzman, “Imaging tumor angiogenesis by use of combined near-infrared diffusive light and ultrasound”, *Opt Lett* 28, 337–339 (2003)
- [54] EB Brown, RB Campbell, Y Tsuzuki, L Xu, P Carmeliet, D Fukumura, et al., “*In vivo* measurement of gene expression, angiogenesis and physiological function in tumours using multiphoton laser scanning microscopy”, *Nat Med* 7, 864-868 (2001)

- [55] A Taruttis, V Ntziachristos, “Translational Optical Imaging”, American Journal of Roentgenology, vol 199, 263–271 (2012)
- [56] G. Ku, X. Wang, G. Stoica, and L.-H. Wang, “Multiple-Bandwidth Photoacoustic Tomography”, Phys. Med. Biol., vol 49, 1329-1338 (2004)
- [57] G. Ku, X. Wang, X. Xie, G. Stoica, and L.-H. Wang, “Imaging of tumor angiogenesis in rat brains *in vivo* by photoacoustic tomography”, Appl. Opt., vol 44, 770-775 (2005)
- [58] X. D. Wang, Y. J. Pang, G. Ku, X. Y. Xie, G. Stoica, and L.-H. V. Wang, “Noninvasive laser-induced photoacoustic tomography for structural and functional *in vivo* imaging of the brain”, Nat. Biotechnol., vol 21, 803-806 (2003).
- [59] K. Maslov, H. F. Zhang, S. Hu and L. H., V., Wang, “Optical-resolution photoacoustic microscopy for *in vivo* imaging of single capillaries”, Opt. Lett. 33, 929-931 (2008)
- [60] S Valastyan and RA Weinberg, “Tumor metastasis molecular insights and evolving paradigms”, Cell 147, 275-292 (2011)
- [61] G. P. Gupta and J. Massagué, “Cancer Metastasis: Building a Framework”, Cell 127, 679-695 (2006)
- [62] P. Friedl, and K. Wolf, “Tumour-cell invasion and migration: diversity and escape mechanisms”, Nat. Rev. Cancer 3, 362–374 (2003)
- [63] R. Gangnus, , S. Langer, E. Breit, K. Pantel, and M.R. Speicher, “Genomic profiling of viable and proliferative micrometastatic cells from early-stage breast cancer patients”, Clin. Cancer Res. 10, 3457–3464 (2004).
- [64] L. Harris, H. Fritsche, R. Mennel, et al., “American Society of Clinical Oncology 2007 Update of Recommendations for the Use of Tumor Markers in Breast Cancer”, Journal of Clinical Oncology, vol 25, 5287-5312 (2007)
- [65] M. Ignatiadis, et al., “Different prognostic value of cytokeratin-19 mRNA positive circulating tumor cells according to estrogen receptor and HER2 status in early-stage breast cancer”, J. Clin. Oncol. 25, 5194–5202 (2007)
- [66] F. Wolfrum, I. Vogel, F. Fandrich, and H. Kalthoff, “Detection and clinical implications of minimal residual disease in gastro-intestinal cancer”, Langenbecks Arch. Surg. 390, 430–441 (2005)

- [67] E. Soeth, et al., “Detection of tumor cell dissemination in pancreatic ductal carcinoma patients by CK 20 RT-PCR indicates poor survival”, *J. Cancer Res. Clin. Oncol.* 131, 669–676 (2005)
- [68] M. Cristofanilli, G.T. Budd, M.J. Ellis, A. Stopeck, et al., et al., “Circulating tumor cells, disease progression, and survival in metastatic breast cancer”, *N. Engl. J. Med.* 351, 781–791 (2004).
- [69] D. F. Hayes, et al., “Circulating tumor cells at each follow-up time point during therapy of metastatic breast cancer patients predict progression-free and overall survival”, *Clin. Cancer Res.* 12, 4218–4224 (2006).
- [70] H. Schwarzenbach, D.S.Hoon, and K. Pantel, “Cell-free nucleic acids as biomarkers in cancer patients”, *Nat. Rev. Cancer* 11, 426–437 (2011)
- [71] K. Pantel, R. H. Brakenhoff, and B. Brandt, “Detection, clinical relevance and specific biological properties of disseminating tumour cells”, *Nat Rev Cancer*, vol 8, 329-40 (2008)
- [72] E. Papadopoulou, E. Davilas, V. Sotiriou, E. Georgakopoulos, S. Georgakopoulou, A. Koliopanos, F. Aggelakis, K. Dardoufas, N.J. Agnanti, I. Karydas, and G. Nasioulas, “Cell-free DNA and RNA in plasma as a new molecular marker for prostate and breast cancer”, *Ann. NY Acad. Sci.* 1075, 235– 243 (2006)
- [73] E. Gormally, E. Caboux, P. Vineis, and P. Hainaut, “Circulating free DNA in plasma or serum as biomarker of carcinogenesis: practical aspects and biological significance”, *Mutat. Res.* 635, 105–117 (2007)
- [74] Zanetti-Dällenbach, R., E. Wight, A.X. Fan, O. Lapaire, S. Hahn, W. Holzgreve, and X.Y. Zhong. “Positive correlation of cell-free DNA in plasma/ serum in patients with malignant and benign breast disease”, *Anticancer Res.* 28:921–925 (2008)
- [75] K.A. Yoon, S. Park, S.H. Lee, J.H. Kim, and J.S. Lee, “Comparison of circulating plasma DNA levels between lung cancer patients and healthy controls”, *J. Mol. Diagn.* 11, 182–185 (2009)
- [76] H. Schwarzenbach, F.K. Chun, I. Lange, S. Carpenter, M. Gottberg, A. Erbersdobler, M.G. Friedrich, H. Huland, and K. Pantel, “Detection of tumor-specific DNA in blood and bone marrow plasma from patients with prostate cancer”, *Int. J. Cancer.* 120, 1465–1471 (2007)
- [77] H. Schwarzenbach, C. Alix-Panabières, I. Müller, N. Letang, J.P. Vendrell, X. Rebillard, and K. Pantel, “Cell-free tumor DNA in blood plasma as a marker for circulating tumor cells in prostate cancer”, *Clin. Cancer Res.* 15, 1032–1038 (2009)

- [78] B. Mostert, S. Sleijfer, J. A. Foekens, J. W. Gratama, “Circulating tumor cells (CTCs): Detection methods and their clinical relevance in breast cancer”, *Cancer Treatment Reviews*, vol 35 463–474 (2009)
- [79] R. Gertler, R. Rosenberg, K. Fuehrer, M. Dahm, H. Nekarda, and J.R. Siewert, “Detection of circulating tumor cells in blood using an optimized density gradient centrifugation”, *Recent Results Cancer Res.* 162, 149–155 (2003)
- [80] V. Müller, N. Stahmann, S. Riethdorf, T. Rau, T. Zabel, A. Goetz, F. Jänicke, and K. Pantel, “Circulating tumor cells in breast cancer: correlation to bone marrow micrometastases, heterogeneous response to systemic therapy and low proliferative activity”, *Clin. Cancer Res.* 11, 3678–3685 (2005)
- [81] P. Wülfing, J. Borchard, H. Buerger, S. Heidl, K.S. Zänker, L. Kiesel, and B. Brandt, “HER2-positive circulating tumor cells indicate poor clinical outcome in stage I to III breast cancer patients”, *Clin. Cancer Res.* 12, 1715–1720 (2006)
- [82] T.M. Morgan, P.H. Lange, and R.L. Vessella, “Detection and characterization of circulating and disseminated prostate cancer cells”, *Front. Biosci.* 12, 3000–3009 (2007)
- [83] M. Yu, S. Stott, M. Toner, S. Maheswaran, and D. A. Haber, “Circulating tumor cells: approaches to isolation and characterization”, *J. Cell Biol.*, vol. 192, 373–382 (2011)
- [84] S. Riethdorf, , H. Fritsche, V. Müller, T. Rau, C. Schindlbeck, B. Rack, W. Janni, C. Coith, K. Beck, F. Jänicke, et al., “Detection of circulating tumor cells in peripheral blood of patients with metastatic breast cancer: a validation study of the CellSearch system”, *Clin. Cancer Res.* 13, 920– 928 (2007)
- [85] W.J. Allard, J. Matera, M.C. Miller, M. Repollet, M.C. Connelly, C. Rao, A.G. Tibbe, J.W. Uhr, and L.W. Terstappen, “Tumor cells circulate in the peripheral blood of all major carcinomas but not in healthy subjects or patients with nonmalignant diseases”, *Clin. Cancer Res.* 10, 6897–6904 (2004)
- [86] G. Attard, J.F. Swennenhuis, D. Olmos, A.H. Reid, E. Vickers, R. A’Hern, R. Levink, F. Coumans, J. Moreira, R. Riisnaes, et al., “Characterization of ERG, AR and PTEN gene status in circulating tumor cells from patients with castration-resistant prostate cancer”, *Cancer Res.* 69, 2912– 2918 (2009)

- [87] R.T. Krivacic, A. Ladanyi, D.N. Curry, H.B. Hsieh, P. Kuhn, D.E. Bergsrud, J.F. Kepros, T. Barbera, M.Y. Ho, L.B. Chen, et al., “A rare-cell detector for cancer”, *Proc. Natl. Acad. Sci. USA.* 101, 10501–10504 (2004)
- [88] D. Marrinucci, K. Bethel, R.H. Bruce, D.N. Curry, B. Hsieh, M. Humphrey, R.T. Krivacic, J. Kroener, L. Kroener, A. Ladanyi, et al., “Case study of the morphologic variation of circulating tumor cells. *Hum. Pathol.* 38, 514–519 (2007)
- [89] K. Pachmann, J.H. Clement, C.P. Schneider, B. Willen, O. Camara, U. Pachmann, and K. Höffken, “Standardized quantification of circulating peripheral tumor cells from lung and breast cancer”, *Clin. Chem. Lab. Med.* 43, 617–627 (2005)
- [90] W. He, H. Wang, L.C. Hartmann, J.X. Cheng, and P.S. Low, “*In vivo* quantitation of rare circulating tumor cells by multiphoton intravital flow cytometry”, *Proc. Natl. Acad. Sci. USA.* 104, 11760–11765 (2007)
- [91] R.M. Weight, P.S. Dale, and J.A. Viator, “Detection of circulating melanoma cells in human blood using photoacoustic flowmetry”, *Conf. Proc. IEEE Eng. Med. Biol. Soc.* 2009, 106–109 (2009)
- [92] E.I. Galanzha, E.V. Shashkov, T. Kelly, J.W. Kim, L. Yang, and V.P. Zharov, “*In vivo* magnetic enrichment and multiplex photoacoustic detection of circulating tumour cells”, *Nat. Nanotechnol.* 4, 855–860 (2009)
- [93] E.I. Galanzha, E.V. Shashkov, P.M. Spring, J.Y. Suen, and V.P. Zharov, “*In vivo*, noninvasive, label-free detection and eradication of circulating metastatic melanoma cells using wo-color photoacoustic flow cytometry with a diode laser”, *Cancer Res.* 69, 7926–7934 (2009)
- [94] X. Wang, X. Qian, J. J. Beitler, G. Chen, F. R. Khuriet, M. M. Lewis, H. J. C. Shin, S. Nie, D. M. Shin, “Detection of Circulating Tumor Cells in Human Peripheral Blood using Surface-Enhanced Raman Scattering Nanoparticles,” *Cancer Res.*, 71(5), 1526–1532 (2011).
- [95] A. G. Bell, “On the Production and Reproduction of Sound by Light”, *Am. J. Sci.* 20, 305-324 (1880)
- [96] M.-H. Xu and L.-H. V. Wang, “Photoacoustic imaging in biomedicine”, *Rev. Sci. Instr.* 77, 041101 (2006)
- [97] V. E. Gusev and A. A. Karabutov, *Laser Optoacoustics* (American Institute of Physics, New York, 1993)

- [98] L. V. Wang and H. Wu, *Biomedical Optics: Principles and Imaging* (John Wiley & Sons, Inc., Hoboken, 2007)
- [99] F. A. Duck, *Physical Properties of Tissue* (Academic, London, 1990)
- [100] P. N. T. Wells, "Ultrasonic imaging of the human body", *Rep. Prog. Phys.* 62, 671 (1999).
- [101] L. V. Wang and S. Hu, "Photoacoustic tomography *in vivo* imaging from organelles to organs", *Science* 335, 1458 (2012);
- [102] S. Oladipupo, S. Hu, J. Kovalski, J. Yao, A. C. Santeford, R. Sohn, R. V. Shohet, K. Maslov, L. V. Wang, and J. M. Arbeit, "VEGF is essential for hypoxia-inducible factor mediated neovascularization but dispensable for endothelial sprouting", *PNAS* 108(32), 13264-13269 (2011)
- [103] S. Oladipupo, S. Hu, A. C. Santeford, J. Yao, J. Kovalski, R. V. Shohet, K. Maslov, L. V. Wang, and J. M. Arbeit, "Conditional HIF-1 induction produces multistage neovascularization with stage-specific sensitivity to VEGFR inhibitors and myeloid cell independence, " *Blood* 117(15), 4142-4153 (2011).
- [104] T. N. Erpelding et al., "Sentinel lymph nodes in the rat: noninvasive photoacoustic and US imaging with a clinical US system", *Radiology* 256, 102 (2010).
- [105] C. Kim et al., "*In vivo* Molecular Photoacoustic Tomography of Melanomas Targeted by Bioconjugated Gold Nanocages", *ACS Nano* 4, 4559 (2010).
- [106] S. Hu, L. V. Wang, "Neurovascular photoacoustic tomography", *Front. Neuroenerg.* 2, (2010).
- [107] S. Hu, P. Yan, K. Maslov, J. M. Lee, and L. H. V. Wang, "Intravital imaging of amyloid plaques in a transgenic mouse model using optical-resolution photoacoustic microscopy," *Opt. Lett.* 34 (24), 3899-3901 (2009)
- [108] X. Wang, Y. J. Pang, G. Ku, X. Y. Xie, G. Stoica, and L.-H. V. Wang, "Noninvasive laser-induced photoacoustic tomography for structural and functional *in vivo* imaging of the brain", *Nat. Biotechnol.*, vol 21, 803-806 (2003).
- [109] S. Hu, B. Rao, K. Maslov, L. V. Wang, "Label-free photoacoustic ophthalmic angiography", *Opt. Lett.* 35, 1 (2010)
- [110] S. Jiao et al., "Photoacoustic ophthalmoscopy for *in vivo* retinal imaging", *Opt. Express* 18, 3967 (2010)

- [111]. E. Z. Zhang et al., “Multimodal photoacoustic and optical coherence tomography scanner using an all optical detection scheme for 3D morphological skin imaging”, *Biomed. Opt. Express* 2, 2202 (2011)
- [112] C. P. Favazza, O. Jassim, L. A. Cornelius, L. V. Wang, “*In vivo* photoacoustic microscopy of human cutaneous microvasculature and a nevus”, *J. Biomed. Opt.* 16, 016015 (2011).
- [113] J.-M. Yang et al., “Photoacoustic endoscopy”, *Opt. Lett.* 34, 1591 (2009).
- [114]. J.-M. Yang et al., “Toward dual-wavelength functional photoacoustic endoscopy: laser and peripheral optical systems development”, *Proc. SPIE* 8223, 822316 (2012).
- [115]. K. Jansen, A. F. W. van der Steen, H. M. M. van Beusekom, J. W. Oosterhuis, G. van Soest, “Intravascular photoacoustic imaging of human coronary atherosclerosis”, *Opt. Lett.* 36, 597(2011).
- [116] B. Wang et al., “Plasmonic intravascular photoacoustic imaging for detection of macrophages in atherosclerotic plaques”, *Nano Lett.* 9, 2212 (2008).
- [117] P. Beard, “Biomedical photoacoustic imaging”, *Interface Focus*, 1, 602-631 (2011)
- [118] S Hu, LV.Wang, “Photoacoustic imaging and characterization of the microvasculature”, *J Biomed Opt* 15(1), 011101 (2010)
- [119] J. Yao and L. V. Wang, “Photoacoustic tomography fundamentals, advances and prospects”, *Contrast Media Mol. Imaging* 6, 332 - 345 (2011)
- [120] G. Ku and L. V. Wang, “Scanning thermoacoustic tomography in biological tissue”, *Med. Phys.* 27, 1195-1202 (2000)
- [121] K. Maslov, G. Stoica, and L.V. Wang, “*In vivo* dark-field reflection-mode photoacoustic microscopy”, *Opt. Lett.* 30, 625–627 (2005)
- [122] Z. X. Xie, S. L. Jiao, H. F. Zhang and C. A. Puliafito, “Laser-scanning optical-resolution photoacoustic microscopy”, *Opt. Lett.* 34, 1771-1773 (2009)
- [123] S. Hu, K. Maslov, and L. V. Wang, “Noninvasive label-free imaging of microhemodynamics by optical-resolution photoacoustic microscopy,” *Opt. Express* 17, 7688–7693 (2009)
- [124] S. Hu, K. Maslov, and L. V. Wang, “*In vivo* functional chronic imaging of a small animal model using optical-resolution photoacoustic microscopy,” *Med. Phys.* 36, 2320–2323 (2009).
- [125] L. Song, K. Maslov, and L. V. Wang, “Multifocal optical-resolution photoacoustic microscopy *in vivo*,” *Opt. Lett* 36, 1236-1237 (2011).

- [126] J. Yao, K. Maslov, Y. Shi, L. Taber, and L. V. Wang, “*In vivo* photoacoustic imaging of transverse blood flow using Doppler broadening of bandwidth,” *Opt. Lett.* 35, 1419–1421 (2010)
- [127] S. Hu, K. Maslov, V. Tsytsarev, and L. V. Wang, “Functional transcranial brain imaging by optical-resolution photoacoustic microscopy,” *J. Biomed. Opt.* 14, 040503 (2009)
- [128] S. Hu, K. Maslov, and L. V. Wang, “Second-generation optical-resolution photoacoustic microscopy with improved sensitivity and speed,” *Opt. Lett.*, vol 16, 1134 (2011)
- [129] P. Hajireza, W. Shi and R. J. Zemp, “Label-Free *In vivo* GRIN-Lens Optical Resolution Photoacoustic Micro-Endoscopy”, *Laser Phys. Lett.* 10 055603 (2013).
- [130] C. Wei, J. Xia, I. Pelivanov, X. Hu, X. Gao, M. O’Donnell, “Trapping and dynamic manipulation of polystyrene beads mimicking circulating tumor cells using targeted magnetic/ photoacoustic contrast agents,” *J. Biomed. Optics* 17(10), 101517(2012)
- [131] U. K. Sur, Resonance. “Surface-Enhanced Raman Spectroscopy: Recent Advancement of Raman Spectroscopy”, *Resonance*, 154- 164(2010)
- [132] M. K. Hossain and Y. Ozaki, “Surface-enhanced Raman scattering: facts and inline trends”, *Current Science* 2, 192-201 (2009)
- [133] M. Fleischmann, P. J. Hendra, A. J. McQuiUan, “Raman spectra of pyridine adsorbed at a silver electrode”, *Chem. Phys. Lett.* 26 (2), 163-166 (1974)
- [134] P. Fortina, L.J. Kricka, S. Surrey, P. Grodzinski, “Nanobiotechnology: the promise and reality of new approaches to molecular recognition”, *Trends Biotechnol.* 23 (4), 168-173(2005)
- [135] X. Michalet, F. F. Pinaud, L. A. Bentolila, J. M. Tsay, S. Doose, J. J. Li, G. Sundaresan, A. M. Wu, S. S. Gambhir, S. Weiss, “Quantum Dots for Live Cells, *in vivo* Imaging, and Diagnostics”, *Science*. 307, 538-544(2005)
- [136] K.K. Jain, “Nanomedicine: application of nanobiotechnology in medical practice”, *Med Princ Pract.* 17(2), 89-101(2008)
- [137] K.K. Jain, “Recent advances in nanooncology”, *Technol Cancer Res Treat.* 7(1), 1-13 (2008)
- [138] K.B. Hartman, L.J. Wilson, M.G. Rosenblum, “Detecting and treating cancer with nanotechnology”, *Mol Diagn Ther.* 12(1), 1-14(2008)
- [139] S. Lin, X. Xie, M.R. Patel., Y.H. Yang, Z. Lin, F. Cao, O. Gheysens, Y. Zhang, S.S. Gambhir, J.H. Rao and J.C. Wu, “Quantum dot imaging for embryonic stem cells”, *BMC Biotechnol.* 7, 67 (2007)

- [140] J. Rao, A. Dragulescu-Andrasi, H. Yao, “Fluorescence imaging *in vivo*: recent advances”, *Curr Opin Biotechnol.* 18, 17-25 (2007)
- [141] S. Keren, C. Zavaleta, Z. Cheng, A. de la Zerda, O. Gheysens, and S. S. Gambhir, “Noninvasive molecular imaging of small living subjects using Raman spectroscopy,” *Proc Natl Acad Sci USA.* 105, 5844-5849 (2008)
- [142] C. L. Zavaleta, B. R. Smith, I. Walton, W. Doering, G. Davis, B. Shojaei, M. J. Natan and S. S. Gambhir, “Multiplexed imaging of surface enhanced Raman scattering nanotags in living mice using noninvasive Raman spectroscopy,” *PNAS* 106 (32), 13511–13516 (2009)
- [143] P. Z. McVeigh, R. J. Mallia, I. Veilleux, and B. C. Wilsona, “Widefield quantitative multiplex surface enhanced Raman scattering imaging *in vivo*,” *J. Biomed. Opt.*, 18(4), 046011 (2013)
- [144] B. Jun, M. S. Noh, J. Kim, G. Kim, H. Kang, M. Kim, Y. Seo, J. Baek, J. Kim, J. Park, S. Kim, Y. Kim, T. Hyeon, M. Cho, D. H. Jeong, Y. Lee, “Multifunctional Silver-Embedded Magnetic Nanoparticles as SERS Nanoprobes and Their Applications,” *Small*, 6(1), 119–125 (2010).
- [145] P. Quaresma, I. Os’orio, G. D’oria, P. A. Carvalho, A. Pereira, J. Langer, J. P. Araújo, e I. Pastoriza-Santos, L. M. Liz-Marz’an, R. Franco, P. V. Baptistac, E. Pereira, “Star-shaped magnetite@gold nanoparticles for protein magnetic separation and SERS detection,” *RSC Adv.*, 4, 3659-3667 (2013).
- [146] Allen, T. M., “Ligand-targeted therapeutics in anticancer therapy”, *Nat Rev Cancer* 2, 750–763 (2002)
- [147] G. Destito, R. Yeh, C. S. Rae, M.G. Finn, and M. Manchester, “Folic Acid-Mediated Targeting of Cowpea Mosaic Virus Particles to Tumor Cells”, *Chemistry & Biology* 14, 1152–1162 (2007)
- [148] P. S. Low, and A. C. Antony, “Folate receptor-targeted drugs for cancer and inflammatory disease”, *Adv Drug Deliv Rev* 56, 1055–1058 (2004)
- [149] J. F. Ross, P. K. Chaudhuri, and M. Ratnam, “Differential regulation of folate receptor isoforms in normal and malignant tissues *in vivo* and in established cell lines”, *Physiologic and clinical implications. Cancer* 73, 2432–2443 (1994)

- [150] S. D. Weitman, R. H. Lark, L. R. Coney, D. W. Fort, V. Frasca, V. R. Zurawski, and B. A. Kamen, "Distribution of the folate receptor GP38 in normal and malignant cell lines and tissues", *Cancer Res* 52, 3396–3401 (1992)
- [151] S. Wang, and P.S. Low, "Folate-mediated targeting of antineoplastic drugs, imaging agents, and nucleic acids to cancer cells", *J. Control. Release* 53, 39–48 (1998)
- [152] C. Leamon, and P.S. Low, "Membrane folate-binding proteins are responsible for folate-protein conjugate endocytosis into cultured cells", *Biochem. J.* 291, 855–860 (1993)
- [153] J.A. Reddy, and P.A. Low, "Folate-mediated targeting of therapeutic and imaging agents to cancers", *Crit. Rev. Ther. Drug Carrier Syst.* 15, 587–627 (1998)
- [154] Y. Lu, and P.S. Low, "Folate-mediated delivery of macromolecular anticancer therapeutic agents", *Adv. Drug Deliv. Rev.* 54, 675–693 (2002)
- [155] A. Shakeri-Zadeh, et al., "Cancerous cells targeting and destruction using folate conjugated gold nanoparticles", *Dynamic Biochemistry, (Process Biotechnology and molecular biology* 4, (Special Issue I), 6-12 (2010)
- [156] E. I. Segal, and P. S. Low, "Tumor detection using folate receptor-targeted imaging agents", *Cancer Metastasis Rev* 27, 655–664 (2008)
- [157] Z. Zhang, J. Jia, Y. Lai, et al., "Conjugating folic acid to gold nanoparticles through glutathione for targeting and detecting cancer cells", *Bioorg. Med. Chem.* 18, 5528–5534 (2010)
- [158] X.B. Zhao, and R.J. Lee, "Tumor-selective targeted delivery of genes and antisense oligodeoxyribonucleotides via the folate receptor", *Adv. Drug Deliv. Rev.* 56, 1193–1204(2004)
- [159] S.M. Stephenson, P.S. Low, and R.J. Lee, "Folate receptor-mediated targeting of liposomal drugs to cancer cells", *Methods Enzymol.* 387, 33–50 (2004)
- [160] A.R. Hilgenbrink, and P.S. Low, "Folate receptor-mediated drug targeting: from therapeutics to diagnostics", *J. Pharm. Sci.* 94, 2135–2146 (2005)
- [161] MB Lowry, AM Duchemin, JM, Robinson, and CL Anderson, "Functional separation of pseudopod extension and particle internalization during Fc gamma receptor-mediated phagocytosis", *J Exp Med.* 187, 161–176 (1998)
- [162] B Stella, S Arpicco, MT Peracchia, et al., "Design of folic acid-conjugated nanoparticles for drug targeting", *J Pharm Sci.* 89: 1452–1464 (2000)

- [163] V. Dixit, J. Van den Bossche, D.M. Sherman, D.H. Thompson, and R.P. Andres, "Synthesis and grafting of thioctic acid- PEG-folate conjugates onto Au nanoparticles for selective targeting of folate receptor-positive tumor cells", *Bioconjug. Chem.* 17, 603–609 (2006)
- [164] M.O. Oyewumi, R.A. Yokel, M. Jay, T. Coakley, and R.J. Mumper, "Comparison of cell uptake, biodistribution and tumor retention of folate-coated and PEG-coated gadolinium nanoparticles in tumor-bearing mice", *J. Control. Release* 95, 613–626 (2004)
- [165] D. Pan, J.L. Turner, and K.L. Wooley, "Folic acid-conjugated nanostructured materials designed for cancer cell targeting", *Chem. Commun. (Camb.)* 7, 2400–2401 (2003)
- [166] C. P. Leamon, and P. S., "LowFolate-mediated targeting: from diagnostics to drug and gene delivery", *Drug Discovery Today*, 6, 44–51 (2001)
- [167] C. P. Leamon and P. S. Low, "Cytotoxicity of momordin– folate conjugates in cultured human cells", *Journal of Biological Chemistry*, 267, 24966–24971. (1992).
- [168] S. F. Atkinson, T. Bettinger, L. W. Seymour, J. P. Behr, and C. M. Ward, "Conjugation of folate via gelonin carbohydrate residues retains ribosomal-inactivating properties of the toxin and permits targeting to folate receptor positive cells", *Journal of Biological Chemistry*, 276, 27930–27935 (2001)
- [169] C. P. Leamon, J. A. Reddy, I. R. Vlahov, E. Westrick, A. Dawson, R. Dorton, et al., "Preclinical antitumor activity of a novel folate-targeted dual drug conjugate", *Molecular Pharmaceutics*, 4, 659–667 (2007)
- [170] J. A. Reddy, R. Dorton, E. Westrick, A. Dawson, T. Smith, L. C. Xu, et al., "Preclinical evaluation of EC145, a folate– vinca alkaloid conjugate", *Cancer Research*, 67, 4434–4442 (2007)
- [171] C. P. Leamon, J. A. Reddy, I. R. Vlahov, M. Vetzal, N. Parker, J. S. Nicoson, et al., "Synthesis and biological evaluation of EC72: a new folate-targeted chemotherapeutic", *Bioconjugate Chemistry*, 16, 803–811 (2005)
- [172] W. A. Henne, D. D. Doorneweerd, A. R. Hilgenbrink, S. A. Kularatne, and P. S. Low, "Synthesis and activity of a folate peptide camptothecin prodrug", *Bioorganic & Medicinal Chemistry Letters*, 16, 5350–5355 (2006)
- [173] J. A. Reddy, and P. S. Low, "Enhanced folate receptor mediated gene therapy using a novel pH-sensitive lipid formulation", *Journal of Controlled Release*, 64, 27–37 (2000)

- [174] L. Xu, K. F. Pirollo, W. H. Tang, A. Rait, and E. H. Chang, “Transferrin-liposome-mediated systemic p53 gene therapy in combination with radiation results in regression of human head and neck cancer xenografts”, *Human Gene Therapy*, 10, 2941–2952 (1999)
- [175] X. Q. Pan, X. Zheng, G. Shi, H. Wang, M. Ratnam, and R. J. Lee, “Strategy for the treatment of acute myelogenous leukemia based on folate receptor beta-targeted liposomal doxorubicin combined with receptor induction using all-trans retinoic acid”, *Blood*, 100, 594–602 (2002)
- [176] K. E. Anderson, L. A. Eliot, B. R. Stevenson, and J. A. Rogers, “Formulation and evaluation of a folic acid receptortargeted oral vancomycin liposomal dosage form”, *Pharmaceutical Research*, 18, 316–322 (2001)
- [177] A. Gabizon, H. Shmeeda, A. T. Horowitz, and S. Zalipsky, “Tumor cell targeting of liposome-entrapped drugs with phospholipid-anchored folic acid-PEG conjugates”, *Advanced Drug Delivery Reviews*, 56, 1177–1192 (2004)
- [178] E. J. Roy, U. Gawlick, B. A. Orr, and D. M. Kranz, “Folate-mediated targeting of T cells to tumors”, *Advanced Drug Delivery Reviews*, 56, 1219–1231 (2004)
- [179] Y. Lu, E. Segal, C. P. Leamon, and P. S. Low, “Folate receptor-targeted immunotherapy of cancer: mechanism and therapeutic potential”, *Advanced Drug Delivery Reviews*, 56, 1161–1176 (2004)
- [180] Y. Lu, and P. S. Low, “Folate targeting of haptens to cancer cell surfaces mediates immunotherapy of syngeneic murine tumors”, *Cancer Immunology and Immunotherapy*, 51, 153–162 (2002)
- [181] B. K. Cho, E. J. Roy, T. A. Patrick, and D. M. Kranz, “Single-chain Fv/folate conjugates mediate efficient lysis of folatereceptor- positive tumor cells”, *Bioconjugate Chemistry*, 8, 338–346 (1997)
- [182] A. Quintana, E. Raczka, L. Piehler, I. Lee, A. Myc, I. Majoros, et al., “Design and function of a dendrimer-based therapeutic nanodevice targeted to tumor cells through the folate receptor”, *Pharmaceutical Research*, 19, 1310–1316 (2002)
- [183] J. Y. Lu, D. A. Lowe, M. D. Kennedy, and P. S. Low, “Folate-targeted enzyme prodrug cancer therapy utilizing penicillin- V amidase and a doxorubicin prodrug”, *Journal of Drug Targeting*, 7, 43–53 (1999)

- [184] Y.Bae, W.D. Jang N. Nishiyama, S. Fukushima, and K. Kataoka, “Multifunctional polymeric micelles with folate-mediated cancer cell targeting and pH-triggered drug releasing properties for active intracellular drug delivery”, *Mol. Biosyst.* 1, 242–250 (2005)
- [185] A. Gabizon, A.T. Horowitz, D. Goren, D. Tzemach, F. Mandelbaum- Shavit, M. M. Qazen, and S. Zalipsky, “Targeting folate receptor with folate linked to extremities of poly(ethylene glycol)-grafted liposomes: *in vitro* studies”, *Bioconjug. Chem.* 10, 289–298 (1999)
- [186] S. Salmaso, A. Semenzato, P. Caliceti, J. Hoebeke, F. Sonvico, C. Dubernet, and P. Couvreur, “Specific antitumor targetable beta-cyclodextrin-poly(ethylene glycol)-folic acid drug delivery bioconjugate”, *Bioconjug. Chem.* 15, 997–1004 (2004)
- [187] C. Alix-Panabières, and K. Pantel, “Circulating Tumor Cells: Liquid Biopsy of Cancer. *Clinical Chemistry.* 59, 110-118 (2013)

3. Optical resolution photoacoustic microscopy using novel high-repetition-rate passively Q-switched microchip and fiber lasers

3.1 Introduction

During the last decade remarkable progress has been made in the area of photoacoustic imaging and its biomedical applications. This is due to the demand for safe, high-contrast, and high spatial resolution techniques for the early diagnosis and monitoring of disease. Photoacoustic imaging uses non-ionizing waves which pose no health hazard, compared with ionizing x-ray radiation. Moreover, photoacoustic imaging presents advantages over traditional pure optical and ultrasound imaging techniques. Several groups have developed photoacoustic imaging technologies in different forms[1]. Photoacoustic tomography (PAT) has shown potential to generate images with optical contrast and ultrasonic spatial resolution at significant tissue depths[2][3]. Maslov et al. [4] and Zhang et al. [5] demonstrated dark-field photoacoustic microscopy (PAM), where high-contrast photoacoustic images were produced by raster-scanning a light-delivery and acoustic detection probe mechanically. Advances in PAM and PAT technology include optical detection of photoacoustic signals[6], and the use of ultrasound arrays to improve imaging speed[7], among others. Due to optical contrast, photoacoustic imaging offers considerable opportunities for functional and molecular imaging, including imaging of blood oxygen saturation, imaging of gene expression, and imaging of contrast agents and optically-absorbing nanoparticles [8]. In PAM and PAT, the lateral spatial resolution is determined by the ultrasonic focal width, while the axial spatial resolution is determined primarily by the transducer reception bandwidth.

Recently, a paradigm shift in photoacoustics has abandoned probing deep tissues in favour of pushing the limits of spatial resolution. In this vein Maslov et al [9] demonstrated Optical-Resolution Photoacoustic Microscopy (OR-PAM), where lateral spatial resolution is determined by the size of a focused light spot rather than the width of the ultrasonic focal zone. Because optical focusing is required, the technique is only suitable in the quasi-ballistic regime (to depths of ~1mm in tissue). Xie et al. [10] extended the pioneering work of the L.V. Wang group to introduce laser-scanning optical-resolution photoacoustic microscopy. A fast-scanning mirror was used to scan

the optical spot relative to a fixed ultrasound transducer. OR-PAM has been demonstrated to probe tissue microvasculature and function down to the single capillary level. Because scanning of an optically-focused laser spot is required, the imaging speed of OR-PAM is limited by laser pulse-repetition rate. Present flashlamp-pumped laser systems offer repetition rates of 10-100 Hz while diode-pumped solid-state Q-switched lasers can provide kHz-level repetition rates. These repetition rates are inadequate for real-time frame-rates, which are desirable for clinical applications. Unfortunately, lasers with high-repetition rates (>100 kHz) and suitable pulse durations and energies are not widely available and can be cost-prohibitive and bulky. To solve this problem, we are developing high repetition rate, inexpensive, compact laser sources for realizing high frame-rate photoacoustic imaging. We present experimental data to demonstrate the feasibility of performing high frame-rate OR-PAM with two novel laser sources: a microchip laser (~ 10 kHz repetition rate) and a passively Q-switched fiber laser (>100 kHz repetition rate) [11, 13]. The novel contributions of this paper include: (1) a unique light-delivery probe design with high optical and acoustic efficiency for OR-PAM (2) demonstration of a custom microchip laser for optical-resolution photoacoustic imaging. In conference papers, our group and Billeh [13] et al. recently demonstrated microchip lasers for use in photoacoustic imaging. Billeh [13] et al. also used supercontinuum generation from nonlinear photonic crystal fibers to demonstrate wavelength-tunable photoacoustic imaging. Their work, however, did not quantify spatial resolution and did not demonstrate imaging in optically turbid media. In this article, we demonstrate a custom 532-nm microchip laser-based OR-PAM system and quantify imaging spatial resolution in optically turbid media. (3) We demonstrate for the first time to our knowledge use of a passively Q-switched fiber laser for use in OR-PAM. The microchip and fiber-lasers discussed here are quite inexpensive compared to many competing laser architectures, and could be developed into highly compact and rugged systems, offering the advantage of fiber-coupling. We demonstrate that such lasers have the potential to enable real-time OR-PAM, which could open doors to many significant clinical and biological applications.

3.2 Methods

3.2.1 Probe design

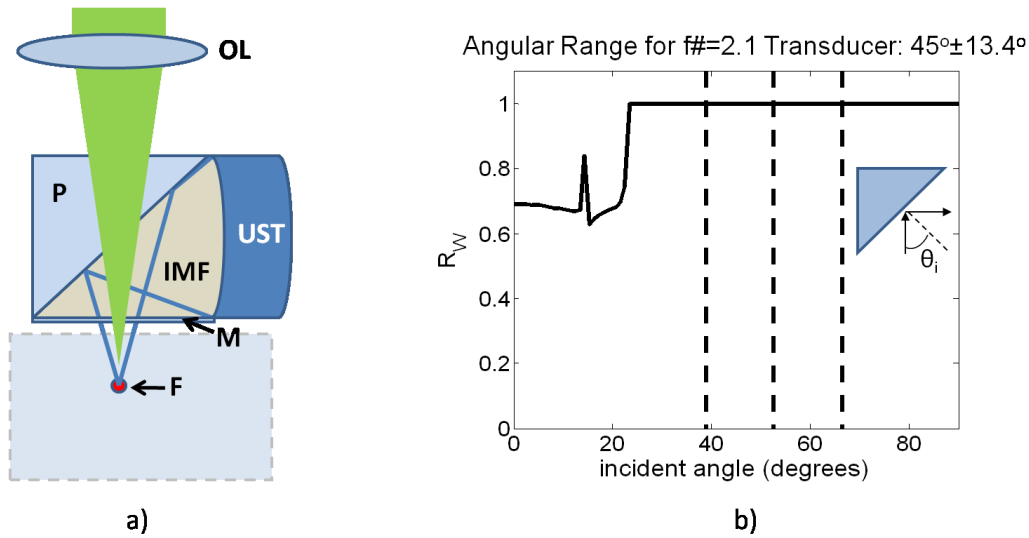


Fig.3.1. (a) Minimal-loss probe design (OL: objective lens, P: prism, IMF: index-matching fluid, UST: ultrasound transducer, M: $\sim 25\text{-}\mu\text{m}$ -thick Saran Wrap membrane, F: focal point of both light and ultrasound). Ultrasound transducer faces a downfacing optical prism such that photoacoustic signals directed upwards to the prism’s diagonal will be deflected to the transducer. An optical index-matching fluid ensures that light can be focused without refraction at the prism’s diagonal interface, and provides a low acoustic-loss medium for acoustic signal propagation. (b) Computed curve of acoustic power reflection coefficient C_w (i.e. fraction of incident power reflected) versus incident angle of ultrasound signal on prism. This calculation was made using the acoustic impedances of the fused silica and index-matching fluid media, as based on the speed of sound in, and density of, these materials. Vertical dashed lines represent the acceptance angles of our transducer (about the optical or acoustic axis).

A low-loss light-delivery and ultrasound detection system is required to enable detection of weak photoacoustic signals. In 2008, Maslov et al. [9] presented a probe with two prisms. This probe successfully achieved focusing gain, minimal path-length in water/tissue, and negligible acoustic attenuation in fused quartz. However, owing to acoustic impedance mismatch, acoustic losses at water-fused quartz interfaces can be high. Additionally, since longitudinal waves are converted to shear waves at liquid-solid interfaces, wave-mode conversion at a prism-fluid 45-degree interface produces further losses. In 2009, Z. Xie et al, [10] designed a probe technique which enabled laser scanning in a photoacoustic microscopy system. They used an unfocused transducer obliquely positioned to receive photoacoustic signals. As a result of the long pathlength in water and the lack of any focal gain, the acoustic and diffractive losses are not negligible, and a low frequency transducer was used, which results in a sacrifice in depth-resolution.

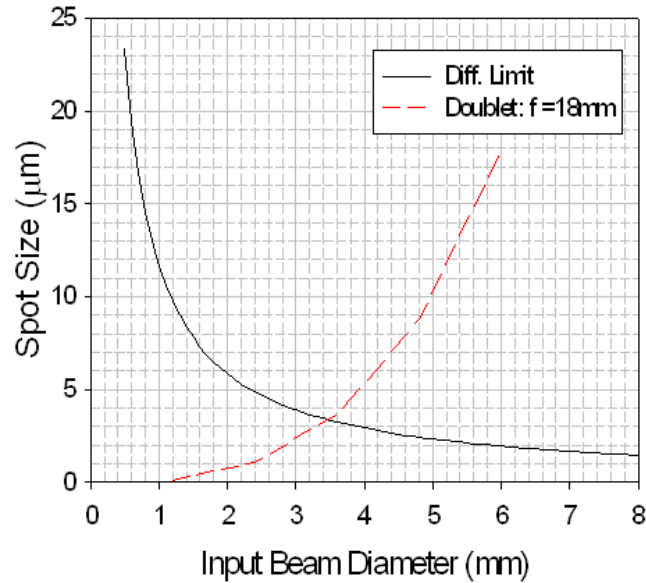


Fig.3.2. To study the effects of the prism-index-fluid layer of Fig.3.1 on the potential optical focusing power of the system, we performed a ray-tracing simulation. We simulated a doublet lens ($f = 18 \text{ mm}$, $\lambda = 532 \text{ nm}$) focusing a top-hat beam through a 1-cm prism-index-fluid slab with air between the lens and the slab. The dashed curve is the spot size at the focus versus input beam diameter. The solid curve represents the spot size possible according to diffraction theory if no aberrating layer were present. The intersection of the curves represents a region where diffraction-limited performance is possible.

In this study, we designed a unique probe with minimal loss which is illustrated in Fig.3.1(a). This probe is somewhat similar to the light-delivery system described by Maslov et al. [9] and is adapted from our previous work [14]. Our ultrasound transducer faces an oblique 10-mm fused silica prism such that photoacoustic signals directed upwards to the prism's diagonal will be deflected to the transducer [14]. Fig.3.1(b) presents the calculation of optical reflectivity of prism versus incident acoustic signal angle. The calculation result shows the reflectivity is almost 100% for incident acoustic signal angles within $45 \pm 13.4^\circ$ (the angular acceptance angles of the transducer) [14][15]. Therefore, all of the acoustic energy is preserved at the prism interface. In our design optical index-matching fluid (Catalog No. 19569, Cargille Labs, Cedar, Grove, New Jersey) is used as ultrasonic coupling, and hence allows for top-down laser illumination to be directed to the tissue surface without optical refractive path variation. The loss caused by acoustic attenuation in index-matching fluid is only slightly more than water [14]. Our probe therefore exhibits minimal loss, which will be critical for sensitive photoacoustic imaging.

In our probe design, to focus the light to a diffraction-limited spot we need to consider the optical aberration, especially due to the prism and matching fluid. In this study, we used the ray-tracing software Beam4 (Stellar Software, Inc, Berkely, CA) to analyze the beam waist as it is focused through a 1-cm slab (modeling the prism and index fluid). In Fig.3.2, the plot based on the Beam4 data is shown for a doublet lens of 18mm focal length (at 532nm). While the input beam diameter to the lens increases, aberrations due to the prism-fluid layer become cubically worse, as measured by the full-width-half-maximum spot size of the beam at the focal waist (dashed line). On the other hand, in a diffraction-limited system without aberrations, the focal spot size decreases with increasing numerical aperture (or input beam diameter), as shown by the solid curve. Diffraction-limited performance may be nearly achieved in the neighbourhood of the intersection of these curves.

3.2.2 Experimental setup with microchip laser

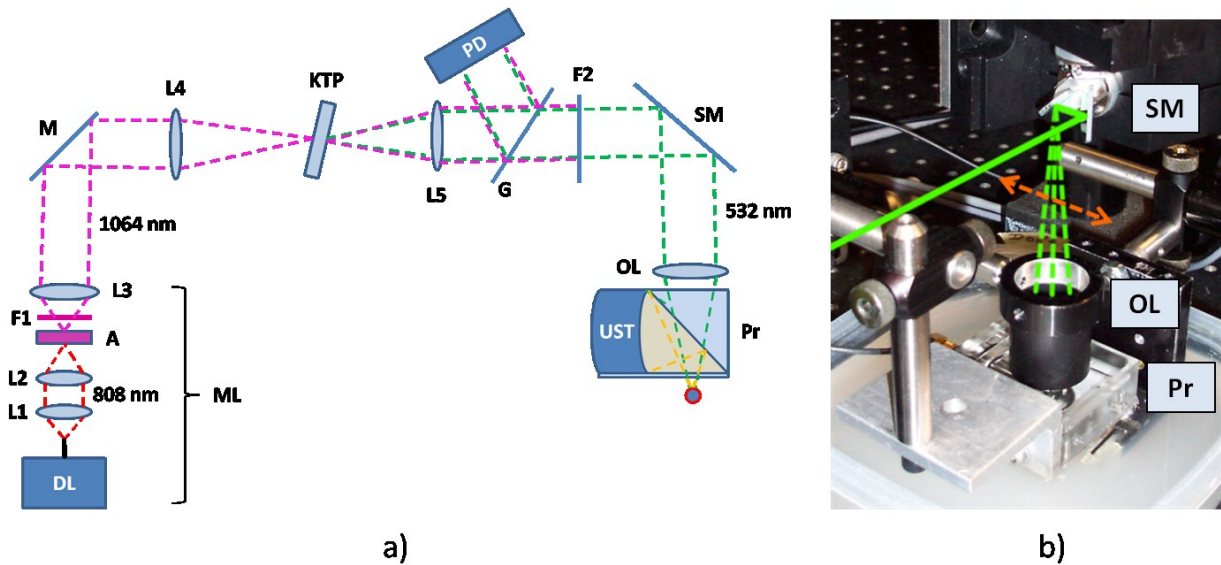


Fig.3.3 (a) Experiment setup for the photoacoustic imaging system employing our microchip laser (ML: microchip laser, DL: diode pump laser, L1: 8-mm lens, L2: 11-mm lens, A: Nd:Cr:YAG microchip, F1: long-pass filter blocking 808 nm pump light, L3: 10-cm lens, M: mirror, L4: 10-cm lens, KTP: KTP frequency-doubling crystal, L5: 30-cm lens, G: glass, PD: photodiode, F2: short-pass filter blocking 1064 nm light, SM: scanning mirror, OL: objective lens, Pr: imaging probe, UST: ultrasound transducer). A diode-pumped Nd: Cr: YAG Micro-chip laser is frequency-doubled by a KTP frequency doubling crystal to 532 nm output. (b) Photograph of the fast-scanning mirror, objective lens, and imaging probe.

The experimental setup for the photoacoustic imaging system employing our microchip laser is illustrated in Fig.3.3(a). The output mode diameter of the 808 nm pump laser was $\sim 100 \mu\text{m}$. Lens 1 of 8-mm focal-length was used for pump collimation. The collimated pump light was focused onto the Nd: Cr: YAG Micro-chip which includes the gain medium and saturable absorber (SA) using 2 lenses of 11-mm focal-length. A long-pass filter 1 was used to block the 808 nm pump light, while 10-cm focal length lenses 3 and 4 were used to focus the laser onto a KTP frequency-doubling crystal. The KTP crystal produces a green 532-nm wavelength output, along with residual fundamental light. This 532-nm wavelength exhibits strong hemoglobin absorption contrast. Although we did not need it for our imaging experiments, we demonstrated amplification of the 1-ns microchip laser pulses to 60 μJ using a large mode-area Yb-doped fiber amplifier. The pulse repetition rate was determined by the power of the microchip laser pump source at 808 nm and may exceed 10 kHz. After collimating the output light from the KTP frequency doubling crystal by 30-cm focal-length lens 5, a glass slide was used to reflect a fraction of the light onto a photodiode which was connected to an oscilloscope (DPO 7054, Digital Phosphor Oscilloscope, Tektronix) as a trigger signal input. Filter 2 was inserted before the scanning mirror system to block incident light at 1064 nm. The scanning mirror system (6230H, Cambridge Technology Inc.) is driven by a function generator (AFG3101, Tektronix Inc.). It can reach 300 Hz at mechanical angles of ± 5 degree although we used much lower rates (3-5 Hz) for our experiments at this time to ensure dense sampling. An 18-mm-focal-length objective lens (NA: 0.15, K16033703, Mitutoyo Co.) was used to focus light through the prism and index-fluid and was positioned ~ 11 cm away from the scanning mirrors. The minimal-loss probe with a 10 MHz ultrasound transducer (19-mm focus, 6-mm active element, $f\# = 3.17$, CD International Inc) was used for photoacoustic signal detection. The photoacoustic signals were amplified by 54 dB using an ultrasound pulse-receiver (5900PR, Olympus NDT Inc). The signals from the photodiode, ultrasound pulse-receiver and the position-feedback signals from the scanning mirror system were recorded by the oscilloscope. The data acquired by the oscilloscope were analyzed by a MATLAB program (Mathworks, Inc). Because the pulse-repetition intervals of the passively Q-switched lasers are somewhat variable, it is important to know where each laser pulse occurs relative to the scanning mirror motion trajectory. To form an image, we register the position of photoacoustic A-scan lines based on the time-location of photo-diode-recorded laser pulses relative to the mirror position-feedback signals.

A calibration curve relating laser-spot location and mirror position (assessed by the feedback signal, which is a function of voltage) is formed by stepping the mirror angle to several fixed intervals then using a micron-precision translation stage to move the position of a carbon-fiber target to the light spot to maximize the photoacoustic signal. Fig.3.3(b) shows a photograph of the scanning mirror, objective lens and probe.

3.2.3 Passively Q-switched fiber laser experimental setup

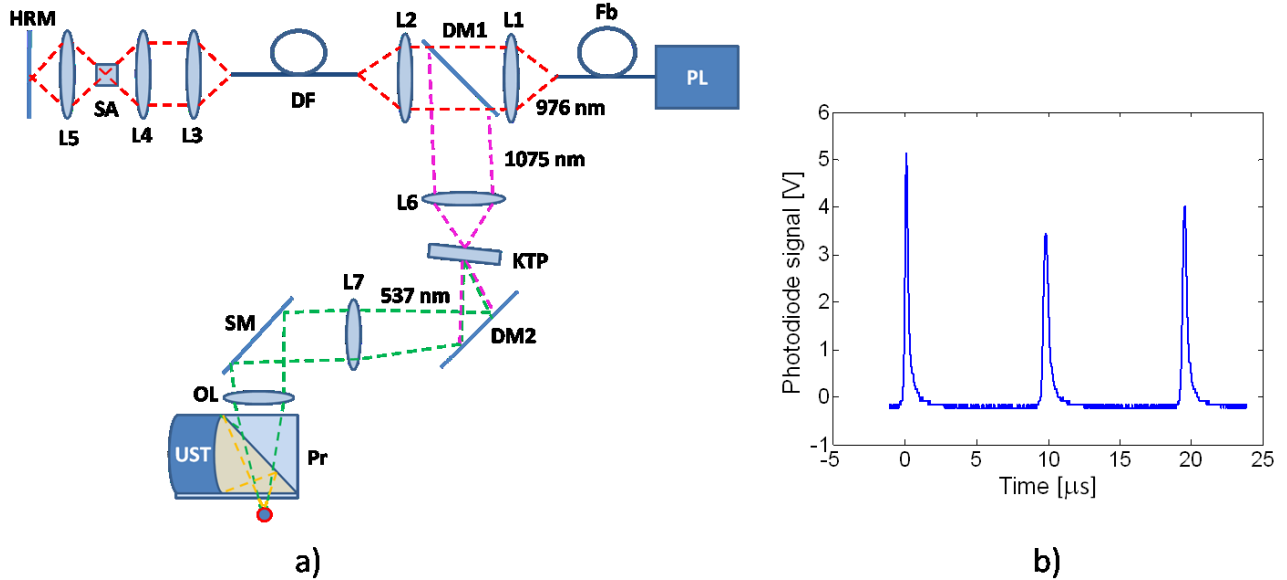


Fig.3.4. (a) Experimental setup for the photoacoustic imaging system employing a fiber laser (PL: pump laser, Fb: fiber, L1:11-mm lens, DM1: dichroic mirror reflecting 1075 nm light, L2:8-mm lens, DF: Yb-doped single mode fiber, L3:6.24-mm lens, L4:15-mm lens, SA: saturable absorber, L5:15-mm lens, HRM: high reflectivity mirror, L6:10-cm lens, KTP: KTP frequency-doubling crystal, DM2: dichroic mirror reflecting 537 nm light, L7:15-cm lens, SM: scanning mirror, OL: objective lens, Pr: imaging probe, UST: ultrasound transducer). A Yb-doped fiber of $\sim 6.5 \mu\text{m}$ mode diameter with an external saturable absorber is pumped by a 976 nm diode laser. The 1075 nm output pulses are coupled out of the laser using a dichroic mirror, and then frequency-doubled with a KTP crystal. The minimal-loss probe with a 10-MHz ultrasound transducer was used for photoacoustic signal detection. (b) Fiber laser signals as measured by a fast photodiode and oscilloscope: 250 ns pulse duration, 100 kHz repetition rate.

Fig.3.4(a) shows the experimental setup for the photoacoustic imaging system employing a novel passively Q-switched fiber laser. As described in previous work [12] by Pan, L. et., the active medium in our fiber laser was a Yb-doped SM DC fiber with core and inner cladding diameters of 6 and 125 μm and core and inner cladding numerical apertures of 0.15 and 0.46, respectively. In our study, however, the length of Yb-doped SM DC fiber was around 5 m instead of 3 m as in previous work, which resulted in a slightly longer pulse duration of ~ 250 ns. The 976 nm pump

light from the fiber coupled diode pump laser (25-W maximum output power) was coupled to the Yb fiber by dichroic mirror 1 with 96% transmission at 976 nm and 99% reflectance at 1075 nm. The SA used in this experiment was a Cr:YAG crystal with transmissions of 30% at 1075 nm. One broadband high-reflectance dielectric mirror and the perpendicularly cleaved fiber end face of the laser medium composed a laser resonator. The other end of the fiber was angle cleaved to avoid feedback. Lens 1 of 11-mm focal length was used for pump light collimation. Lens 2 of 8-mm focal length was used to couple the pump light into the active medium. Lens 3 of 6.24-mm focal length was a collimation lens at the other end of the fiber. The 15-mm focal length lens 4 and lens 5 were used to focus the laser onto the SA. In our experiment, as shown in Fig.3.4(a), the 1075 nm output pulses reflected from the dichroic mirror were frequency-doubled with a KTP crystal. The 10-cm focal length lens 6 was used to focus the laser onto the KTP crystal. Before collimating the output light from the KTP crystal by 15-cm focal-length lens 7, dichroic mirror 2 was inserted to transmit 1075 nm and reflect 537 nm light. The 1075 nm light was detected by a photodiode, which was connected to an oscilloscope for trigger signal input. The pulse-repetition rate was determined by the power of the fiber laser pump source at 975 nm and was 100 kHz for 4.1 W coupled pump power in our experiments. Repetition rates from this laser system up to 300 KHz are demonstrated in [12]. Fig.3.4(b) shows the fiber laser signal. The minimal-loss probe with a 10-MHz ultrasound transducer was used for photoacoustic signal detection.

3.3 Results

3.3.1 Microchip laser experimental results

Without a fiber-amplifier stage the microchip laser produced $\sim 1.84 \mu\text{J}$, 0.6 ns, 1064 nm laser pulses with 7.4 kHz repetition rate at $\sim 1.8\text{W}$ pump power. After frequency doubling and filtering, we obtained $0.21 \mu\text{J}$, 0.6 ns, 532 nm laser pulses, measured after the scanning mirrors and before the objective lens. With our objective lens, the calculated light spot size at the focus is $\sim 6 \mu\text{m}$. A phantom study was performed using $7.5\text{-}\mu\text{m}$ carbon fiber targets positioned 1.5 mm below the probe membrane. To mimic the turbid medium of human tissue (which has a reduced scattering coefficient μ_s' of around 10 cm^{-1}) at 0.5 mm imaging depths, a solution of intralipid was created with $\mu_s' = 3.33 \text{ cm}^{-1}$ to be used at the 1.5 mm depth. This solution was based on a reference intralipid concentration of 20% with measured μ_s and μ_s' of 1674 cm^{-1} and 334 cm^{-1} , respectively.

Oblique-incidence reflectometry was used to perform these scattering measurements [16]. It can be seen from Fig.3.5 that the measured photoacoustic signal amplitudes were around 1.9 V, 1.2 V and 0.9 V, in clear water, turbid media with $\mu_s' = 3.33 \text{ cm}^{-1}$ and turbid media with $\mu_s' = 6.67 \text{ cm}^{-1}$, respectively. Photoacoustic signal FWHMs (full-width-half-maximums) were $8 \pm 2 \text{ }\mu\text{m}$, $11 \pm 2 \text{ }\mu\text{m}$ and $7 \pm 2 \text{ }\mu\text{m}$ in the aforementioned media. The mean photoacoustic signal FWHM in our study (for media ranging from water to turbid media with μ_s' up to 7.94 cm^{-1}) is $9 \pm 2 \text{ }\mu\text{m}$. The measured widths of curves shown in Fig.3.5 are partly due to the width of the carbon fibers themselves. To estimate the true optical resolution, we computed the convolution of a 2D Gaussian beam with a carbon fiber (simulated as a 2D rectangular absorption region). We plot the true FWHM of the Gaussian beam versus the FWHM of the convolution result in Fig.3.6, which shows the corresponding lateral Gaussian Probe spot resolution is $7 \pm 2 \text{ }\mu\text{m}$, which is within error of the predicted spot size of $6 \text{ }\mu\text{m}$.

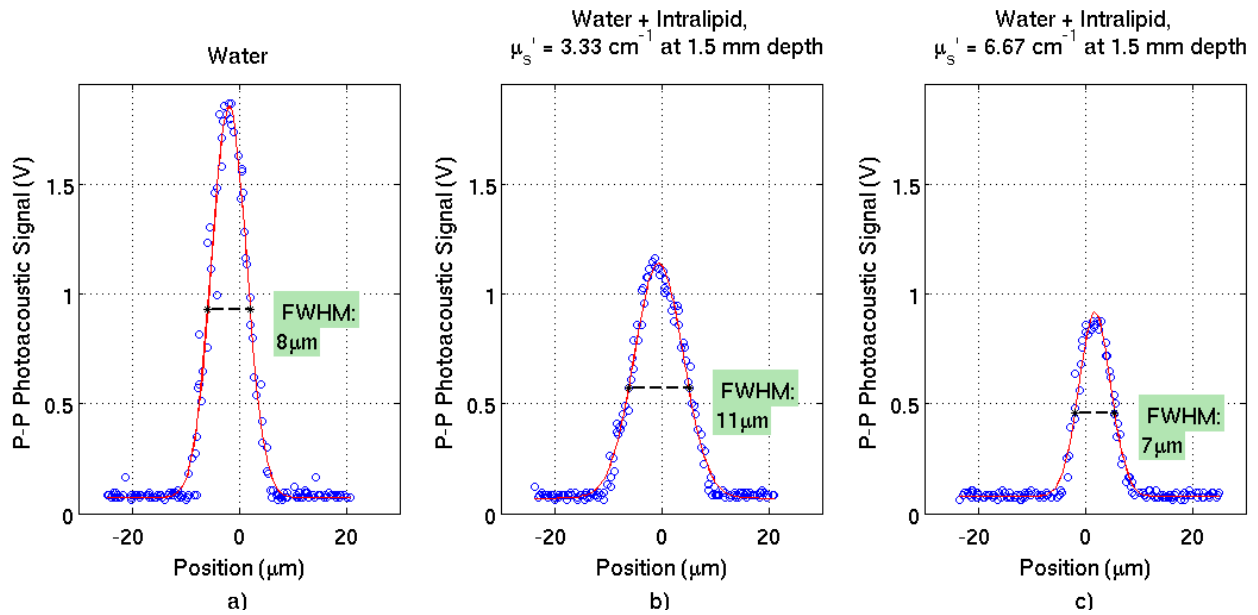


Fig.3.5. Photoacoustic signals (circles) at 1.5 mm depth below the probe membrane with Gaussian fits (lines) (a) in clear water, FWHM = $7.9 \text{ }\mu\text{m}$, amplitude = 1.9 V; (b) in turbid medium with $\mu_s' = 3.33 \text{ cm}^{-1}$, FWHM = $11.3 \text{ }\mu\text{m}$, amplitude = 1.2 V; (c) in turbid medium with $\mu_s' = 6.67 \text{ cm}^{-1}$, FWHM = $7.5 \text{ }\mu\text{m}$, amplitude = 0.9 V.

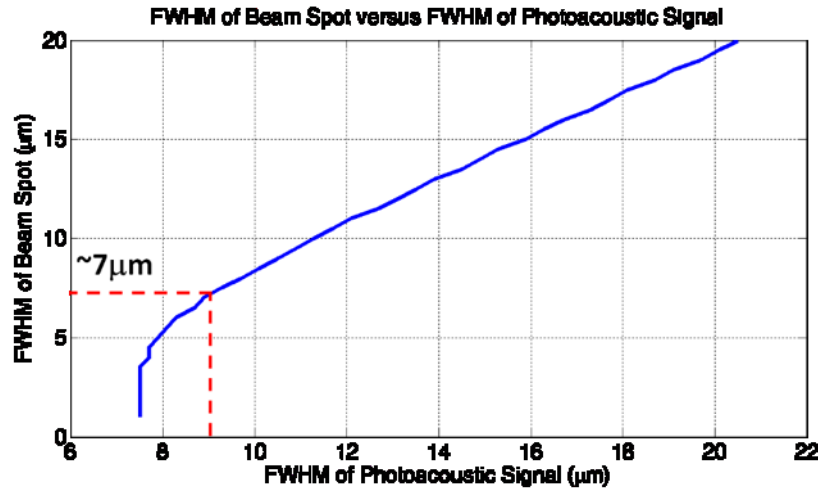


Fig.3.6 Optical resolution as a function of full width at half maximum (FWHM) of measured photoacoustic signal. This plot was generated by taking the convolution of a 2D Gaussian with a rectangle (simulating the beam spot and carbon fiber, respectively). The photoacoustic FWHM is larger than the corresponding beam FWHM due to the non-zero width (7 – 8 μm) of the carbon fiber targets; the true optical resolution of the system is found to be 7 μm for the measured photoacoustic FWHM of 9 μm.

3.3.2 Fiber laser experimental results

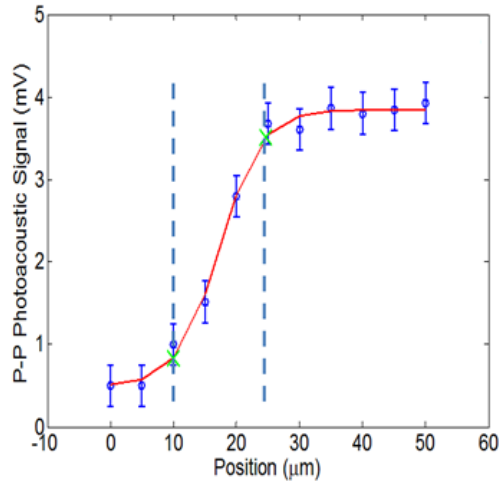


Fig.3.7. Edge-spread function of photoacoustic signal from graphite foil; lateral 10% - 90% PA resolution is $15 \pm 5 \mu\text{m}$.

In our study, the passively Q-switched fiber laser produced $\sim 13 \mu\text{J}$, 250 ns, 1075 nm laser pulses with 100 kHz repetition rates at 4.1 W coupled pump power. The output mode diameter of the single-mode Ytterbium-doped fiber is around $6.5 \mu\text{m}$. After intentional attenuation (via a neutral density filter) and measuring before the objective lens, we obtain a mere $0.06 \mu\text{J}$, 250 ns pulse of

537 nm laser light. Using an objective lens with 18-mm focal length, the calculated light spot size at the focus is $\sim 10 \mu\text{m}$ for the fiber-laser system. To measure the photoacoustic signal resolution in a phantom study, we plot the edge-spread function of the photoacoustic signal, shown in Fig. 3.7, as the optical spot is scanned relative to a graphite foil sample. From the plot, we can see that the photoacoustic resolution is $15 \pm 5 \mu\text{m}$, which is significantly better than the ultrasonic lateral resolution of $\sim 580 \mu\text{m}$.

3.4 Discussion

In our experiments with the microchip laser system the mean spot size on the carbon fiber targets is $7 \pm 2 \mu\text{m}$. With this spot size and $0.21 \mu\text{J}$ pulses the predicted fluence is 546 mJ/cm^2 , which is comparable to that found in other OR-PAM experiments[9][10], but above the ANSI limit for laser exposure to human skin. In our experiments with the fiber laser system, the photoacoustic resolution is $15 \pm 5 \mu\text{m}$. This corresponds to a fluence of roughly 20 mJ/cm^2 , which is the ANSI limit for pulsed laser exposure to human skin. As demonstrated with the above two laser systems, lower fluences can be used at the expense of signal-to-noise ratio.

One disadvantage present in both the laser systems used here is irregular pulse repetition intervals, which is a consequence of passive Q-switching. This should not be a significant problem for many photoacoustic imaging applications, however, as data acquisition is typically triggered off of photodiode signals. It could be problematic in cases where synchronization of the laser pulse-repetition clock and the clock of the data acquisition system with minimum jitter is required, such as with photoacoustic flow imaging. Use of polarization maintaining doped fibers could improve pulse-to-pulse energy stability, and improve frequency doubling efficiency; our fiber laser system did not use polarization maintaining fibers, principally to minimize cost.

The fiber laser based OR-PAM system displayed poor photoacoustic signal-to-noise ratio, making it necessary to use time-averaging when recording data; this is undesirable for real-time imaging purposes. One possible cause of the weak photoacoustic signals is that the pulse-width of the fiber laser, which is quite long, may violate thermal and stress-confinement conditions for efficient photoacoustic signal generation. Additionally, the excitation due to such long pulses may produce photoacoustic signals with frequency characteristics which are too low for our present 10-MHz transducer (the equivalent bandwidth of the 250-ns pulse-width is $\sim 2 \text{ MHz}$). Therefore it

may be advantageous to use a lower frequency transducer, which could improve signal to-noise at the expense of axial resolution. This trade-off may be tolerable since the depth-of-field of the optical focus can potentially be made very tight so that axial resolution is optically-defined rather than acoustically-defined. Future work may build on recent developments in exploiting distributed Stimulated Brillouin Scattering to produce sub-nanosecond pulses [17], or may use seeding pulses from diode-laser sources.

3.5 Conclusion

In our studies on photoacoustic imaging systems with a microchip laser and a fiber laser, we have demonstrated: a) a unique probe design with minimal loss; b) a unique microchip laser which is highly compact and potentially inexpensive; c) a fiber laser which is also potentially inexpensive and should offer considerable advantages due to fiber coupling. The microchip laser's repetition rate is around 7.5 kHz and can be increased to 30 kHz at the expense of pulse energy, while the passively Q-switched fiber laser's repetition rate can range between 100 – 300 kHz, which is the suitable range for real-time OR-PAM imaging (for a 1-mm by 1-mm imaging area scanned with a lateral resolution of 15 μm and a real-time scanning rate of 30 frames per second, a laser pulse repetition rate of ~ 130 kHz is required). Both laser systems can potentially be miniaturized to a shoe-box size apparatus. The above photoacoustic systems present optically-defined lateral resolution of around 7 μm and 15 μm respectively, which is over 33 times higher than that of ultrasound resolution. All these results show that these systems have adequate laser parameters in terms of energy, spatial resolution, and repetition rate to be used for real-time optical-resolution photoacoustic microscopy.

Bibliography

- [1] L.V. Wang, Photoacoustic Imaging and Spectroscopy (CRC, 2009)
- [2] G. Ku, and L. V. Wang, “Deeply penetrating photoacoustic tomography in biological tissues enhanced with an optical contrast agent”, *Optics Letters* 30 (5), 507(2005).
- [3] S.A. Ermilov, T. Khamapirad, A. Conjusteau, M.H. Leonard, and R. Lacewell, “Laser optoacoustic imaging system for detection of breast cancer”, *Journal of Biomedical Optics* 14(2), 24007 (2009)
- [4] K. Maslov, G. Stoica, and L. H., V. Wang, “*In vivo* dark-field reflection-mode photoacoustic microscopy”, *Optics Letters* 30, 625 (2005)
- [5] H. F.Zhang, K. Maslov, G. Stoica, and L. H., V. Wang, “Functional photoacoustic microscopy for high-resolution and noninvasive *in vivo* imaging”, *Nature Biotechnology* 24, 848 (2006).
- [6] E. Zhang, J. Laufer, and P. Beard, “Backward-mode multiwavelength photoacoustic scanner using a planar Fabry-Perot polymer film ultrasound sensor for high-resolution three-dimensional imaging of biological tissues”, *Applied Optics* 47, 561(2008)
- [7] R.J. Zemp, L. Song, R. Bitton, K.K Shung, and L.V. Wang, “*In vivo* realtime photoacoustic microscopy with a 30-MHz ultrasound array transducer”, *Optics Express* 16 (11), 7915(2008)
- [8] L. Li, R. J. Zemp, G. Lungu, G. Stoica, and L. H. V. Wang, “Photoacoustic imaging of lacZ gene expression *in vivo*”, *Journal of Biomedical Optics* 12, 020504(2007)
- [9] K. Maslov, H. F. Zhang, S. Hu, and L. H. V. Wang, “Optical-resolution photoacoustic microscopy for *in vivo* imaging of single capillaries”, *Optics Letters* 33, 929 (2008).
- [10] Z. X .Xie, S. L. Jiao, H. F. Zhang, and C. A. Puliafito, “Laser-scanning optical-resolution photoacoustic microscopy”, *Optics Letters* 34, 1771 (2009).
- [11] L. Pan, I. Utkin, and R. Fedosejevs, “Two-wavelength passively Q-switched ytterbium doped fiber laser”, *Optics Express* 16, 11858 (2008)
- [12] L. Pan, I. Utkin, and R. Fedosejevs, “Passively Q-switched ytterbium-doped double-clad fiber laser with a Cr⁴⁺: YAG saturable absorber”, *IEEE Photonics Technology Letters* 19, 1979 (2007)
- [13] Y.N. Billeh, M.Y. Liu, and T. Buma, “Multispectral photoacoustic microscopy using a photonic crystal fiber super-continuum source”, *Proc. SPIE*, Vol. 7564, 75642T (2010)

- [14] J. C. Ranasinghesagara, Y. Jian, X. H. Chen, K. Mathewson, and R. J. Zemp, "Photoacoustic technique for assessing optical scattering properties of turbid media", *Journal of Biomedical Optics* 14, 040504 (2009)
- [15] R. S. C. Cobbold, *Foundations of Biomedical Ultrasound* (Oxford University Press, Inc., New York, 2007)
- [16] S.-P Lin, L.V. Wang, S. L. Jacques, and F. K. Tittel, "Measurement of tissue optical properties using oblique incidence optical fiber reflectometry", *Applied Optics* 36, 136 (1997)
- [17] L. Pan, I. Utkin, R.J. Lan, Y. Godwal, and R. Fedosejevs, "High peak power sub-nanosecond passively Q-switched ytterbium doped fiber laser", *Opt. Lett.* 35 (7) 895 (2010)

4 *In vivo* near-realtime volumetric optical-resolution photoacoustic microscopy using a high-repetition-rate nanosecond fiber-laser

4.1 Introduction

Photoacoustic imaging is an emerging technology that involves firing short laser pulses into tissue and recording acoustic signals due to light absorption-induced thermoelastic expansion. Image contrast is principally due to optical absorption. High-resolution photoacoustic imaging has captured considerable attention in the imaging community as its utility is extending to areas of interest to biologists and clinicians. One embodiment, termed Dark-Field Photoacoustic Microscopy (PAM) [1] achieves high resolution by using a mechanically-scanned high frequency, high numerical aperture single-element ultrasonic transducers to receive photoacoustic signals. In 2006, Zhang et al. [2] reported a lateral resolution of 45 μm at a maximum depth of 3 mm by using a 50 MHz focused ultrasonic transducer to demonstrate functional imaging of hemoglobin oxygen saturation. To realize micron-scale acoustic resolution, the transducer frequency would need to be in the hundreds of MHz to GHz range, where penetration depth is limited to less than $\sim 100 \mu\text{m}$ due to high ultrasonic attenuation in tissue at high frequencies. An alternative technology to achieve high resolution is referred to as Optical-Resolution Photoacoustic Microscopy (OR-PAM). OR-PAM is capable of realizing high optical resolution images because its lateral spatial resolution is determined by the focused optical spot size (limited by the diffraction-limited focal spot size) rather than the width of the ultrasound focal zone. OR-PAM systems are depth-limited to approximately one transport mean-free path ($\sim 1 \text{ mm}$ in tissue). Because of multiple scattering, diffraction-limited focusing is difficult to achieve past this depth. Beginning with the work of Maslov et al. [3], OR-PAM has been used for structural [4] and functional [4-8] imaging in mice. Oxygen saturation imaging, and imaging of blood velocity has been demonstrated [6][7], and stunning trans-cranial images of whole-brain murine cortical capillary networks have shown the potential power of the technique for neuro-functional imaging [8]. Other applications have included *in vivo* imaging of amyloid plaques in a transgenic murine model of Alzheimer's disease [9], high-resolution functional imaging and chronic monitoring of angiogenesis in a transgenic mouse model [10], ocular microvasculature [11], and others. E. Zhang et al [12] demonstrated a

unique Fabry-Perot etalon-based approach for OR-PAM. Xie et al. [13], developed a laser-scanning OR-PAM (LS-OR-PAM) system based on the pioneering work of L.V. Wang's group. In Xie's studies, a lateral resolution of 7.8 μm in a 6 mm-diameter circular field-of-view (FOV) was achieved.

For clinical applications, OR-PAM should be developed into a realtime technique. Unfortunately, present volumetric OR-PAM systems have low imaging frame-rates. Since the separation between successive pixels within the image area should be no bigger than the optical spot size, even a relatively small image area $<1 \text{ mm} \times 1 \text{ mm}$ requires tens of thousands of PA signals (A-scan lines) for each frame. Laser PRR and/or high scanning speeds are thus keys to high imaging frame-rates. Recently, Wang et al. [14], reported a real-time OR-PAM B-scan imaging system with voice-coil scanning speed up to 40Hz over a 1mm range or 20 Hz over 9mm. The LS-OR-PAM system described by Xie et al. showed no frame-rate advantages over previous OR-PAM systems due to limitations of the laser PRR. Presently, the PRR of flashlamp-pumped laser systems can reach 10-100 Hz while that of diode-pumped solid-state Q-switched lasers is at kHz range. For real-time volume-scanning frame-rates which are desirable for clinical applications, these repetition rates are still not high enough. Recently we demonstrated the use of custom-built passively Q-switched microchip (10's of kHz PRRs) and fiber lasers (100's of kHz PRRs) operating at the frequency-double wavelength of 532-nm for OR-PAM [15]. Since then, Wang et al. [16], reported a 50-kHz fiber-laser operating at 1064nm for OR-PAM. Unfortunately, optical absorption of hemoglobin at 1064nm is comparatively low. Here we present experimental data to demonstrate the feasibility of performing high frame-rate OR-PAM by employing 532-nm fiber laser source with high repetition rate of up to 600 kHz. Combined with a fast-scanning mirror oscillating at 800 (B-scan) lines per second, we demonstrate an OR-PAM system capable of volumetric imaging at 4 fps. The imaging frame-rate can be higher if the FOV is sacrificed. This imaging speed may be adequate for some clinical applications and is one to two orders of magnitude faster than previous systems. Besides frame-rate advantages, we use a unique light-delivery acoustic probe system. Previous laser-scanning OR-PAM systems used an unfocused transducer positioned a significant distance from the sample to collect photoacoustic signals. Signal attenuation, diffraction and lack of transducer focal gain are significant disadvantages of this technique. In contrast, other OR-PAM systems use clever probe designs [17] to attain high

numerical aperture focusing, offering considerable signal-to-noise advantages, but relying on mechanical scanning of the probe, limiting frame-rates. In our approach, we combined the signal-to-noise-ratio-advantages of focused transducers with the speed advantages of laser-scanning by using a unique low-loss light-delivery and ultrasound-detection probe. A laser-spot from our high-repetition-rate fiber laser is scanned across the focal zone of the ultrasound transducer. Due to our near realtime imaging frame-rates, our system may pave the way to more widespread acceptance by biologists and clinicians, and provide new opportunities for studying dynamic processes in clinical and pre-clinical settings.

4.2 Methods

The system diagram for our unique system is shown in Fig.4.1. Laser pulses are generated by a diode-pumped pulsed Ytterbium-doped fiber laser (GLP-10, IPG Photonics Corporation.) with PRR ranging from 20 kHz - 600 kHz. The 1064-nm fundamental wavelength is frequency-doubled to 532-nm via a built-in compact laser head with output collimator for free-space light delivery. Laser pulse widths are ~ 1 ns and pulse energies are programmable up to 20 μ J by adjusting the amplifier pump power, referred to by the manufacturer as the set-point. A glass slide was inserted in the beam path to reflect a small amount of light onto a high speed custom photodiode, used for triggering and pulse-to-pulse energy normalization if required. Raster scanning is realized by using a 2D galvanometer scanning mirror system (6230H, Cambridge Technology Inc.) with XY mirrors driven by analog sinusoidal signals from two function generators (AFG3101, Tektronix Inc.). The scanning speed of each mirror can reach hundreds of Hz depending on the scanning angles required. The amplitude of the function generator output determines the maximum scanning angle, which in-turn determines the FOV in the image. An 18-mm-focal-length objective lens was positioned ~ 3.6 cm below the centers of the scanning mirrors to focus light through our unique light-delivery probe adapted from our previous work [15][18]. As seen in Fig.4.1, a 10 MHz focused ultrasound transducer (19-mm focus, 6-mm active element, $f\#=3.17$, CD International Inc) faces a downfacing 10-mm optical prism which reflects the upward photoacoustic signals to the transducer [18]. The acoustic reflectivity is almost 100% for the incident acoustic signal angle within the angular acceptance angles of the transducer [18]. The optical index-matching fluid (Catalog # 19569, Cargille Labs, Cedar, Grove, New Jersey) used for ultrasonic coupling, allowed top-down laser illumination to be directed to the tissue surface without optical refractive path variation. Acoustic

attenuation of this fluid was measured to be only slightly higher than that of water [18]. A thin transparent plastic membrane was used to hold the index-fluid in place using O-rings to make a water-tight seal.

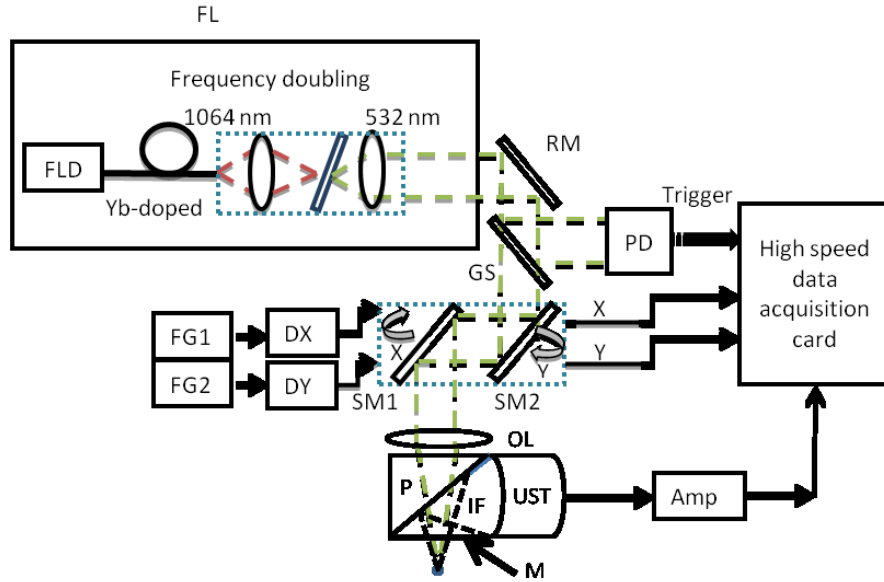


Fig 4.1. Experiment setup for the photoacoustic imaging system with focused transducer (FL: fiber laser; FLD: fiber laser driver; RM: high reflectivity mirror; GS: glass slide; PD: photodiode; FG1, FG2: function generator; DX, DY: galvanometer scanning mirror driver; SM1, SM2: scanning mirror; OL: 18-mm objective lens; P: prism; IF: index-matching fluid; M: membrane; UST: ultrasound transducer; Amp: amplifier). A diode-pumped pulsed Ytterbium fiber laser generates 532 nm output. A glass slide was inserted to reflect some light into high speed photodiode detector. We used 2D fast scanning mirrors and an objective lens to realize scanning and focusing. We used a uniquely designed minimal-loss probe with a 10 MHz ultrasound transducer (US-TX) for photoacoustic signal detection.

An eight channel PCI data acquisition card (CS8289, Gage Cobra, Gage Applied Systems, Inc.) with 12-bit dynamic range and up to 125 MSamples/s sample rate was used to acquire the photodiode signal (to trigger data acquisition), the feedback positions of the scanning mirrors (to determine laser spot position on the image plane), and the photoacoustic signals which were detected by an ultrasonic transducer, and amplified by an ultrasound pulser-receiver (5900PR, Olympus NDT Inc). Further data processing and analysis were conducted by using MATLAB programs (Mathworks, Inc) in the data acquisition PC.

4.3 Results

Fig.4.2(a) shows a maximum-amplitude-projection (MAP) image of a human hair target positioned 1.5mm below the probe membrane in a clear medium. By setting the 2D scanning

galvanometer mirror system with scanning frequencies of 2 Hz and 400 Hz in the Y direction (slow scanning axis) and X direction (fast scanning axis), respectively at optical angles within ± 1.6 degrees, the OR-PAM system realized raster scanning at 4 fps. The image in Fig.4.2(a) shows the target diameter of around 100 μm which is roughly the size of a hair. For resolution studies, an MAP image of a $\sim 7.5\text{-}\mu\text{m}$ carbon fiber target positioned ~ 1.5 mm below the probe membrane was obtained as shown in Fig.4.2 (b). To analyze the photoacoustic signal resolution, we extracted out a slice of data on the image perpendicular to the carbon fiber. The circles in Fig.4.2 (c) indicate the photoacoustic signals along the slice direction, and the line curve is its Gaussian fitting which shows the photoacoustic signal full width at half maximum (FWHM) as ~ 9 μm . Since the measured FWHM shown in Fig.4.2 (c) are partly due to the width of the carbon fiber itself, we computed the convolution of a 2D Gaussian beam with a carbon fiber (simulated as a 2D rectangular absorption region) [15], which shows the corresponding lateral resolution as $\sim 7\mu\text{m}$.

For *in vivo* studies, we used pulse energies of ~ 0.15 μJ (measured after the scanning mirror system). While 4 fps were achieved in phantom studies, we chose to image a larger field of view ($1\text{ mm} \times 1\text{ mm}$) for *in-vivo* studies. We set the 2D scanning galvanometer mirror system with scanning frequency in Y direction as 1 Hz, and in X direction as 400 Hz at optical angles of ± 1.6 degrees, which enabled raster scanning at 2 fps. Frame-rates for this FOV are limited by the fast-scanning mirror system but higher frame-rates are possible for smaller field of view. All experimental animal procedures were conducted in conformity with the laboratory animal protocol approved by the University of Alberta Animal Use and Care Committee. The Swiss Webster mouse was anesthetized using a breathing anesthesia system (E-Z Anesthesia, Euthanex Corp.) during image acquisition. Fig.4.3 shows snapshots from 2 volumetric images of the microvasculature in a Swiss Webster mouse ear *in vivo*. The volumetric images were processed by using 3D Vesselness filtering [19] and displayed using Volview software (Kitware, Inc., Volview 3.2). Fig.4.3(a) clearly depicts a pair of parallel arteries or veins surrounded by many capillaries, while a corresponding volumetric rendering is shown in Video 1. Fig.4.3(b) shows another snapshot with photoacoustic signal FWHM of ~ 6 μm obtained from resolution studies, while a corresponding volumetric rendering is shown in Video 2.

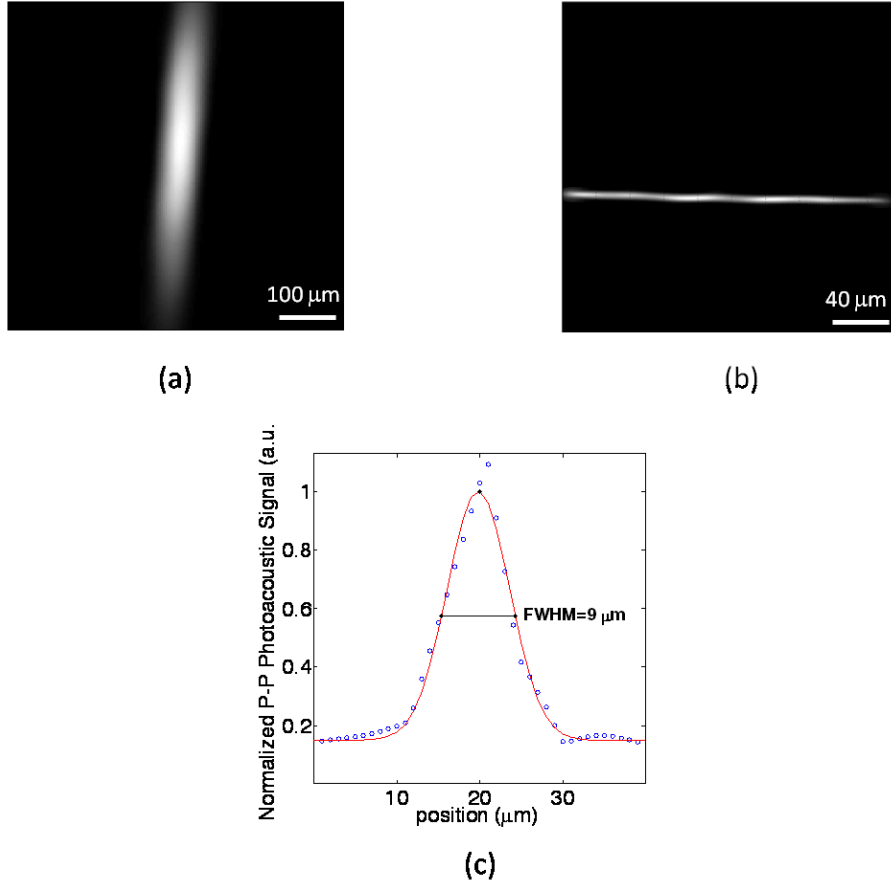


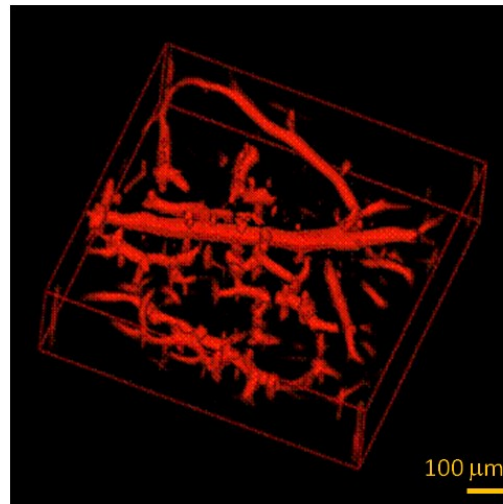
Fig.4.2. (a) Image of a human hair; (b) Image of a 7.5- μm carbon fiber target positioned 1.5 mm below the probe membrane; (c) Photoacoustic signal (circles) of a slice of data selected perpendicular to the carbon fiber on 2D image with Gaussian fit (line) in clear water, FWHM = 9 μm .

4.4 Discussion

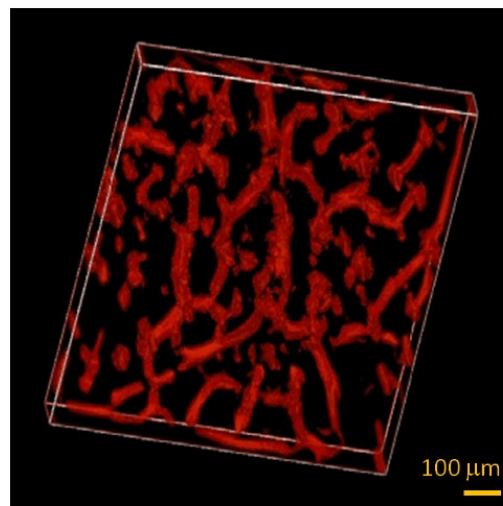
In our studies on photoacoustic imaging systems with fiber laser, we have demonstrated an OR-PAM system with lateral resolution of $\sim 6\mu\text{m}$, which is close to the objective lens diffraction-limited focal spot size of $\sim 4.3\mu\text{m}$ at 532 nm. A smaller optical focal spot size can be achieved by using an objective lens with higher numerical aperture; however, this would require adjustment of the light delivery system.

Also, our OR-PAM system is capable of C-scan and 3D imaging at 4 fps by using a high PRR 532 nm fiber laser and a high speed 2D galvanometer mirror system. Our *in vivo* images have a FOV of $1\text{ mm} \times 1\text{ mm}$, with an average pixel size of $2.5\mu\text{m} \times 2.5\mu\text{m}$, imaged at a frame-rate of 2 fps. Recently, Hu et al. [20] reported second-generation optical-resolution photoacoustic

microscopy which takes 70 min. for $7.8 \text{ mm} \times 10 \text{ mm}$ FOV at a pixel size of $2.5 \mu\text{m} \times 2.5 \mu\text{m}$. Taking into account the different number of pixels in each image, our setup would be on the order of $100\times$ faster. Ref. [16] uses a 50 kHz fiber laser ($25\times$ faster than previous dye-laser-based systems but $12\times$ slower than our 600 kHz maximum repetition-rate laser), however their imaging frame rates are further limited by mechanical scanning and some signal averaging due to the lower signal strength at 1064nm.



(a)



(b)

Fig.4.3. (a) *in vivo* image of microvasculature in a Swiss Webster mouse ear acquired at 2 fps, which shows an image of a pair of parallel arteries or veins surrounded by capillaries; Video 1 shows the volumetric visualization of the Swiss Webster mouse ear microvasculatures by OR-PAM; (b) Another *in vivo* image of microvasculature in a Swiss Webster mouse ear; Video 2 shows corresponding volumetric visualization of the Swiss Webster mouse ear microvasculature.

The diode-pumped pulsed Ytterbium fiber laser with PRR ranging from 20 to 600 kHz is of compact size, potentially inexpensive, and should offer considerable advantages due to fiber coupling. It should be noted that the distance traveled by photoacoustic signals during the time between laser pulses at 600 kHz PRF is ~ 2.5 mm, only slightly more than the optical transport mean-free path (which defines the penetration depth of OR-PAM). Hence, repetition-rates much higher than this may be complicated by deep-tissue signals from previous pulses interfering with those due to superficial structures.

The pixel separations along the Y-axis were determined by the ratio of the fast axis scanning speed over the slow axis scanning speed. The maximum scanning speed of around 500 Hz within optical angles of ± 1.6 degrees limits the maximum frame rate to 2.5 fps for an image area of 1 mm \times 1 mm at average pixel pitch of around 2.5 μ m. We chose not to push these scanning-speed limits to prevent heat buildup in the galvanometer system. If active cooling higher speed 2D galvanometer mirror systems are used, with our fiber laser operating at its maximum PRR of 600 kHz, this system is capable of achieving a maximum frame rate of ~ 15 fps at an average pixel pitch of 2.5 μ m for an image size of 500 μ m \times 500 μ m, which provides near-realtime volumetric imaging. Realtime or near-realtime frame-rates will be possible in the near future, which will permit clinical applications.

For our 2 fps *in vivo* images, each 3D frame takes nearly 96 Mbytes. This is calculated as follows: we used 100 samples per A-scan, and 160,000 laser-shots per 3D image (with laser repetition rate of 320 kHz at 2 fps, with a higher number of laser shots needed for 600 kHz PRR). Note that we also acquire position feedback signals and laser-diode signals for a total of 4 channels. Thus each frame requires $(100 \times 160,000 \times 4)$ samples/image \times 12 bits/sample / (8 bits/byte) = 96 Mbyte/image. Since we have only 128 Mbytes on-board storage capacity we are limited in the number of frames we can acquire before transferring data to the PC RAM. To sustain realtime imaging rates, very high data transfer rates between the data acquisition card and the PC RAM are required and these transfer rates are beyond the capabilities of our current hardware. Future work will aim to store only peak-to-peak values, reduce the number of data channels required, increase the onboard RAM, and use higher data-throughput data acquisition hardware for sustained realtime acquisition and display.

In our *in vivo* studies, the laser pulse energy was tuned to 0.15 μJ . Assuming that the depth of the laser focus is $\sim 120\ \mu\text{m}$ below the tissue surface, the calculated surface laser fluence is 18 mJ/cm^2 , which is less than the 20 mJ/cm^2 safety standard set by American National Standards Institute (ANSI) [21], also less than that reported in other OR-PAM studies [20]. The average power delivered to a $1\ \text{mm} \times 1\ \text{mm}$ FOV using the maximum laser PRR is $\sim 9\ \text{W}/\text{cm}^2$, significantly higher than the 100 mW/cm^2 (ANSI-recommended exposure for CW light delivery), but comparable to other *in vivo* microscopy methods such as fluorescence confocal microscopy. In addition, focal peak power densities (assuming lossless focusing) of 540 MW/cm^2 are still less than those used in 2-photon microscopy [22]. In our work, light delivery is confined to a localized area and no tissue damage is visible after imaging.

Future work will involve demonstrating imaging of dynamic processes, minimizing the channel count and system complexity by eliminating mirror position feedback, increasing the imaging FOV, developing multi-wavelength high-repetition-rate sources for functional imaging by using nonlinear photonic crystal fibers [23] or Raman shift crystals, exploring nonlinear photoacoustic phenomena for single-wavelength functional imaging, minimizing the system footprint [24] and expanding clinical and biological applications.

Bibliography

- [1] K. Maslov, G. Stoica, and L. H. V. Wang, “*In vivo* dark-field reflection-mode photoacoustic microscopy”, *Opt. Lett.* 30, 625-627 (2005)
- [2] H. F. Zhang, K. Maslov, G. Stoica, and L.-H. Wang, “Functional photoacoustic microscopy for high-resolution and noninvasive *in vivo* imaging”, *Nature Biotechnol.* 24, 848–851 (2006)
- [3] K. Maslov, H. F. Zhang, S. Hu, and L. H., V. Wang, “Optical-resolution photoacoustic microscopy for *in vivo* imaging of single capillaries”, *Opt. Lett.* 33, 929-931 (2008)
- [4] S. Hu, K. Maslov, and L. V. Wang, “Noninvasive label-free imaging of microhemodynamics by optical-resolution photoacoustic microscopy”, *Opt. Express* 17, 7688–7693 (2009)
- [5] S. Hu, K. Maslov, V. Tsytsarev, and L. V. Wang, “Functional transcranial brain imaging by optical-resolution photoacoustic microscopy”, *J. Biomed. Opt.* 14, 040503 (2009)
- [6] S. Hu, K. Maslov, and L. V. Wang, “*In vivo* functional chronic imaging of a small animal model using optical-resolution photoacoustic microscopy”, *Med. Phys.* 36, 2320–2323 (2009)
- [7] L. Song, K. Maslov, and L. V. Wang, “Multifocal optical-resolution photoacoustic microscopy *in vivo*”, *Opt. Lett.* 36, 1236-1237 (2011)
- [8] J. Yao, K. Maslov, Y. Shi, L. Taberand L. V. Wang, “*In vivo* photoacoustic imaging of transverse blood flow using Doppler broadening of bandwidth,” *Opt. Lett.*, 35(9): 1419–1421 (2010)
- [9] S. Hu, P. Yan, K. Maslov, J.M. Lee, and L. H., V. Wang, “Optical-resolution photoacoustic microscopy of amyloid- β deposits *in vivo*”, *Proc. SPIE* 7564, 75643D (2010).
- [10] S. Hu, J. Yao, K. Maslov, and L. H., V. Wang, “Optical-resolution photoacoustic microscopy of angiogenesis in a transgenic mouse model”, *Proc. SPIE* 7564, 756406 (2010).
- [11] S. Hu, B. Rao, K. Maslov, and L. H., V. Wang, “Label-free Photoacoustic Ophthalmic Angiography”, *Opt. Lett.* 35(1), 1–3 (2010)
- [12] E. Zhang, and P. Beard, “Ultra high sensitivity, wideband Fabry Perot ultrasound sensors as an alternative to piezoelectric PVDF transducers for biomedical photoacoustic detection”, *Proc. SPIE* 5320, 222-229 (2004)
- [13] Z. X. Xie, S. L. Jiao, H. F. Zhang, and C. A. Puliafito, “Laser-scanning optical-resolution photoacoustic microscopy”, *Opt. Lett.* 34, 1771-1773 (2009).

- [14] L. Wang, K. Maslov, J. Yao, B. Rao, and L. H., V. Wang, “Fast voice-coil scanning optical-resolution photoacoustic microscopy”, *Opt. Lett.* 36, 139-141 (2011).
- [15] W. Shi, S. Kerr, I. Utkin, J. C. Ranasinghesagara, L. Pan, Y. Godwal, R. J. Zemp, and R. Fedosejevs, “Optical Resolution Photoacoustic Microscopy Using Novel High-Repetition-Rate Passively Q-switched Microchip and Fiber Lasers”, *J. Biomed. Opt.* 15, 056017 (2010).
- [16] Y. Wang, K. Maslov, Y. Zhang, S. Hu, L. Yang, Y. Xia, J. Liu, and L. H., V. Wang, “Fiber-laser-based photoacoustic microscopy and melanoma cell detection”, *J. Biomed. Opt.* 16, 011014 (2011).
- [17] B. Rao, L. Li, K. Maslov, and L. H. Wang, “Hybrid-scanning optical-resolution photoacoustic microscopy for *in vivo* vasculature imaging”, *Opt. Lett.* vol.35, no. 10, 1521- 1523 (2010).
- [18] J. C. Ranasinghesagara, Y. Jian, X. H. Chen, K. Mathewson, and R. J. Zemp, “Photoacoustic technique for assessing optical scattering properties of turbid media”, *J. Biomed. Opt.* 14, 040504 (2009).
- [19] A.F. Frangi, W.J. Niessen, P.D. Nederkoorn, J. Bakker, W.P.Th.M. Mali, and M.A. Viergever, “Quantitative analysis of vessel morphology from 3D MR angiograms: *in vitro* and *in vivo* results”, *Magn. Reson. Med.* 45(2) 311 – 322 (2001).
- [20] S. Hu, K. Maslov, and L.V. Wang, “Second-generation optical-resolution photoacoustic microscopy with improved sensitivity and speed”, *Opt. Lett.* vol. 36, no. 7, 1134-1136 (2011).
- [21] Laser Institute of America, American National Standard for Safe Use of Lasers ANSI Z136.1-2007 (American National Standards Institute, Inc., 2007).
- [22] J. B. Pawley, *Handbook of Biological Confocal Microscopy*, 3rd ed. Springer Science + Business Media, LLC, New York (2006).
- [23] Y. N. Billeh, M. Liu, and T. Buma, “Spectroscopic photoacoustic microscopy using a photonic crystal fiber supercontinuum source”, *Opt. Express* 18, 18519-18524 (2010).
- [24] P. Hajireza, W. Shi, P. Shao, S. Kerr, and R.J. Zemp, “Optical-resolution photoacoustic micro-endoscopy using image-guide fibers and fiber laser technology”, *Proc. SPIE* 78990P (2011)

5 *In vivo* dynamic process imaging using real-time optical-resolution photoacoustic microscopy

5.1 Introduction

Optical-resolution photoacoustic microscopy (OR-PAM) is an emerging imaging technology with high lateral resolution due to tightly focused micron-scale laser spot size, and high contrast in tissue based on optical absorption. Maslov et al. [1], first demonstrated *in vivo* imaging of the microvasculature including single capillaries in mice using OR-PAM with a lateral resolution of 5 μm at imaging depths > 0.7 mm. Later, more studies on using novel OR-PAM techniques for structural [2] and functional [2-6] imaging were reported. OR-PAM has demonstrated its potential applications for neuro-functional imaging, oxygen saturation imaging [3][4], blood velocity imaging[5], transcranial imaging of whole brain murine cortical capillary networks [6]. In addition, OR-PAM was reported to realize *in vivo* imaging of amyloid plaques in a transgenic mouse model of Alzheimer's disease [7], as well as longitudinal monitoring of angiogenesis in a transgenic mouse model [8][9], demonstrating the potential to monitor the efficacy of anti-angiogenic therapies.

In order to extend the applications of OR-PAM to clinical applications, ease of use and real-time operation will be key factors to be implemented. Both laser pulse repetition rate (PRR) and scanning speed are important factors affecting the imaging speed. Recently, Hu et al. [10] developed a second-generation OR-PAM system based on mechanical translation of an imaging head. They reported a 70 minute image acquisition time for a $7.8 \text{ mm} \times 10 \text{ mm}$ FOV with a pixel size of $2.5 \mu\text{m} \times 2.5 \mu\text{m}$. Translating the imaging head instead of the living object accelerated the scanning speed by a factor of 5[10]. However, despite high image quality, imaging speed was far below real-time rates. Xie et al. [11] reported a laser-scanning OR-PAM with only laser light being raster scanned by an x-y galvanometer mirror system while keeping the ultrasonic transducer stationary. The system enabled fast scanning speed but with imaging speed limited mainly by their kHz PRR laser. In 2010, our group demonstrated laser-scanning OR-PAM imaging using passively Q-switched microchip lasers with PRR exceeding 10 kHz and fiber lasers with 100 kHz PRR [12]. Later, a 50 kHz fiber-laser operating at 1064nm for OR-PAM is reported by Wang et al. [13]. In 2011, our group demonstrated an OR-PAM system using a fiber laser source with high repetition

rate of up to 600 kHz capable of C-scan imaging at 4 frames per second [14]. However, the system was limited to acquisition of only 2-3 volumetric datasets due to memory limitations and sustained real-time imaging was not possible. Rao et al. [15] reported a high-speed OR-PAM system in an inverted microscope configuration with Au nanoparticle-assisted sub-diffraction-limit resolution. With a 100 kHz pulsed laser, a stationary ultrasonic transducer and a two dimensional (2-D) - Galvo system scanning the collimated laser beam through the pupil of objective lens, their system demonstrated its ability to achieve *in vivo* imaging of microcirculation in mouse skin at 18 three-dimensional volumes per second with repeated 2-D raster scans of 100 by 50 points for 100 μm x 50 μm image size with 0.23 micron point size and 256 A-line measurements at each points. However, their setup worked only in transmission mode, which limits its applications for thick soft tissue. Also, imaging microcirculation in their system required the assistance of nanoparticle agents. In [16] a second generation OR-PAM system was used to acquire ECG-gated measurements of blood pulse-waves in small vessels. This novel approach offered outstanding image quality and provided for the first time, estimates of pulse-wave velocities using photoacoustic imaging, however, real-time C-scan visualization was not possible. Yao et al [17] demonstrated an immersible MEMS-mirror scanning system capable of high volumetric frame rates, and imaging of carbon particles and red blood cells, however, they did not correlate microvascular hemodynamics with cardiac pulsations, which could be important in pulse-wave velocity studies. In our previous studies [14], we were not able to image dynamic processes due to previous data acquisition limitations of our system. In this paper, we demonstrate an improved fast C-scan OR-PAM system which enables both sustained imaging and real-time imaging. We report *in vivo* label-free reflection-mode real-time OR-PAM imaging of micro-hemodynamics correlated with cardiac pulsations and anticipate this system can play an important role in future functional imaging studies of neuronal-hemodynamic coupling.

5.2 Methods

Fig.5.1 shows the schematic of the real-time OR-PAM system. Laser pulses with high repetition rate ranging from 20 kHz - 600 kHz are generated by a diode-pumped pulsed Ytterbium-doped fiber laser (GLP-10, IPG Photonics Corporation.). Via a built-in compact laser head, the 1064-nm fundamental wavelength is frequency-doubled to 532-nm and is then collimated for free space output. Laser amplifier pump power can be adjusted to provide nanosecond laser pulses with

programmable pulse energy up to 20 μJ . A small amount of light is reflected by a glass slide onto a high speed custom photodiode to generate trigger signals for a data acquisition card (PCI 6221, National Instruments Corporation). A 2D galvanometer scanning mirror system (6230H, Cambridge Technology Inc.) deflected the incident laser beam onto an 18-mm-focal-length objective lens positioned ~ 3.6 cm below. With 2D XY mirrors driven by analog sinusoidal signals from a dual channel function generator (AFG3022B Tektronix Inc.), the raster scanning of laser beam on the objective lens focal plane was realized. The scanning angles are determined by the amplitudes of the sinusoidal signals outputs from the function generator. Together with the focal length of objective lens, the maximum scanning angles on both axes determine the image FOV. Also, the maximum scanning angles limit the maximum scanning speed that the mirrors can reach up to several kHz for small angles. The laser beam scanned onto the objective lens is focused through our unique light-delivery probe adapted from our previous work [12][14][18]. As shown in Fig.5.1, a downfacing 10-mm silica prism together with optical index-matching fluid (Catalog # 19569, Cargille Labs, Cedar, Grove, New Jersey) and a thin transparent plastic membrane to hold the index-fluid in place enabled top-down laser beam be directed to the object without optical refractive path deviation. The object is positioned underneath the membrane at the focal plane of both the objective lens and a 3.5 MHz focused ultrasound transducer (19-mm focus, 6-mm active element, $f\#=3.17$, CD International Inc.). The generated upwards photoacoustic signal was reflected by the optical prism and then received by the ultrasound transducer. According to our previous work [18], acoustic attenuation in the index matching fluid is measured to be only slightly higher than that in water. Also, for acoustic signal within the angular acceptance of the transducer, the acoustic reflectivity on the prism and index matching fluid interface is almost 100% [18].

Two data acquisition methods were developed on the system configured in Fig.5.1: long acquisition mode and multiple-record acquisition mode. In long acquisition mode, for each frame, the system collects photoacoustic signals from large number of laser shots in one long acquisition and then block-transfers data to the PC random-access memory (RAM). With this method, data acquisition time is based on both the data collection time and data block-transferring time. The fast ($\sim 200\text{MB}/\text{sec}$) data block-transfer rate capabilities of the high speed digitizer (CS8289, Gage Cobra, Gage Applied Systems, Inc.) enable sustained data acquisition. High frame rate is achievable for small FOV where data block-transfer time is short due to the small amount of data

need to be transferred. In multiple-record acquisition mode, the system collects photoacoustic signals for each laser shot in one acquisition and transfers data when all data collection is done. With this method, high frame rate is achievable since there is no data transfer time between acquisition records. However, transfer of all data collection at the end requires substantially longer time than transfer of a large single acquisition data in long acquisition mode. Therefore, sustained real-time acquisition is difficult to realize in this method. Nevertheless, it can be used to realize real-time imaging for a small FOV with limited number of frame acquisitions limited by memory buffer size of 128 Mbytes. Its real-time nature can be used for imaging of microcirculation hemodynamics.

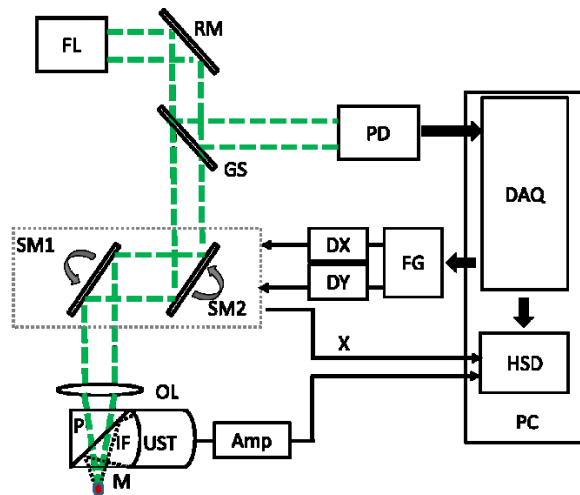


Fig 5.1. Experiment setup of the real-time OR-PAM system (FL: fiber laser; RM: high reflectivity mirror; GS: glass slide; PD: photodiode; SM1, SM2: scanning mirror; DX, DY: galvanometer scanning mirror driver; FG: 2-channel function generator; DAQ: data acquisition card; OL: 18-mm objective lens; P: prism; IF: index-matching fluid; M: membrane; UST: ultrasonic transducer; Amp: amplifier; HSD: high speed digitizer).

5.3 Results

The OR-PAM system is utilized for imaging *in vivo* dynamic processes. Seven-week old SCID Hairless Outbred (SHOTM, Charles River, MA, USA) mice were used for our *in vivo* imaging studies. The animals were anesthetized using a breathing anesthesia system (E-Z Anesthesia, Euthanex Corp.) during image acquisition. All experimental animal procedures were conducted in conformity with the laboratory animal protocol approved by the Animal Use and Care Committee of the University of Alberta.

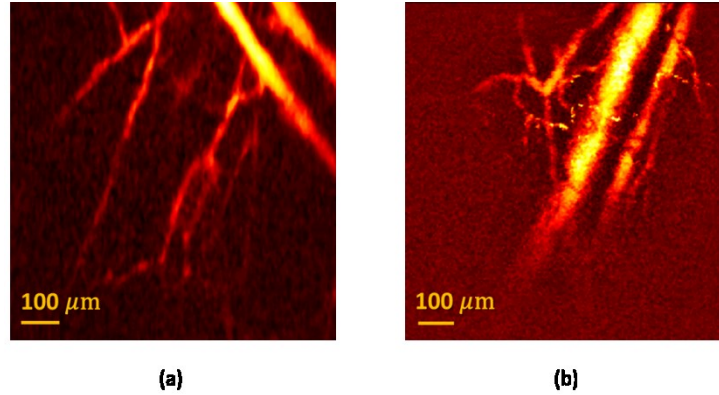


Fig.5.2. (a) An *in vivo* image of micro-vasculatures obtained from a hairless SCID mouse ear to demonstrate the imaging capability of our imaging system; (b) A snapshot from the *in vivo* movie composed of 41 frame 1mm× 1mm images of microvasculature in a SCID hairless mouse ear when the mouse was in a vertical movement; video 1 displays at 2fps while the actual system frame rate is about 0.5 fps; some small capillaries come out and disappear during the vertical translation.

Animal imaging experiments demonstrated the dynamic imaging capability of our system. During the experiments, the diode-pumped pulsed Ytterbium-doped fiber laser generated 320 kHz, ~1ns, 532-nm laser pulses with ~0.1 μJ (measured after the objective lens). The raster scanning frequencies on two axes were set as 1 Hz on the Y axis and 400 Hz on the X axis, and both maximum optical scanning angles were ~1.6° which corresponds to 1 mm × 1 mm FOV. A high-precision motorized translation stage (not shown in Fig.5.1) was used to translate the mice each time after one frame scan was finished. The position of the stage was sensed by encoders and recorded. The long acquisition mode technique was used for sustained imaging of translations. For the repeated 2D scans of 400 by 400 points with 156 A-line measures at each point, the photoacoustic data collection time was 0.5 s. Block-data transfer time was a slightly over 0.5 s, resulting in a frame rate of 0.5 fps which means 1D A-scan rate of 80,000 Hz. Fig.5.2(a) shows a maximum-amplitude-projection (MAP) snapshot of microvasculature in a SCID mouse ear to demonstrate the imaging capability of our system. It clearly depicts the vessels including small capillaries. This is consistent with previous resolution studies using our OR-PAM system with ~6-μm resolution [12][14]. Fig.5.2(b) shows a snap shot taken from a movie of microvasculature MAP images in a SCID mouse ear as well but with mouse under 6 micron per step vertical translation for focusing. Vessels including capillaries are visualized. The corresponding movie is displayed at 2 fps in video 1. It includes a total of 41-frame 1mm× 1mm images acquired at 0.5 fps. Some small capillaries show up and disappear in the video as the mouse is translated.

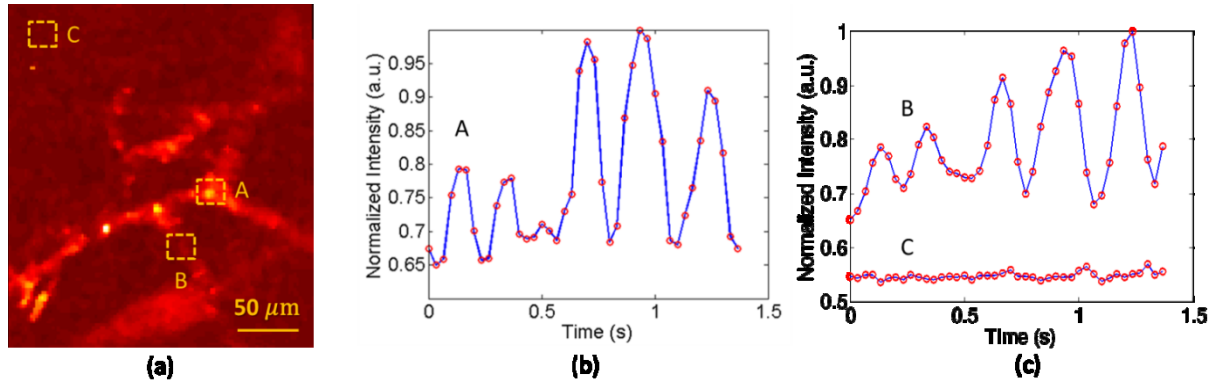


Fig.5.3. (a) A snapshot from the *in vivo* movie composed of 42 frame $250\ \mu\text{m} \times 250\ \mu\text{m}$ images of microvasculature in a SCID hairless mouse ear acquired at 30 fps; video 2 displays at 15 fps, while microvasculature motions and blood intensity changes are clear to see. (b) Mean photoacoustic signal amplitude inside the dash box A indicated area in (a) versus time. (c) Mean photoacoustic signal amplitude inside the dash box B and C indicated area in (a) respectively versus time.

In our studies on imaging dynamic processes of micro-hemodynamics, the diode-pumped pulsed Ytterbium-doped fiber laser generated 300-kHz, ~ 1 -ns, 532-nm laser pulses with $\sim 0.1\ \mu\text{J}$. Raster scanning frequencies of the fast-scanning mirrors were set as 15 Hz for the Y axis and 1.5 kHz for the X axis. Therefore, the data collection rate can reach 30 fps (2 times the slow axis scan rate). Also, due to the limitation of the scanning galvanometer mirror system, the maximum optical scanning angles of both mirrors are set as $\sim 0.4^\circ$. The resulting imaging area was $250\ \mu\text{m} \times 250\ \mu\text{m}$. The mice were kept stationary during the experiment. Multi-record acquisition mode was adapted as the data acquisition method to reach a frame-rate of 30 fps over a limited number of frame acquisitions with 156 A-line measures at each point for 100 by 100 repeated 2D scans. The corresponding 1D A-scan rate was 300,000 Hz. Fig.5.3(a) shows a single frame from a movie representing MAP images of microvasculature in a SCID mouse ear. The corresponding movie (video 2) is composed of 42-frame $250\ \mu\text{m} \times 250\ \mu\text{m}$ images taken at a frame rate of 30 fps. A periodic variation in photoacoustic intensity was observed, which we hypothesize is the flow of blood cells through the vessels due to cardiac cycle-induced pulse waves propagating through arterioles. We examined the photoacoustic signal amplitude over time within the dashed box region A indicated in Fig.5.3(a) by averaging the intensity as seen in Fig.5.3(b). The intensity variation is about 35% with ~ 5 peaks clearly depicted in ~ 1.4 s, which is consistent with the heart rate of an anaesthetized mouse measured independently by a pulse-oximeter. For comparison, we examined the photoacoustic signal amplitude over time within the dashed box region B and C indicated in Fig.5.3(a) respectively, while region C did not include visible blood vessels. The

intensity variation for B is similar to that of A, while the intensity variation for C is within 5%, much less compared with studies on region A and B. In addition, the pulse energy instability of the diode-pumped pulsed Ytterbium-doped fiber laser used here is within 1%.

5.4 Discussion

In vivo images of microvasculature in SCID mouse ears under translations, with an average pixel separation of $2.5\ \mu\text{m}$ within a FOV of $1\ \text{mm} \times 1\ \text{mm}$, were obtained at a frame-rate of 0.5 fps. Higher frame rate with sustained imaging is achievable for smaller FOV (~ 7 fps for a FOV of $250 \times 250\ \mu\text{m}$). The step size for the vertical translation in Fig.5.2 is $6\ \mu\text{m}$. So for 41 frames, it moved $\sim 240\ \mu\text{m}$ in total. Some small vessels including capillaries are seen to come into and out of focus with vertical translation. However, this is less evident for larger vessels. One explanation of this is that for targets larger than the spot size, with OR-PAM (which, like conventional microscopy uses one-way focusing) the photoacoustic axial depth of field is effectively much larger than the optical depth of field of the focused beam (estimated as $\sim 35\ \mu\text{m}$) [19]. This, coupled with poor axial resolution ($\sim 500\ \mu\text{m}$) leads to lack of clear axial focusing/defocusing for large targets. The sustained high resolution fast imaging demonstrated the capability of our system to be used for real-time focusing and positioning. Near real-time positioning will permit panning over large areas with mm FOV windows and then locating regions of interest for further studies.

Video 2 is the label-free reflection-mode OR-PAM demonstration of imaging micro-hemodynamics. One observation, already noted, is the intensity variations which correlate with cardiac cycle. This may in part be explained by surges of blood periodically surging through arterioles due to cardiac-induced pulse-waves. Another observation is that some vascular branches seem to have negligible flow then seemingly random transient surges. These effects deserve additional study and could be due to microhemodynamic regulatory mechanisms. The effects seen can be discounted as artifacts, however, because laser pulse-to-pulse intensity variation is less than 1% and scanning of stationary phantom structures shows no motion. It is noteworthy to point out that optical coherence tomography can provide excellent structural images of microvasculature [20][21]. However, to date, these systems have not been able to provide video-rate imaging of comparable tissue volumes due to the necessity of requiring multiple A-scan lines to extract motion of scatterers. Intravital microscopy is a powerful technique which has been capable of studying

microhemodynamics [22]. However, this technique requires surgical exposure of thin transparent membranes and is not suitable for non-invasive reflection-mode imaging.

The unique capabilities of our system may prove important for imaging cortical hemodynamics in functional brain mapping studies. Real-time focusing and positioning should facilitate translation of the technique to clinical settings. While FOV is limited in our real-time scanning, mosaicing of small patches should provide larger-FOV images, as described by our recent work [23].

For 2D laser scanning OR-PAM systems using a focused transducer, the FOV is limited by the focal width of the ultrasonic transducer. Therefore, we used a low frequency (3.5 MHz) ultrasonic transducer to achieve a large FOV. The axial resolution of the 3.5 MHz ultrasonic transducer can be calculated as near 500 μm , sacrifice of axial resolution is tolerable for MAP images. A future design could match the receiver bandwidth to the bandwidth of the high-frequency photoacoustic signals to improve signal-noise-ratio (SNR) at the expense of FOV.

In our *in vivo* studies, given that the optical focus is $\sim 150 \mu\text{m}$ beneath the tissue surface, with an objective lense NA of 0.15, the surface spot size is $\sim 45 \mu\text{m}$ in diameter, and the calculated surface laser fluence is $\sim 5 \text{ mJ}/\text{cm}^2$, below the single pulse limit of $20 \text{ mJ}/\text{cm}^2$ set by the American National Standards Institute (ANSI) [24]. The spatial peak optical fluence at the focus in water is $\sim 500 \text{ mJ}/\text{cm}^2$, which is still less than the damage threshold observed in small animals [25]. In our work, light delivery is confined to a localized area and no tissue damage is visible after imaging.

In addition, for an average pixel separation of $2.5 \mu\text{m}$, there are on average $N=45\mu\text{m}/2.5\mu\text{m}\sim 18$ adjacent laser pulses overlapping on the skin surface. For 320 kHz laser PRR, the exposure time is $t\sim 56\mu\text{s}$, so the MPE for a pulse train is $MPE_{Train}=1.1C_A t^{0.25}=95\text{mJ}/\text{cm}^2$, where C_A is a wavelength-correction factor equal to unity for 400-700nm wavelengths. The average power limit set by ANSI is calculated as $MPE_{Average}=MPE_{Train}/N\sim 5\text{mJ}/\text{cm}^2$ which is our estimated fluence per pulse at the skin surface. This means that we are essentially at our theoretical upper limit for pulse-repetition rate, however, the repetition rate could be increased if pulse-energy can be lowered and SNR improved. In future studies, careful selection of focusing, repetition rate, and pulse

energy parameters must be considered to avoid exceeding ANSI limits. On the other hand, for some pre-clinical applications, exceeding these limits may be acceptable.

5.5 Conclusion

We have demonstrated an optical-resolution photoacoustic microscopy system capable of near real-time sustained imaging to aid focusing and positioning, and a real-time frame-limited mode capable of imaging micro-circulation pulsatile hemodynamics. This OR-PAM system enabled label-free reflection-mode imaging of micro-hemodynamics at real-time rates. The fast acquisition capabilities of the system may pave the way for clinical adaptation and pre-clinical studies such as functional brain imaging.

Bibliography

- [1] K. Maslov, H. F. Zhang, S. Hu, and L. H. V. Wang, "Optical-resolution photoacoustic microscopy for *in vivo* imaging of single capillaries," *Opt. Lett.* **33(9)**, 929-931 (2008).
- [2] S. Hu, K. Maslov, and L. V. Wang, "Noninvasive label-free imaging of microhemodynamics by optical-resolution photoacoustic microscopy," *Opt. Express* **17(9)**, 7688–7693 (2009).
- [3] S. Hu, K. Maslov, and L. V. Wang, "*In vivo* functional chronic imaging of a small animal model using optical-resolution photoacoustic microscopy," *Med. Phys.* **36(6)**, 2320–2323 (2009).
- [4] L. Song, K. Maslov, and L. V. Wang, "Multifocal optical-resolution photoacoustic microscopy *in vivo*," *Opt. Lett.* **36(7)**, 1236-1237 (2011).
- [5] J. Yao, K. Maslov, Y. Shi, L. Taber, and L. V. Wang, "*In vivo* photoacoustic imaging of transverse blood flow using Doppler broadening of bandwidth," *Opt. Lett.* **35(9)**, 1419–1421 (2010).
- [6] S. Hu, K. Maslov, V. Tsytsarev, and L. V. Wang, "Functional transcranial brain imaging by optical-resolution photoacoustic microscopy," *J. Biomed. Opt.* **14(4)**, 040503 (2009).
- [7] S. Hu, P. Yan, K. Maslov, J. M. Lee, and L. H. V. Wang, "Intravital imaging of amyloid plaques in a transgenic mouse model using optical-resolution photoacoustic microscopy," *Opt. Lett.* **34(24)**, 3899-3901 (2009)
- [8] S. Oladipupo, S. Hu, A. C. Santeford, J. Yao, J. Kovalski, R. V. Shohet, K. Maslov, L. V. Wang, and J. M. Arbeit, "Conditional HIF-1 induction produces multistage neovascularization with stage-specific sensitivity to VEGFR inhibitors and myeloid cell independence, " *Blood* **117(15)**, 4142-4153 (2011).
- [9] S. Oladipupo, S. Hu, J. Kovalski, J. Yao, A. C. Santeford, R. Sohn, R. V. Shohet, K. Maslov, L. V. Wang, and J. M. Arbeit, "VEGF is essential for hypoxia-inducible factor mediated neovascularization but dispensable for endothelial sprouting, " *P NAS* **108(32)**, 13264-13269 (2011).
- [10] S. Hu, K. Maslov, and L. V. Wang, "Second-generation optical-resolution photoacoustic microscopy with improved sensitivity and speed," *Opt. Lett.* **36(7)**, 1134-1136 (2011).
- [11] Z. X. Xie, S. L. Jiao, H. F. Zhang, and C. A. Puliafito, "Laser-scanning optical-resolution photoacoustic microscopy," *Opt. Lett.* **34(12)**, 1771-1773 (2009).

- [12] W. Shi, S. Kerr, I. Utkin, J. C. Ranasinghesagara, L. Pan, Y. Godwal, R. J. Zemp, and R. Fedosejevs, "Optical resolution photoacoustic microscopy using novel high-repetition-rate passively Q-switched microchip and fiber lasers," *J. Biomed. Opt.* **15**, 056017 (2010).
- [13] Y. Wang, K. Maslov, Y. Zhang, S. Hu, L. Yang, Y. Xia, J. Liu, and L. H. V. Wang, "Fiber-laser-based photoacoustic microscopy and melanoma cell detection," *J. Biomed. Opt.* **16(1)**, 011014 (2011).
- [14] W. Shi, P. Hajireza, P. Shao, A. Forbrich, and R. J. Zemp, "*In vivo* near-realtime volumetric optical-resolution photoacoustic microscopy using a high-repetition-rate nanosecond fiber-laser," *Opt. Express* **19(18)**, 17143-17150 (2011).
- [15] B. Rao, K. Maslov, A. Danielli, R. Chen, K. K. Shung, Q. Zhou, and L. H. V. Wang, "Real-time four-dimensional optical-resolution photoacoustic microscopy with Au nanoparticle-assisted subdiffraction-limit resolution," *Opt. Lett.* **36(7)**, 1137-1139 (2011).
- [16] C. Yeh, S. Hu, K. Maslov and L. V. Wang, "Photoacoustic microscopy of blood pulse wave," *J. Biomed. Opt.* **17(7)**, 070504 (2012)
- [17] J. Yao, C.-H. Huang, L. Wang, J.-M. Yang, L. Gao, K. I. Maslov, J. Zou and L. V. Wang, "Wide-field fast-scanning photoacoustic microscopy based on a water-immersible MEMS scanning mirror," *J. Biomed. Opt.* **17(8)**, 080505 (2012)
- [18] J. C. Ranasinghesagara, Y. Jian, X. H. Chen, K. Mathewson, and R. J. Zemp, "Photoacoustic technique for assessing optical scattering properties of turbid media," *J. Biomed. Opt.* **14(4)**, 040504 (2009).
- [19] L. V. Wang and H. Wu, *Biomedical Optics: Principles and Imaging*, John Wiley & Sons, Inc., Hoboken, New Jersey (2007).
- [20] A. Mariampillai, M.K.K. L. M. Jarvi, B.A. Standish, K. Lee, B.C. Wilson, A. Vitkin, and V.X.D. Yang, "Optimized speckle variance OCT imaging of microvasculature," *Opt. Lett.* **35(8)**, 1257-1259 (2010).
- [21] G. Liu, W. Jia, V. Sun, B. Choi, and Z. Chen, "High-resolution imaging of microvasculature in human skin in-vivo with optical coherence tomography," *Opt. Express* **20(7)**, 7694-7705 (2012).
- [22] A. M. Iga, S. Sarkar, K. M. Sales, M. C. Winslet, and A. M. Seifalian, "Quantitating therapeutic disruption of tumor blood flow with intravital video microscopy," *Cancer Res.* **66(24)**, 11517-11519 (2006).

- [23] P. Shao, W. Shi, R. K. Chee, and R. J. Zemp, "Mosaicing acquisition and processing for optical resolution photoacoustic microscopy," *J. Biomed. Opt.* **17(8)**, 080503 (2012).
- [24] Laser Institute of America, American National Standard for Safe Use of Lasers ANSI Z136.1-2007 (American National Standards Institute, Inc. 2007).
- [25] V. P. Zharov, E. I. Galanzha, E. V. Shashkov, N. G. Khlebtsov, and V. V. Tuchin, "*In vivo* photoacoustic flow cytometry for monitoring of circulating single cancer cells and contrast agents," *Opt. Lett.* **31(24)**, 3623-3625 (2006).

6 Investigation of photoacoustic signal strength as a function of scan-speed and laser-repetition-rate

6.1 Introduction

Photoacoustic effect was first reported by Alexander Graham Bell in 1880[1]. When short laser pulses are fired on a sample, optically-absorbing structures convert the energy into heat causing thermo-elastic expansion and inducing acoustic pressure waves detectable with ultrasound transducers. Photoacoustic signal depends on the absorption of light and the subsequent emission of an acoustic wave. The pressure rise of the generated acoustic wave is proportional to the Greneisen parameter, which is temperature dependent. Based on temperature dependence of photoacoustic signal, some studies have been conducted on photoacoustic detection based temperature measurements and photothermal cancer therapy, especially with enhancement of nanoparticles [2-4].

By tightly optical focusing of laser beam onto target, photoacoustic imaging pushes the limits of the lateral resolution to micron-scale, which is determined by the size of a focused light spot (limited by diffraction-limited focal spot size) rather than the width of the ultrasonic focal zone. This novel imaging technology is referred to as optical resolution photoacoustic microscopy (OR-PAM). The ability to resolve capillaries enables OR-PAM to detect earlier stages of cancer than traditional photoacoustic imaging [5][6]. For clinical adaptation and pre-clinical studies, OR-PAM is developing into a real-time technique, where laser with high pulse repetition rate and fast optical scanning of the focused laser spot are required[7-9]. High laser pulse repetition rate may cause overlapping of adjacent laser pulses on targets, where subsequent laser pulses may generate higher photoacoustic signals due to the temperature rise caused by previous laser pulse absorption. Therefore, for OR-PAM using high laser pulse repetition rate, besides local optical absorption and laser fluence, photoacoustic signal also depends on scanning speed and laser-repetition-rate which affect the overlapping of adjacent laser pulses on targets. The purpose of this investigation is to study photoacoustic signal strength as a function of scan-speed and laser-repetition-rates.

6.2 Theory

6.2.1 Thermal Confinements and Stress Confinements

Upon irradiated by a short pulsed laser beam, the tissue produces thermal and acoustic impulse responses. The excited photoacoustic signal is locally determined by the electromagnetic absorption and scattering properties, the thermal properties, and the elastic properties of the sample[10].

There are two crucial conditions which must be met as to efficiently generate photoacoustic signals: thermal confinements and stress confinements[11]. Thermal confinement: the pulse width (τ_p) should be shorter than heat dissipation time scale (τ_{th}), i.e. heat diffusion is negligible during the excitation pulse. Stress confinement: the pulse width (τ_p) should be shorter than the time for the stress to transit the heated region (τ_s), i.e. high thermoelastic pressure in the sample can build up rapidly[11].

6.2.2 Gruneisen Parameter

When the laser excitation is in both the thermal and stress confinements, the pressure rise caused by optical absorption via thermal expansion can be expressed as [11][12]:

$$p_0 = \frac{\beta v_s^2}{C_p} \mu_a F = \Gamma \mu_a F \quad (1)$$

where β denotes the thermal coefficient of volume expansion coefficient in K^{-1} , v_s is the speed of sound in m/s, C_p denotes the specific heat capacity at constant pressure in J/ (kg K), μ_a is the optical absorption coefficient in cm^{-1} , F is the optical fluence in J/cm^2 . $\Gamma = \frac{\beta v_s^2}{C_p}$, is the Gruneisen parameter. Thus, the strength of photoacoustic signals is proportional to optical absorption coefficient, optical fluence and Gruneisen parameter which is temperature dependent.

For water and diluted aqueous solutions, Gruneisen parameter can be estimated by the following empirical formula:

$$\Gamma_w(T_0) = 0.0043 + 0.0053T_0 \quad (2)$$

where T_0 is the temperature in degree Celsius.

6.2.3 Temperature Rise

The temperature rise caused by optical can be expressed as [11][12]:

$$\Delta T = \frac{A_e}{\rho C_v}, \quad (3)$$

where $A_e = \mu_a F$, denotes the specific optical absorption (J/cm^3), ρ denotes the mass density ($\sim 1\text{g}/\text{cm}^3$ for water) and C_v denotes the specific heat capacities at constant volume ($\sim 4\text{J}/(\text{g K})$ for water).

6.3 Methods

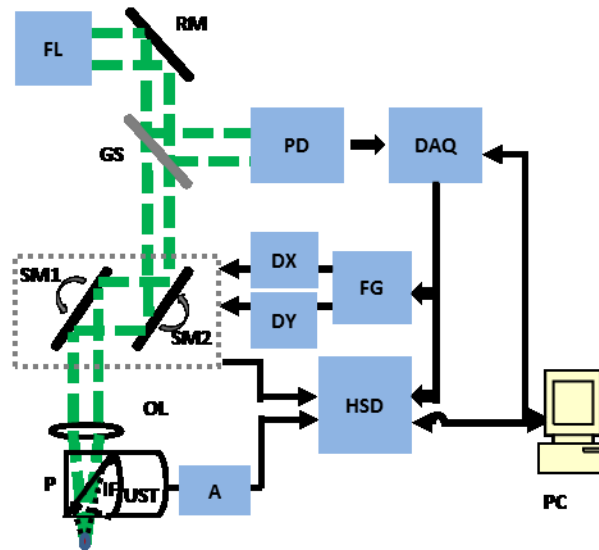


Fig.6.1. Experiment setup (FL: fiber laser; RM: high reflectivity mirror; GS: glass slide; PD: photodiode; SM1, SM2: scanning mirror; DX, DY: galvanometer scanning mirror driver; FG: 2-channel function generator; DAQ: data acquisition card; OL: 18-mm objective lens; P: prism; IF: index-matching fluid; UST: ultrasonic transducer; A: amplifier; HSD: high speed digitizer).

The system diagram is shown in Fig.6.1. Laser pulses are generated by a diode-pumped 532-nm pulsed Ytterbium-doped fiber laser (GLP-10, IPG Photonics Corporation.) with laser-repetition-rate ranging from 20 to 600 kHz and ~ 1 ns pulse widths. A small amount of light was deflected onto a high speed custom photodiode for triggering and pulse-to-pulse energy normalization by a glass slide. A 2D galvanometer scanning mirror system (6230H, Cambridge Technology Inc.) is used to raster scan the laser beam onto an 18-mm-focal-length objective lens. XY mirrors are driven by analog sinusoidal signals from a two channel function generator (AFG3022B, Tektronix Inc.). The scanning speed of each mirror can reach up to several kHz depending on the scanning angles required. The field of view on the imaging plane (focal plane of objective lens) is

determined by the maximum scanning angle corresponding to the amplitude of the function generator output. Laser beam is focused by the objective lens (~3.6 cm below the centers of the scanning mirrors) through a unique light-delivery probe adapted from our previous work [13]. The generated photoacoustic signals were detected by a 3.5-MHz ultrasound transducer, amplified by an ultrasound pulser-receiver (5900PR, Olympus NDT Inc) and finally acquired by a 12-bit eight channel rate PCI data acquisition card (CS8289, Gage Cobra, Gage Applied Systems, Inc.) with sample rate up to 125 MSamples/s. The photoacoustic signal acquisition was triggered by the photodiode signals along with the feedback positions of the scanning mirrors. MATLAB programs (Mathworks, Inc) were used for further data processing and analysis.

6.4 Experiments and results

In our experiments, the diode-pumped pulsed Ytterbium-doped fiber laser generated ~1ns, 532-nm laser pulses with 100nJ pulse energy (measured after the objective lens).

Condition	Laser repetition rate (kHz)	Laser pulse energy (nJ)	X-axis Scanning speed (Hz)	Y-axis Scanning speed (Hz)	Field of View ($\mu\text{m} \times \mu\text{m}$)	Average Pixel Interval (μm)	Focal Spot Size (μm)
1	32	100	40	800	250×250	12.5	~ 6
2	320	100	1	400	1000×1000	2.5	~ 6

Tab 6.1. Two sets of experimental parameters in our experiments, referred as condition 1 and condition2, corresponding to non-overlapped and overlapped mode respectively.

To realize non-overlapping of laser pulses on target during imaging, the laser pulse repetition rate was set to 32 kHz. The fast scanning speed was set as 800 Hz, while slow scanning speed was 40 Hz, referred as condition 1 shown in table 6.1. The raster scanning amplitudes on both axes were set as 100 mV, and hence maximum optical scanning angles were $\sim 0.4^\circ$ which corresponds to $250 \mu\text{m} \times 250 \mu\text{m}$ FOV. The pixel numbers per imaging was 20×20 . Therefore, the average interval between pixels was $12.5 \mu\text{m}$, about twice large as the focused optical spot size ($\sim 6 \mu\text{m}$) and hence can be considered as no overlapping of laser pulses happened. As shown in table 6.2, the average photoacoustic signal from black tape, human hair and rat blood were 333mV, 347mv, 361mV respectively for condition 1.

To realize overlapping of laser pulses, the laser-repetition-rate was set to 320 kHz. The fast scanning speed was set as 400 Hz, while slow scanning speed was 1 Hz, referred as condition 2

shown in table 6.1. The pixel numbers per imaging was 400×400 . The raster scanning amplitudes on both axes were set as 400 mV, and hence maximum optical scanning angles were $\sim 1.6^\circ$ which corresponds to $1000 \mu\text{m} \times 1000 \mu\text{m}$ FOV. Therefore, the average interval between pixels was 2.5 μm , less than half of the focused optical spot size and hence the space overlapping of laser pulses occurred. Since the $\sim 3\mu\text{s}$ pulse time interval (for 320 kHz pulse repetition rate) is much less than thermal relaxation time of targets used in our experiments, the temperature effects on photoacoustic signals by Gruneisen parameter exist between consecutive overlapping laser pulses. As shown in table 6.2, the average photoacoustic signal from black tape, human hair and rat blood were 484mV, 432mv, 563mV respectively for condition 2.

Sample \ Condition	Condition	Photoacoustic Signal (mV)	Photoacoustic Signal Change from Condition 1 to Condition 2
Black Tape	1	333	↑ ~45%
	2	484	
Human Hair	1	347	↑ ~24%
	2	432	
Rat Blood	1	361	↑ ~56%
	2	563	

Tab 6.2. Average photoacoustic signals from black tape, human hair and rat blood, under condition 1 and condition 2 respectively.

6.5 Discussion and conclusion

Photoacoustic signals in condition 2 (overlapping mode) showed more than 50% increase compared to that in non-overlapping mode in our phantom studies with rat blood, and the increase was more than 40% and more than 20% for our studies with black tape and hair respectively.

In our experiments, for 100-nJ laser pulse energy and focal spot size of $\sim 6 \mu\text{m}$, optical fluence F on targets was $\sim 350\text{mJ}/\text{cm}^2$. Take rat blood for example, assuming $\mu_a = 180 \text{ cm}^{-1}$, the specific optical absorption $A_e = \mu_a F$, $\sim 60\text{J}/\text{cm}^3$. From formula (3), we can calculate the resulting temperature rise ΔT was $\sim 15^\circ\text{C}$. Thus, by using formula (2), the Gruneisen parameter increase due to 15°C temperature increase is $\Delta\Gamma/\Gamma = [\Gamma_w(40^\circ\text{C}) - \Gamma_w(25^\circ\text{C})]/\Gamma_w(25^\circ\text{C})$, $\sim 60\%$. Also, from formula (1), we know that pressure rise change $\Delta p_0/p_0 \propto \Delta\Gamma/\Gamma$. Hence the calculated photoacoustic signal increase can be calculated also as $\sim 60\%$. In our experiment result with rat

blood sample, in condition 1, where no overlapping of laser pulses happened and no temperature rising effects on photoacoustic signal caused by previous laser pulses, the photoacoustic signal was 361 mV. While in condition 2, where the temperature effects on photoacoustic signals by Gruneisen parameter exist between consecutive overlapping laser pulses, the photoacoustic signal was 563 mV, ~ 56% increase compared to that in condition 1. Therefore, our experiment result with rat blood is consistent with theoretical calculation of ~60% increase in photoacoustic signal.

Our experimental results shows that laser-repetition-rate and scanning speed in OR-PAM system may cause overlapping of adjacent laser pulses on targets within thermal relaxation time, and thus generate higher photoacoustic signals. Therefore, we demonstrated the dependence of photoacoustic signal strength on laser repetition rate and scanning speed in OR-PAM system, due to the temperature dependence of Gruneisen parameter. In the future, this may be used for improving imaging quality and may lead to a novel super-resolution technique.

Bibliography

- [1] A. G. Bell, “On the Production and Reproduction of Sound by Light”, *Am. J. Sci.* 20, 305 (1880)
- [2] I. V. Larina, K. V. Larin and R. O. Esenaliev, “Real-time optoacoustic monitoring of temperature in tissues”, *J. Phys. D: Appl. Phys.* 38, .2633–2639 (2005)
- [3] P. Li, C. C. Wang, D. Shieh, C. Wei, C. Liao, C. Poe, S. Jhan, A. Ding and Y. Wu, “*In vivo* Photoacoustic Molecular Imaging with Simultaneous Multiple Selective Targeting Using Antibody-Conjugated Gold Nanorods”, *Opt. Express* 23 (16),.18605-18615 (2008)
- [4] J. Shah, S. Park, S. Aglyamov, T. Larson, L. Ma, K. Sokolov, K. Johnston, S. Y. Emelianov, “Photoacoustic imaging and temperature measurement for photothermal cancer therapy”, *J Biomed Opt.* 13(3), 034024 (2008)
- [5] K. Maslov, H. F. Zhang, S. Hu and L. H., V., Wang, “Optical-resolution photoacoustic microscopy for *in vivo* imaging of single capillaries”, *Opt. Lett.* 33, 929-931 (2008)
- [6] Z. X. Xie, S. L. Jiao, H. F. Zhang and C. A. Puliafito, “Laser-scanning optical-resolution photoacoustic microscopy”, *Opt. Lett.* 34, 1771-1773 (2009)
- [7] W. Shi, S. Kerr, I. Utkin, J. C. Ranasinghesagara, L. Pan, Y. Godwal, R. J. Zemp, and R. Fedosejevs, “Optical resolution photoacoustic microscopy using novel high-repetition-rate passively Q-switched microchip and fiber lasers,” *J. Biomed. Opt.* 15, 056017 (2010)
- [8] W. Shi, P. Hajireza, P. Shao, A. Forbrich, and R. J. Zemp, “*In vivo* near-realtime volumetric optical-resolution photoacoustic microscopy using a high-repetition-rate nanosecond fiber-laser,” *Opt. Express* 19, 17143 (2011)
- [9] W. Shi, P. Shao, P. Hajireza, A. Forbrich, and R. J. Zemp, “*In vivo* dynamic process imaging using real-time optical-resolution photoacoustic microscopy ”, *J. Biomed. Opt.* 18, 026001 (2013)
- [10] C. K. N. Patel and A. C. Tam, “Pulsed photoacoustic spectroscopy of condensed matter,” *Rev. Mod. Phys.* 53, 517–550 (1981)
- [11] V. E. Gusev and A. A. Karabutov, “*Laser Optoacoustics*”, AIP, New York (1993)
- [12] A. A. Oraevsky and A. A. Karabutov, “Optoacoustic Tomography”, in *Biomedical Photonics Handbook*, ed. by T. Vo-Dinh, CRC Press, Boca Raton, Florida, Vol. PM125, Chapter 34 (2003)
- [13] J. C. Ranasinghesagara, Y. Jian, X. H. Chen, K. Mathewson and R. J Zemp, “Photoacoustic technique for assessing optical scattering properties of turbid media”, *Journal of Biomedical Optics* 14, 040504 (2009)

7 Detection of circulating tumor cells using targeted surface-enhanced-Raman-scattering nanoparticles and magnetic enrichment

7.1 Introduction

Metastasis, the spread of cancer cells from the primary tumor to distant sites in the body, is known to cause >90% of cancer-associated deaths [1]. Circulating tumor cells (CTCs) are a marker of cancer metastasis and hence a source of biomarkers for tumor research and diagnosis. Detecting CTCs helps in diagnosis at the early stages of metastasis and may have important prognostic and therapeutic implications [2]. However, directly identifying CTCs is difficult due to their low concentration in blood, which may be on the order of 1-10 CTC per mL compared to millions of white blood cells and nearly a billion of red blood cells per mL of blood [3]. Both capture sensitivity and specificity are critical for the detection of CTCs.

A variety of enrichment technologies have been developed to separate and identify CTCs [4-7]. Messenger RNA (mRNA) based strategies with PCR amplification do not allow collection of cells for further analysis and may miss CTCs that exhibit unexpected phenotypes. In immunomagnetic methods, iron or magnetic beads coated with monoclonal antibodies (mAb) specific to cell surface onco-antigens or cell specific cytokeratin (CK) and common leukocyte antigen (CD45) are used to capture and enrich CTCs [8]. Methods including flow cytometry are used for enumeration of CTCs in whole blood, which has high sensitivity and reproducibility, but rely on expensive specific equipment. Additionally, high specificity often requires multiple fluorescent labels to avoid false positives, yet spectral overlap of absorption and emission spectra from fluorescent labels can limit multiplexing and hence specificity. Additionally, background autofluorescence can significantly limit detection sensitivity in tissue. Microfluidic separation alone or in combination with immunomagnetic assays has also been used to capture and analyze CTCs [9-10]. Filter based physical methods have been developed to enable capture of CTCs based on size, keeping the CTCs while filtering out blood cells [11]. However, the above methods are not suitable for *in vivo* detection or enrichment.

In 2009, Galanzha et.al [12] reported rapid photoacoustic detection of magnetically captured CTCs *in vivo* using magnetic and optically-absorbing nanoparticles. In 2012, Wei et al. [13] demonstrated magnetomotive photoacoustic imaging of polystyrene beads using magnetic and photoacoustic contrast agents. Photoacoustic flow cytometry approaches have also been used to sort and detect CTCs [14]. However, these photoacoustic approaches have thus far demonstrated limited multiplexing capacity to improve specificity of detection.

Raman spectroscopy presents high multiplexing capabilities due to the multiple narrow linewidths of spectral peaks. Surface-enhanced Raman Scattering nanoparticles (SERS NPs) produce strong Raman-scattering optical signatures unique to each ‘flavor’ of SERS NPs, and offer a way of spectral fingerprinting that may provide extremely high specificity when targeting multiple cell biomarkers. In 2009, Zavaleta et.al, [15] demonstrated the ability to produce multiplexed *in vivo* images with 10 species of SERS NPs at picomolar (pM) sensitivities with ultralow background levels. In 2011, Wang et al., [16] reported using SERS NPs to detect CTCs in human peripheral blood. However, their method lacked an enrichment technique.

In 2010, Jun et al., demonstrated silica-encapsulated magnetic NPs (M-SERS dots) produce strong SERS signals and have magnetic properties which can be used for cancer-cell targeting and separation [17]. In 2014, Quaresma et al., reported star shaped gold-coated magnetic nanoparticles with unique properties demonstrated SERS detection of Astra Blue, and effective magnetic separation of a histidine-tagged maltose binding protein from a crude cell-extract [18]. However, neither of these studies examined the magnetic trapping of CTCs. Additionally, previously developed magnetic-SERS NPs could produce false positive signals during magnetic trapping when the intention is to detect only targeted CTCs.

To achieve detection of CTCs with high sensitivity and specificity, we propose a combination of magnetic trapping and multiplex detection of CTCs by using targeted magnetic NPs and SERS probes. We demonstrate a SERS imaging system with 1 pM sensitivity, 2.5 mm penetration depth, and high linearity between estimated SERS NPs concentration and actual SERS NPs concentration. Our magnetic trapping system is able to effectively trap cells at flow velocities ranging from 0.2 cm/s to 12 cm/s. Presently both SERS NPs and magnetic nanoparticles (MNPs) are targeted to folate receptor, overexpressed on many cancer cells but absent on most normal blood cells. We

show that only cells targeted with both SERS NPs and MNPs exhibit an increasing SERS signal due to magnetic accumulation of CTCs. Hence the SERS signal increase correlates with CTC detection. Free NPs or CTCs targeted with only SERS NPs or only MNPs do not exhibit this optical increase. In addition, discrete SERS signals were detected in the magnetic trapping zone from a mixture of flowing dual-nanoparticle labeled HeLa cells and Phosphate buffered saline (PBS) or rat blood indicative of single cell trapping events. This technology could be used for *in vitro* or *in vivo* detection of CTCs, and may prove important for cancer research, molecular diagnostics and personal medicine.

7.2 Materials and methods

7.2.1 Folate receptor targeting

Compared to low levels of folate receptors in most normal cells, many cancer cells (breast, lung, kidney, ovary, colon, brain, and myelogenous leukemia) significantly overexpress folate receptors to facilitate rapid cell division [19]. We conjugate nanoparticles with folate to target folate receptors of cancer cells.

7.2.2 MNPs

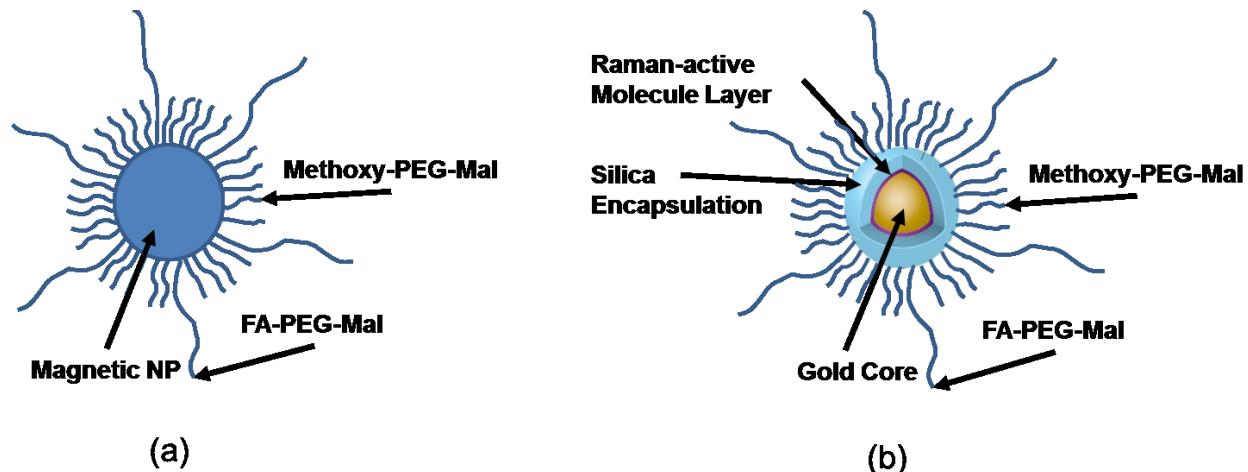


Fig.7.1 Diagrammatic representations of the conjugated (a) MNP and (b) SERS NP. PEG, polyethylene glycol; Mal, maleimide; FA, folate.

MNPs (screenMAG-Thiol, chemicell™ GmbH, Berlin, Germany) consisted of 500 nm-diameter magnetic fluorescent silica particles with nearly 1 million SH- groups per particle. To target folate receptors, thiolated MNPs (1.25 nM, $\sim 7.5 \times 10^{11}$ particles/mL) were added to a solution of folate-

PEG5k-maleimide (Nanocs Inc., New York, USA, PG2-FAML-5k, 0.8mM) and methoxy-PEG2k-maleimide (Sigma™ Aldrich, Oakville, Canada, 4mM) and mixed at room temperature by a rocker overnight. Excess folate-PEG-maleimide was separated from MNPs by three runs of centrifugation (14,000 RPM, 5 min), and resuspension in 2-(N-morpholino)ethanesulfonic acid (MES, Fisher Science) buffer. The diagrammatic representation of the conjugated MNP is shown in Fig.7.1 (a).

7.2.3 SERS NPs

SERS NPs (S440 & S420, Oxonica Materials Inc., Mountain View, CA, USA) are composed of a 60 nm-diameter Au core with a Raman active molecular monolayer adsorbed onto it. They are encapsulated with a 30 nm silica shell, with an overall diameter of 120 nm. Each type of SERS NP consists of a different Raman active molecular layer with its own unique Raman spectrum. To simplify, instead of nomenclature based on the Raman active molecular monolayer, a three-digit suffix (e.g., S440, S421) is used to name each type of SERS NP. Using a similar procedure as MNPs targeting, a solution of folate-PEG5k-maleimide (Nanocs Inc., PG2-FAML-5k, 0.8mM) and methoxy-PEG2k-maleimide (Sigma Aldrich, 4mM) was added to thiolated SERS NPs (1.3 nM, $\sim 8 \times 10^{11}$ particles/mL) and mixed at room temperature on a rocker overnight, followed by three runs of centrifugation (14,000 RPM, 5 min) to eliminate excess folate-PEG-maleimide and re-suspension in MES buffer. The diagrammatic representation of the conjugated SERS NP is shown in Fig.7.1(b).

7.2.4 Magnetic trapping system

To achieve efficient magnetic trapping, two rectangular neodymium rare earth magnets (25×5×5mm, Indigo™ Instruments, Waterloo, Canada) separated by a distance of 20mm were used to provide a 0.07 Tesla external magnetizing field in the tubing area. This was used to polarize the MNPs for subsequent efficient trapping. A 1” cone magnet (Cone-Cone0100N, SuperMagnetMan) pointed at the optical focus was used for generating a high magnetic field gradient for trapping. Cells were flowed inside a 1-mm inner-diameter Tygon™ tubing controlled by a syringe pump (NE-300, New Era Pump Systems, Inc., Farmingdale, USA).

7.2.5 Raman imaging system

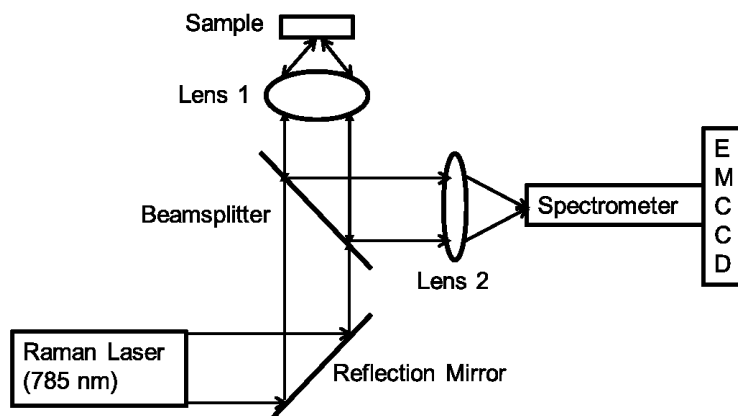


Fig.7.2 Schematic diagram of Raman imaging system.

Our Raman imaging setup (Fig.7.2) uses a 785 nm Raman laser (FB-785-350-FS-FS-1-1, RGBLase LLC, Fremont, CA, USA) as an excitation source. This laser provides up to 350 mW (while the power used in our experiment was 54 mW) and has a 20dB spectral linewidth of 0.4 nm and side lobe suppression ratio > 40dB. The narrow excitation linewidth is important since Raman peaks have linewidths of only a couple of nm or less. Raman spectra were captured using a custom Raman imaging spectrometer (RASPEEC -785-HR, P&P Optica Inc. Kitchener, ON, Canada). The imaging spectrometer is capable of measuring the Raman spectra from each point in a line. The input aperture is a slit of size 15 μ m x 26mm. Light from this slit is collimated and then passed through a gel grating then refocused onto a 2D camera sensor array. The imaging spectrometer presents a 21-degree bend to ensure collection of diffracted light in the desired spectral range. The gel-grating is a through-transmission grating with 900 l/mm offering a spectral range of 815 nm to 895 nm. The imaging spectrometer offers a spectral resolution of 10 cm^{-1} with an $f\#$ of 3.5. A 785 nm ultra-steep long-band-pass cut-off (OD 8) is used to as Raman filter. Spectra are detected using a liquid-cooled Electron-Multiplying (EM) CCD camera (DU971N-UV, Andor Technology, South Windsor, USA). This camera has dark current noise as low as 0.0002 e-/pix/sec at -100 $^{\circ}$ C and a quantum efficiency of \sim 50% at peak wavelengths, \sim 30% in the measurement wavelength range. The sensor head is a 1600 \times 400 pixel front-illuminated EMCCD array. The camera is mounted such that the spectra are recorded along the short-axis of the sensor. The camera can be rotated 90-degrees relative to the spectrometer if needed. Pixel elements are 16 \times 16 μ m. Presently we use only a few spatial channels (\sim 5 vertical pixels) of our imaging spectrometer system for

point illumination and collection. The electron-multiplying (EM) gain was set at 10, integration time was 3s, and sensor temperature was liquid-cooled to -100 °C. An aspheric lens (A240TM-B, Thorlabs, Newton , USA) with a 0.5 numerical aperture (NA) and 8mm focal length (shown as Lens 1 in Fig.7.2) was used for both illumination and light collection. Collimated backscattered light from the sample was redirected via a beam splitter (DMSP805L, Thorlabs) and focused into the input aperture of the imaging spectrometer via a 0.3 NA lens (AC127-019-B-ML, Thorlabs) with a magnification of ~2.4. Algorithms to correct for spherical aberrations on the camera sensor were provided by the spectrometer manufacturer. De-mixing was based on a classical linear least-squares method with an optional positivity constraint. In experiments, background noise and fluorescence signals generated from real tissue should be acquired before SERS detection and used as demixing factors to eliminate interference effects. Sensitivity was evaluated by detecting SERS signals from serial dilutions of SERS NPs solutions in PCR tubes.

7.3 Experiments and results

7.3.1 Sensitivity

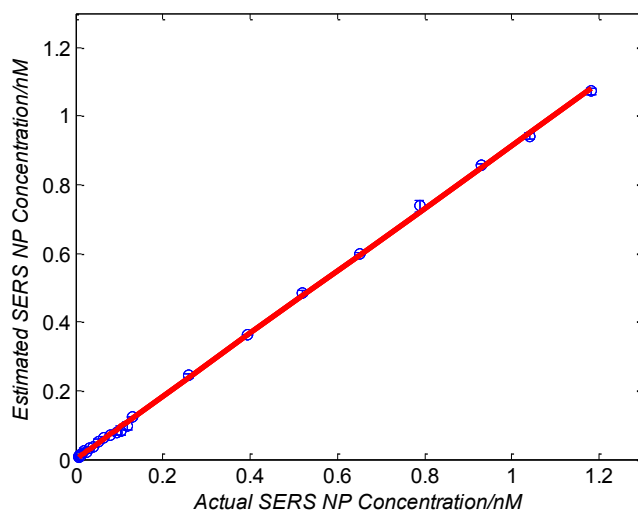


Fig.7.3 Linearity of estimated SERS NP concentration with actual SERS NP concentration.

The data presents a highly linear relationship between estimated SERS NP concentrations and actual SERS NP concentrations with $R^2=0.99$ (Fig.7.3). Fig.7.4 is a close up view of the low concentration part in Fig.7.3. It can be seen that the high linearity was maintained for SERS NPs concentrations even below 10 pM. Defining sensitivity as the concentration of SERS NPs

detectable with a unity signal-to-noise ratio, our sensitivity is estimated as $\sim 1\text{pM}$. To clarify, when reporting nanoparticle concentrations, we report the number density of nanoparticles and these concentrations should not be confused with the effective Raman reporter concentrations.

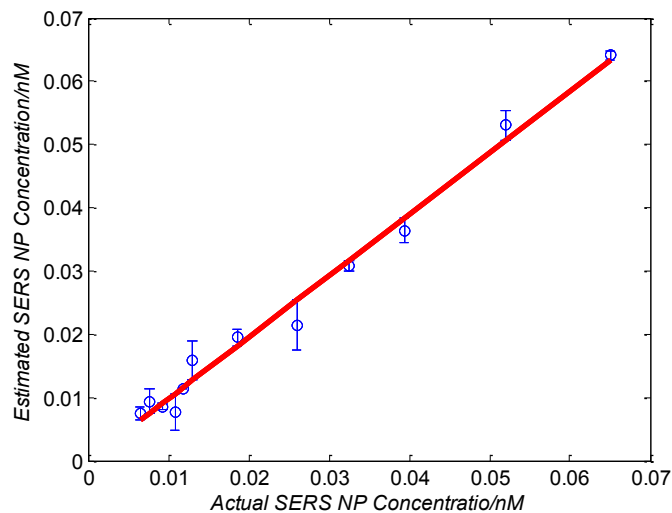


Fig.7. 4 Sensitivity of detected SERS NP.

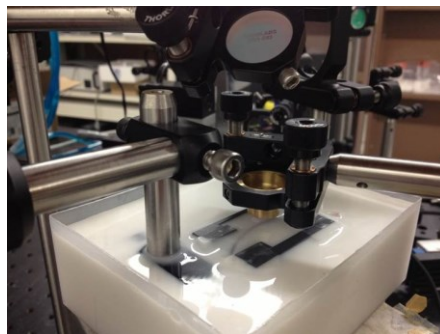


Fig.7.5 Photograph setup used to measure maximum penetration depth.

To estimate the maximum depth of penetration of our system for possible future *in vivo* applications we used a tissue mimicking phantom with 1.3 nM SERS NPs inside a Tygon tubing. This high concentration may be achieved by magnetic trapping of tens to hundreds of cells labelled with hundreds to thousands of SERS NPs. Fig.7.5 shows the photograph setup used to measure maximum penetration depth. The maximum depth of penetration was 2 mm in a solution of Intralipid with reduced scattering coefficient measured as $\mu_s' = 12.5 \text{ cm}^{-1}$. Therefore, the maximum depth of penetration in tissue with an μ_s' of $\sim 10 \text{ cm}^{-1}$ is $\sim 2.5 \text{ mm}$.

7.3.2 Crosstalk

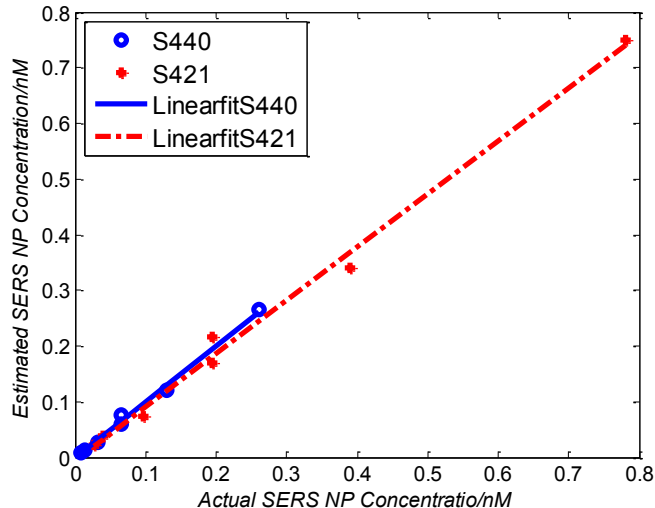


Fig.7.6 Detection of S440 and S421 SERS NPs mixed with concentration ratio of 1:3.

To investigate multiplexing capabilities, we quantified crosstalk from varying types of potential interfering SERS NPs. Using multiple concentrations from 10pM to 1.3nM of S440 SERS NPs, the estimated concentration of S420 SERS NPs was below the noise of the system when no S420 SERS NPs were present. Likewise, using multiple concentrations from 10pM to 1.3nM of S420 SERS NPs, the estimated concentration of S440 SERS NPs was below the noise of the system when no S440 SERS NPs were present. Further, using multiple concentrations of mixed S440 and S421 SERS NPs with concentration ratio of 1:3, the data presents highly linear relationships between estimated SERS NP concentrations and actual SERS NP concentrations with $R^2=0.99$ (Fig.7.6) down to ~ 10 pM of SERS NP S440. Other groups have performed additional investigations to demonstrate 10 or more variants of SERS NPs can be de-mixed with low crosstalk [15].

7.3.3 Non-specific binding

To quantify the specificity of binding of folate conjugated SERS NPs to folate receptors we used a commercial Raman microscope (Nicolet Almega XR Micro and Macro Raman Analysis System, Thermo Fisher Scientific Inc., Waltham, USA). This permitted us to focus on single cells or groups of cells mounted on a slide after 3 washing steps, while avoiding possible SERS NPs in the surrounding media. Six samples were prepared by using HeLa (high folate receptor expression)

and ZR-75-1 (low folate receptor expression) cell lines. HeLa cells and ZR-75-1 cells were incubated for 4 hours respectively with: a) medium only; b) non-functionalized SERS NPs in medium; c) folate-conjugated SERS NPs in medium. The SERS spectrum detected from the six samples are shown in Fig.7.7. HeLa cells incubated with folate-conjugated SERS NPs generated much higher SERS signals than the other five samples, which prove that folate-receptor positive cells accumulated more folate-conjugated nanoparticles. The detected SERS signal from HeLa cells was 12 times higher than the SERS signal from ZR-75-1 cells. This 1:12 non-specific binding ratio may vary depending on the cell type and it is expected that specificity due to antibody or peptide targeting could be significantly higher. SERS signal from red blood cells mixed with equivalent-levels of folate-targeted SERS NPs was not measurable. In addition, fluorescence and Raman microscopy validate that both MNPs and SERS NPs were bound to HeLa cells even after washing steps.

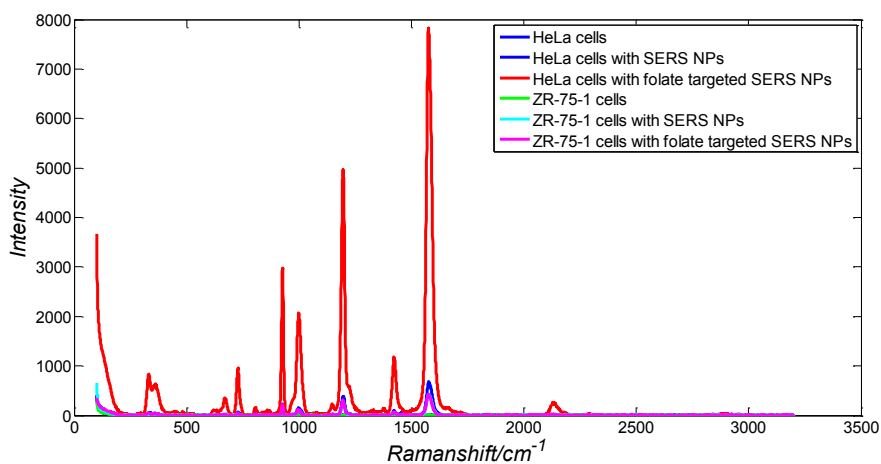


Fig.7.7 SERS signal due to 780 nm excitation wavelength from HeLa cells incubated with medium only, HeLa cells incubated with SERS NPs in medium, HeLa cells incubated with folate targeted SERS NPs in medium, ZR-75-1 cells incubated with medium only, ZR-75-1 cells incubated with SERS NPs in medium, and ZR-75-1 cells incubated with folate targeted SERS NPs in medium, respectively.

7.3.4 Magnetic trapping at 1cm/s mean flow velocity

5×10^5 HeLa cells were incubated with both folate-conjugated SERS NPs and MNPs (magnetic-fluorescent bead) for 4 hours, with fluorescence images demonstrating MNP targeting on HeLa cells. Possible shorter incubation times and *in vivo* targeting need to be explored in the future. The mean flow velocity (defined as volumetric flow rate divided by cross-sectional area) of HeLa cells mixed with 10 mL PBS inside the 1-mm inner diameter Tygon tubing was set as 1 cm/s. The

detected SERS spectrum changing with the magnetic trapping time is shown in Fig.7.8. SERS signal intensity was determined by the magnetically-trapped HeLa cells (incubated with both SERS NPs and MNPs) in the optical focal volume, hence the SERS NPs concentration at the focus. For comparison, SERS signals from samples of HeLa cells incubated with folate-conjugated SERS NPs only, and HeLa cells incubated with folate-conjugated MNPs only were detected, as shown in Fig.7.9. It is clear that only HeLa cells incubated with both folate-conjugated SERS NPs and MNPs exhibited increasing SERS signals with magnetic trapping time. No such increase was observed in the absence of a magnetic field gradient.

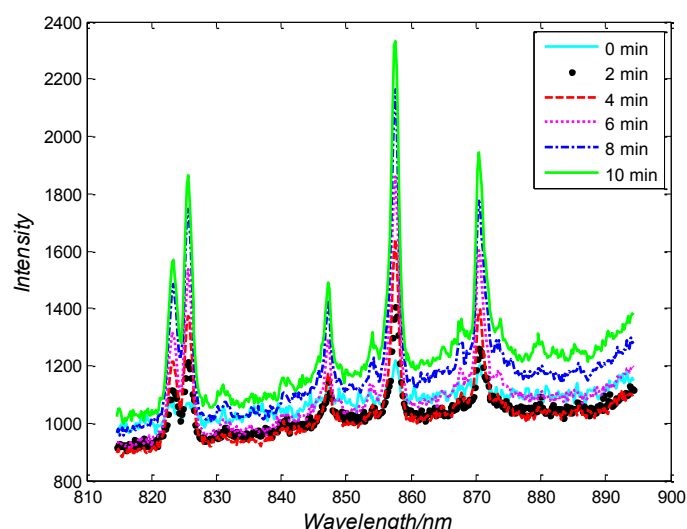


Fig.7.8 SERS spectrum from HeLa cells targeted with both SERS NPs and MNPs at different magnetic trapping time for 1cm/s flow velocity inside 1-mm diameter Tygon tubing.

Magnetic trapping and SERS detection were performed using different concentrations of labelled HeLa cells as shown in Fig7.10. After incubation with both folate-conjugated SERS NPs and MNPs, serial dilutions corresponding to 1/2, 1/8, 1/16, 1/64, and 1/128 of 2×10^5 HeLa cells were re-suspended in 10 mL PBS. These serial diluted samples were flowed through 1-mm diameter Tygon tubing at 1 cm/s mean flow velocity. The estimated SERS NP concentrations in the focal zone increased with magnetic trapping time as shown in Fig.7.10, while Fig.7.11 presents the details for three low cell concentration samples. Discrete trapping events were observed in the SERS signal for low cell concentration samples, which we believe were due to trapped cells rather than free NPs or NPs washed off the cells since only HeLa cells dual labeled with both folate-conjugated SERS NPs and MNPs were detectable as shown in Fig.7.9. The discrete increases of

estimated SERS NP concentration were at least 10 pM which corresponds to ~100 SERS NPs trapped in the focal zone. Because there may be hundreds or more SERS NP per cell the discrete increases in SERS signals are most likely due to single cell trapping or trapping of cell clusters. Variability in the step increases could be due to NP loading variance or cell clustering, however, if cells are loaded with >100 SERS NPs we are sensitive to single cell trapping. The result also shows that we are able to detect ~ 300 CTCs per mL in a total volume of 10 mL within 7 min. Detection of clinically-relevant levels of CTCs (~1-10 CTCs per mL) can be achievable if longer magnetic trapping times or larger volumes are used. Fig.7.12 demonstrated the relationship between estimated SERS NP concentrations in focal zone and cell concentrations, using the same data for Fig.7.10, at magnetic trapping time of 900 seconds and 1200 seconds respectively. The data presents a highly linear relationship between estimated SERS NP concentrations and cell concentrations in PBS solution with a coefficient of determination $R^2=0.99$. For *in vivo* applications, quantitation of nanoparticle concentrations or CTCs may be more challenging than present *ex-vivo* experiments.

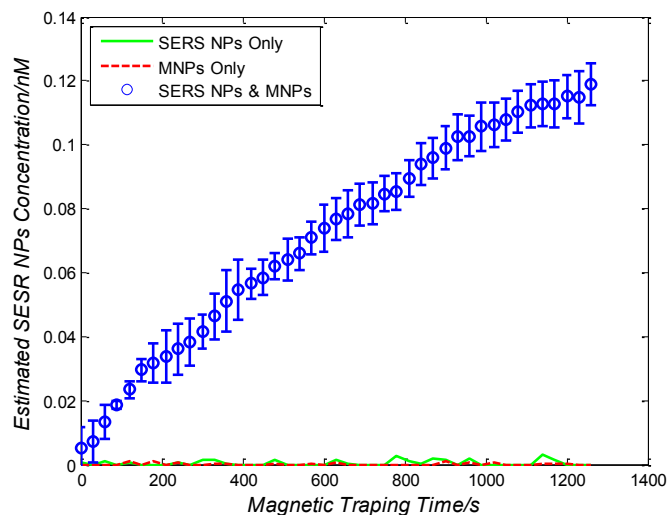


Fig.7.9 Estimated SERS NP concentration at focal zone detected at different magnetic trapping time for 1cm/s flow velocity inside 1-mm diameter Tygon tubing. Three types of cell preparation were made: HeLa cells incubated with SERS NPs only, HeLa cells incubated with MNPs only, and HeLa cells incubated with both SERS NPs and MNPs, respectively.

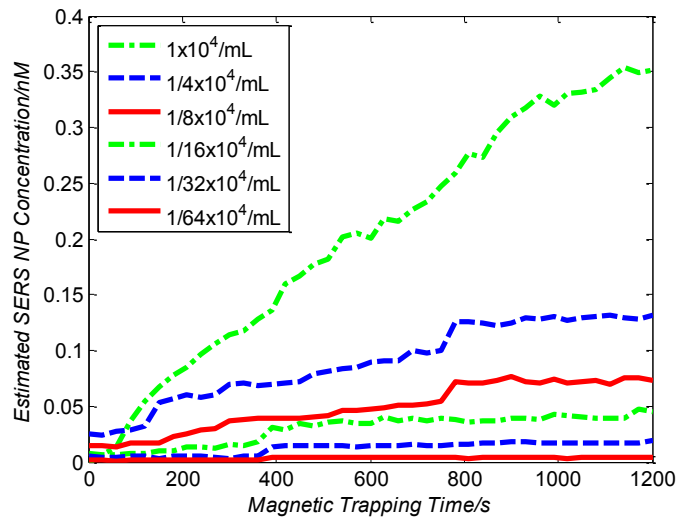


Fig.7.10 Estimated SERS NP concentration at focal zone detected at different magnetic trapping time for different labelled cell concentrations

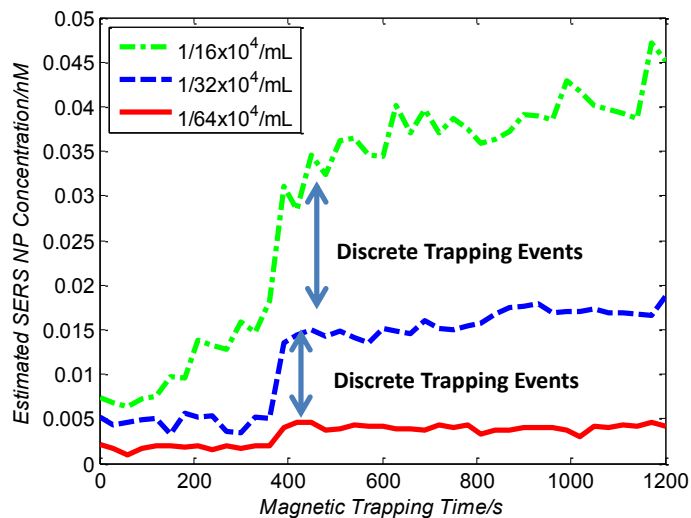


Fig.7.11 Discrete events observed in SERS signals from low cell concentration samples.

7.3.5 Magnetic trapping at different flow velocities

We investigated magnetic trapping at different flow velocities ranging from 0.2cm/s to 12 cm/s as shown in Fig.7.13. These flow velocities are representative of physiological flow velocities in peripheral vessels where future magnetic trapping experiments could be conducted *in vivo*. It can be seen that the magnetic trapping speed increased with the increasing flowing velocity. Therefore, our system demonstrated its ability to trap flowing cells within a large flow velocity range.

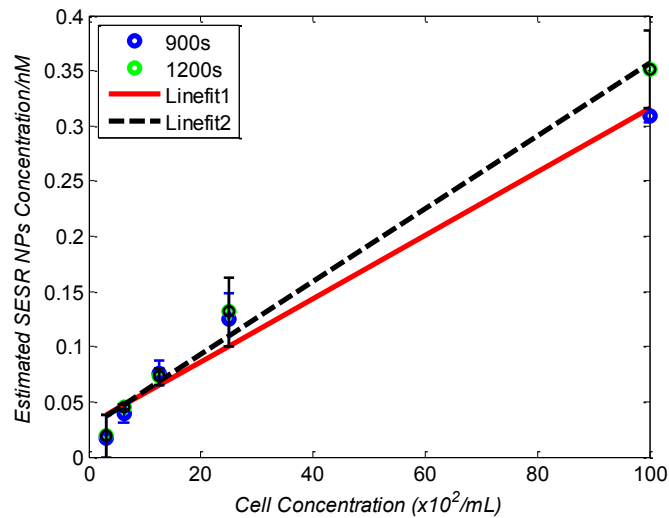


Fig.7.12 Relationship between estimated SERS NP concentrations in focal zone and cell concentrations, at magnetic trapping time of 900 seconds and 1200 seconds respectively.

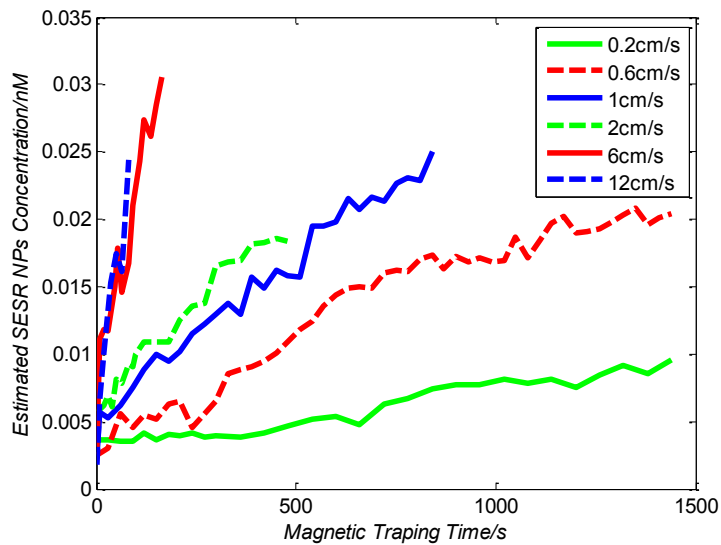


Fig.7.13 Estimated SERS NP concentration at focal zone detected from HeLa cells targeted with both folate-conjugated SERS NPs and MNPs as a function of magnetic trapping time inside 1-mm diameter Tygon tubing for different flow velocities.

7.3.6 Detection of discrete trapping events in blood

Approximately 100,000 dual-nanoparticle labeled HeLa cells were mixed in 10mL of rat blood. The mixture was flowed through 1mm-inner-diameter Tygon tubing at a flow velocity of 1cm/s with both incident light and the cone magnet directed at the top of the tubing. Discrete trapping events were observed in the SERS signal shown in Fig.7.14.

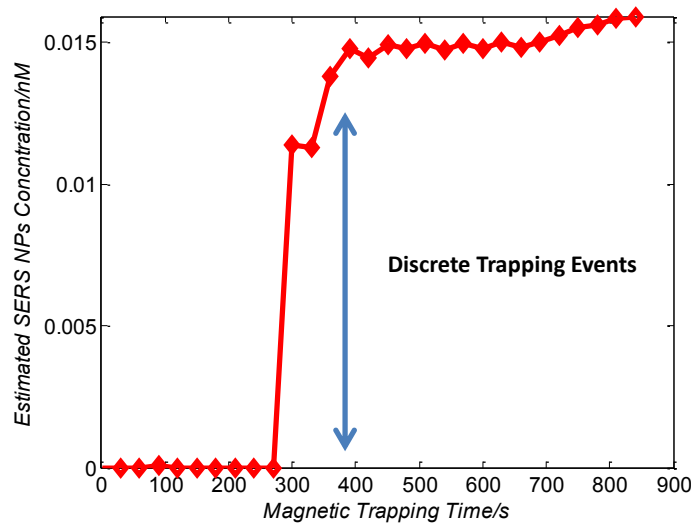


Fig.7.14 Estimated SERS NP concentration at focal zone detected from HeLa cells targeted with both SERS NPs and MNPs at different magnetic trapping time mixed with 10 ml rat blood inside 1-mm diameter Tygon tubing.

7.4 Discussion

To our knowledge, this is the first report of using both SERS NPs and MNPs to achieve magnetic enrichment and trapping of cancer cells mixed with circulating PBS or blood. The present work offers significant promise for future SERS-based multiplex detection of CTCs and could have both *ex vivo* and *in vivo* applications. *In vivo* clinical applications could involve a subject wearing a magnet for an extended period of time to ensure trapping of adequate numbers of CTCs. For *ex vivo* applications, CTC detection in blood samples might be considered similar to present work. Specificity can be further improved by use of antibodies or peptides and the targeting of multiple ligands.

SERS signals from HeLa cells targeted with only SERS NPs or only MNPs were well below the sensitivity of our system, while the SERS signals from HeLa cells targeted with both SERS NPs and MNPs increased with the magnetic trapping time.

The unity-SNR sensitivity was ~ 1 pM. The minimum number of SERS NPs detected within our optical focus is estimated to be only ~ 100 , lower than that reported in [20], which is 600. [21] reported detection of single SERS NPs. Our data suggests we can detect trapping of single cells labelled with hundreds of NPs. Indeed, brighter SERS NPs and enhanced-sensitivity detection

may offer future improvements. Presently for simplicity we use only a few spatial channels (~5 vertical pixels) of our imaging spectrometer system. The detection limit can potentially be further improved by using a fiber bundle to fully utilize all possible spatial channels on our EMCCD and by improving matching of numerical apertures between our spectrometer and detection optics. Additionally, the laser power used in our experiment was about 54 mW measured after the objective lens, slightly less than other groups [15]. In the future, improved signal-to-noise or deeper penetration might be achieved by increasing the laser power. Using the long dimension of our EMCCD for spectral discrimination may facilitate a wider spectral range to improve signal-to-noise and enhance multiplexing capability.

The overexpression of folate receptor on HeLa cells was reported as $\sim 10^5$ receptors per cell [22]. In our experiments, the ratio of SERS NPs to HeLa cells was approximately 20000 to 1. Since the minimum number of SERS NPs detected within our optical focus is estimated to be only ~ 100 , only 1 cell needs to be trapped in order to be detectable using our system if there were 200 SERS NPs targeted on each HeLa cell. This also helps to explain the discrete trapping events observed in Fig.7.11 and Fig.7.14. The discrete increases of estimated SERS NP concentration were at least 10 pM which corresponds to ~ 100 more SERS NPs trapped in the focal zone. The discrete trapping events indicate one cell or several cells simultaneously trapped by the magnet.

Our present study is limited to using tumor cells pre-labelled with nanoparticles. Future work should optimize protocols for targeting circulating tumor cells in whole blood, both *ex vivo* and *in vivo*. Serial dilution experiments indicate it should be possible to detect low clinically-relevant concentrations of CTCs using prolonged trapping times.

Since folate receptor is overexpressed in many cancer cells, MNPs decorated with folate might target several kinds of tumor cells. Therefore, decorating several flavors of SERS NPs with different antibodies can be potentially used for targeting different types of tumor cells to achieve multiplex detection. Targeting different receptors with multiple SERS NPs may additionally enhance specificity of a single CTC cell type. Immune stealth should also be investigated. For some applications including *ex vivo* procedures, immune-suppressants could mitigate immune-cell non-specific uptake. If extraction methods are developed, the enriched population of cells could be further sorted with alternative techniques such as flow cytometry. While a number of additional

research directions appear promising, the present study offers critical feasibility to motivate future work.

7.5 Conclusion

We have demonstrated magnetic enrichment and detection of CTCs with folate-conjugated MNPs and SERS NPs. This technique could be used in either *ex vivo* blood samples or *in vivo*, where a patient could wear a magnet for a sufficient time to detect adequate numbers of CTCs. We hope that present *ex vivo* experiments may pave the way to create new tools in the detection of and therefore prediction of high risk malignancy that requires early aggressive systemic therapy.

Bibliography

- [1] B. Weigelt, J. L. Peterse, and L. J. van't Veer, "Breast cancer metastasis: markers and models," *Nat. Rev. Cancer* 5, 591–602 (2005).
- [2] R. A. Ghossein, S. Bhattacharya, J. Rosai, "Molecular detection of micrometastases and circulating tumor cells in solid tumors," *Clin. Cancer Res.* 5, 1950–1960 (1999).
- [3] M. C. Miller, G. V. Doyle, L. W. Terstappen, "Significance of Circulating Tumor Cells Detected by the CellSearch System in Patients with Metastatic Breast Colorectal and Prostate Cancer," *J. of oncology*, vol. 2010, Article ID 617421, 8 pages, (2010).
- [4] R. F. Swaby, M. Cristofanilli, "Circulating tumor cells in breast cancer: a tool whose time has come of age," *BMC medicine* 9, 43 (2011).
- [5] D. C. Danila, M. Fleisher, H. I. Scher, "Circulating tumor cells as biomarkers in prostate cancer," *Clin. Cancer Res.*, 17 (12), 3903–3912 (2011).
- [6] F. Tanaka, K. Yoneda, N. Kondo, M. Hashimoto, T. Takuwa, S. Matsumoto, Y. Okumura, S. Rahman, N. Tsubota, T. Tsujimura, K. Kuribayashi, K. Fukuoka, T. Nakano, S. Hasegawa, "Circulating tumor cell as a diagnostic marker in primary lung cancer," *Clin. Cancer Res.*, 15 (22): 6980–6986 (2009)
- [7] B. P. Negin, S. J. Cohen, "Circulating tumor cells in colorectal cancer: past, present, and future challenges," *Current Treatment Options in Oncology*, 11 (1-2), 1–13 (2010).
- [8] W.J. Allard, J. Matera, M.C. Miller, M. Repollet, M.C. Connelly, C. Rao, A.G. Tibbe, J.W. Uhr, L.W. Terstappen, "Tumor cells circulate in the peripheral blood of all major carcinomas but not in healthy subjects or patients with nonmalignant diseases," *Clin. Cancer Res.*, 10, 6897–6904 (2004).
- [9] S. Negrath, L. V. Sequist, S. Maheswaran, D. W. Bell, D. Irimia, L. Ulkus, M. R. Smith, E. L. Kwak, S. Digumarthy, A. Muzikansky, P. Ryan, U. J. Balis, R. G. Tompkins, D. A. Haber, M. Toner, "Isolation of rare circulating tumor cells in cancer patients by microchip technology," *Nature*, 450, 1235–1239 (2007).
- [10] K. Kazunori, Y. Y. Huang, N. Lane, M. Huebschman, J. W. Uhr, E. P. Frenkel, X. Zhang, "Microchip-based immunomagnetic detection of circulating tumor cells," *Lab on a Chip*, 11 (20), 3449–3457 (2011).

- [11] S. Zheng, H. Lin, J. Q. Liu, M. Balic, R. Datar, R. J. Cote, T. C. Tai, "Membrane microfilter device for selective capture, electrolysis and genomic analysis of human circulating tumor cells," *J. Chromatogr*, 1162(2), 154–161 (2007).
- [12] E. I. Galanzha, E. V. Shashkov, T. Kelly, J. W. Kim, L. Yang, V. P. Zharov, " *In vivo* magnetic enrichment and multiplex photoacoustic detection of circulating tumor cells, " *Nature Nanotech.*, 4, 855-860 (2009).
- [13] C. W. Wei, J. Xia, I. Pelivanov, X. Hu, X. Gao, M. O'Donnella, "Trapping and dynamic manipulation of polystyrene beads mimicking circulating tumor cells using targeted magnetic/photoacoustic contrast agents," *J. of Biomed. Optics*, 17(10), 101517 (2012).
- [14] C. M. O'Brien, K. D. Rood, K. Bhattacharyya, T. DeSouza, S. Sengupta, S. K. Gupta, J. D. Mosley, B. S. Goldschmidt, N. Sharma, J. A. Viator, "Capture of circulating tumor cells using photoacoustic flowmetry and two phase flow," *J. of Biomed. Optics*, 17, 061221 (2012).
- [15] C. L. Zavaleta, B. R. Smith, I. Walton, W. Doering, G. Davis, B. Shojaei, M. J. Natan, S. S. Gambhir, "Multiplexed imaging of surface enhanced Raman scattering nanotags in living mice using noninvasive Raman spectroscopy," *PNAS*, 106 (32), 13511–13516 (2009).
- [16] X. Wang, X. Qian, J. J. Beitler, G. Chen, F. R. Khuriet, M. M. Lewis, H. J. C. Shin, S. Nie, D. M. Shin, "Detection of Circulating Tumor Cells in Human Peripheral Blood using Surface-Enhanced Raman Scattering Nanoparticles," *Cancer Res.*, 71(5), 1526–1532 (2011).
- [17] B. Jun, M. S. Noh, J. Kim, G. Kim, H. Kang, M. Kim, Y. Seo, J. Baek, J. Kim, J. Park, S. Kim, Y. Kim, T. Hyeon, M. Cho, D. H. Jeong, Y. Lee, "Multifunctional Silver-Embedded Magnetic Nanoparticles as SERS Nanoprobes and Their Applications," *Small*, 6(1), 119–125 (2010).
- [18] P. Quaresma, I. Os'orio, G. D'oria, P. A. Carvalho, A. Pereira, J. Langer, J. P. Araújo, e I. Pastoriza-Santos, L. M. Liz-Marz'an, R. Franco, P. V. Baptistac, E. Pereira, "Star-shaped magnetite@gold nanoparticles for protein magnetic separation and SERS detection," *RSC Adv.*, 4, 3659-3667 (2013).
- [19] P. S. Low and A. C. Antony, "Folate receptor-targeted drugs for cancer and inflammatory disease", *Adv Drug Deliv Rev*, 56, 1055–1058 (2004).

- [20] S. Keren, C. Zavaleta, Z. Cheng, A. de la Zerda, O. Gheysens, S. S. Gambhir, “Noninvasive molecular imaging of small living subjects using Raman spectroscopy,” *PNAS*, 105 (15), 5844–5849 (2008).
- [21] S. Nie, S. R. Emory, “Probing Single Molecules and Single Nanoparticles by Surface-Enhanced Raman Scattering,” *Science*, 275, 1102-1106 (1997).
- [22] G. Destito, R. Yeh, C.S. Rae, M.G. Finn, and M. Manchester, “Folic Acid-Mediated Targeting of Cowpea Mosaic Virus Particles to Tumor Cells,” *Chemistry & Biology*, 14, 1152–1162 (2007)

8 Multimodality photoacoustic and Raman imaging of magnetically-trapped tumor cells

8.1 Introduction

Photoacoustic (PA) imaging is a novel imaging technology for visualizing optically-absorbing structures based on the PA effect: the absorption of electromagnetic energy, such as optical energy, produces acoustic waves by a pressure rise via thermoelastic expansion. The PA effect was first reported by Alexander Graham Bell in 1880 [1]. PA imaging poses no health hazard compared with ionizing x-ray radiation, due to the nonionizing waves PA imaging employs. PA imaging outperforms traditional optical imaging in spatial resolution feature since the ultrasound scattering is weaker than optical scattering by two or three orders of magnitude. On the other hand, PA imaging is of high optical contrast compared to far lower mechanical contrast of ultrasound imaging. In addition, PA signals are sensitive to hemoglobin concentration and to oxygen saturation due to different optical absorption spectra of oxygenated and deoxygenated hemoglobin. There has been remarkable progress on employing PA imaging in biomedical applications in the last decade, which makes PA imaging a promising technique for early diagnosis and monitoring of disease [2].

PA tomography generates images with optical contrast and ultrasonic spatial resolution at significant tissue depths [3] [4]. PA microscopy (PAM) was used to produce high-contrast images by raster-scanning a light-delivery and acoustic detection probe mechanically [5][6]. Furthermore, newly developed optical-resolution PAM demonstrated its ability to image single capillaries or even blood cells with high optical lateral resolution defined by the focused micron or submicron scale laser spot in real-time [7-10]. However, differentiation of PA signals is non-trivial hence specificity can be poor. It would be ideal if we could detect and identify the tumor cells inside the vasculature as well. Surface-enhanced Raman spectroscopy is one of the promising multiplexed imaging techniques used for this application.

Raman scattering was first reported in 1928 by C. V. Raman et al. [11]. It is the inelastic scattering of a photon from an atom or a molecule when light interacts with matters, which provides rich information on the structure and composition of the atom or molecule, a spectral fingerprint. Raman spectroscopy is based on the measurement of the vibrational energy levels of

chemical bonds through Raman scattering. It is a non-destructive and non-invasive technique which can also be carried out under a wide range of conditions [12]. Multiple narrow line-widths of spectral peaks of Raman spectrum enables extremely high multiplexing capabilities of Raman spectroscopy. However, the application of Raman spectroscopy is limited by its inherent weak intensity. The emergence of surface-enhanced Raman scattering (SERS) broke through the bottleneck by dramatically enhancing the Raman scattering signal by factors as much as 10^{14} - 10^{15} , which is due to laser excitation of molecules adsorbed on nano-patterned metal surfaces or nanoparticles.

Surface-enhanced Raman spectroscopy with SERS nanoparticles (SERS NPs) has recently been reported and offers ultralow background and very high multiplexing capabilities, important for specificity [13-15]. S. Gambhir's group at Stanford University recently showed that they could detect and classify multiple types of Raman nanoparticles injected into live mice with picomolar sensitivities [16]. This work demonstrates the ability to detect a multiplicity of optical probes with high sensitivity *in vivo*. In 2011, Wang et al., demonstrated using SERS NPs to detect CTCs in human peripheral blood [17]. However, their method lacked an enrichment technique.

Detection of circulating tumor cells (CTC) is of great importance for tumor research since CTCs is a common marker of cancer metastasis. However, *in vivo* detection of CTCs is difficult due to its low concentration in blood. In 2009, Zharov's group reported rapid photoacoustic detection of magnetically captured CTCs [18]. In their experiment, circulating breast cancer cells were targeted by functionalized magnetic nanoparticles (MNPs) and hence were captured under a magnet. Also, functionalized gold-plated carbon nanotubes acted as a second contrast agent for photoacoustic imaging. Their experiment demonstrated the ability to concentrate CTCs from a large volume of blood in the vessels of tumor-bearing mice. Recently M. O'Donnell's group at University of Washington demonstrated magnetically trapping and manipulating of CTCs-mimicking flowing polystyrene beads [19]. Magneto-sensitive nanospheres and optical absorptive gold nanorods were used for targeting the polystyrene beads. Their results showed efficient magnetic trapping in a stream with a flow rate up to 12 ml/min. However, similar to Zharov's group, their setup did not show multiplexing ability to improve specificity of detection.

To achieve blood microvasculature imaging and improve the specificity for molecular imaging application with a multi-modality approach, we propose combining PAM with SERS imaging using targeted magnetic and SERS probes. We demonstrated both phantom and *in vivo* co-registered images. This technology may play a key role in cancer research, molecular diagnostics and personal medicine.

8.2 Methods

8.2.1 System description

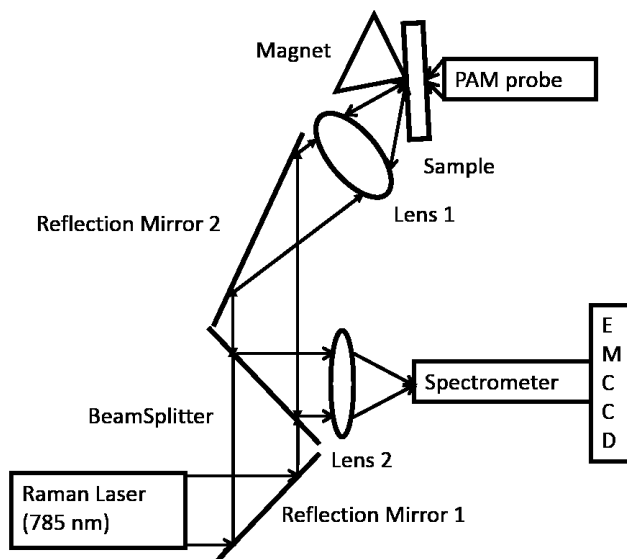


Fig.8.1. Schematic diagram of photoacoustic and Raman imaging system.

The schematic of our combined PAM and SERS imaging system is shown in Fig.1. The excitation laser source for SERS imaging is a 785 nm Raman laser (FB-785-350-FS-FS-1-1, RGBLase LLC, Fremont, CA, USA) with 0.4 nm 20-dB spectral line-width and up to 350mW output (while the power used in our experiment was 54mW). A custom Raman imaging spectrometer (RASPPEC - 785-HR, P&P Optica Inc. Kitchener, ON, Canada) was used to capture Raman spectra: A 15 μ m x 26mm slit was used as the input aperture ($f\#$: 3.5). The incident light was then collimated and transmitted through a 900 l/mm gel-grating. The spectral range of the Raman spectrometer is 815nm to 895nm, along with a 10 cm^{-1} spectral resolution. A liquid-cooled Electron-Multiplying (EM) CCD camera (DU971N-UV, Andor Technology) was used for detection and signal acquisition, with very low dark current noise (0.0002 e-/pix/sec at -100 $^{\circ}$ C) and \sim 50% quantum

efficiency at peak wavelengths, ~30% in the wavelength range we used. There are 1600×400 pixels on the EMCCD array, while pixel element size is 16×16 μm. A dichroic beam splitter (DMSP805L, Thorlabs) was used to transmit the incident excitation laser beam while reflect the SERS signals towards Raman spectrometer. A 0.3 NA lens (AC127-019-B-ML, Thorlabs) was used to focus reflected SERS signals from beam splitter into the input aperture of the imaging spectrometer. An aspheric lens (A240TM-B, Thorlabs, 0.5 NA, 8mm focal length) was used for illumination of excitation laser beam onto sample and collection of the SERS signals from sample. A strong magnetic field with high magnetic field gradient was generated by a 1” tall, 1” diameter N50 cone magnet (Cone0100N, SuperMagnetMan) pointing at the optical focus of lens 1. A custom designed PAM probe using 532-nm laser source and 50 MHz ultrasound transducer was placed to the other side of sample to achieve PA imaging. Sample was placed on a three-axis translation stage which is not shown on the system diagram.

8.2.2 Nanoparticles and cell preparation

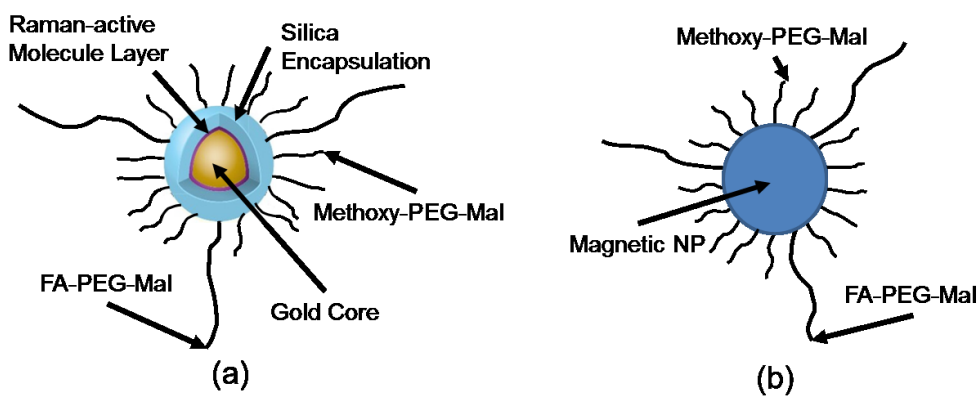


Fig.8.2. Diagrammatic figures of the conjugated (a) SERS NP and (b) MNP. PEG, polyethylene glycol; Mal, maleimide; FA, folate.

In our studies, SERS NPs (S440 & S420, Oxonica Materials Inc., Mountain View, CA, USA) consisted of a 60 nm-diameter Au core and a 30 nm silica shell, with an overall diameter of 120 nm. A Raman active molecular monolayer is adsorbed onto the Au core which is unique for different types of SERS NPs. Since many cancer cells (breast, lung, kidney, ovary, colon, brain, and myelogenous leukemia) significantly overexpress folate receptors to facilitate rapid cell division, we conjugated nanoparticles with folate to target folate receptors of cancer cells [20]. To target folate receptors, thiolated SERS NPs (1.3 nM) were added to a solution of folate-PEG5k-maleimide (Nanocs Inc., PG2-FAML-5k, 0.8mM) and methoxy-PEG2k-maleimide (Sigma™

Aldrich, 4mM) and mixed at room temperature by a rocker overnight. Excess folate-PEG-maleimide was separated from SERS NPs by three runs of centrifugation (14,000 RPM, 5 min), and resuspension in MES (Fisher Science) buffer.

MNPs (screenMAG-Thiol, chemicell™ GmbH) are composed of 500 nm-diameter magnetic fluorescent silica particles with nearly 1 million SH- group per particle. Under the similar procedure as SERS NPs targeting, a solution of folate-PEG5k-maleimide (Nanocs Inc., PG2-FAML-5k, 0.8mM) and methoxy-PEG2k-maleimide (Sigma Aldrich, 4mM) was added to thiolated MNPs (1.25nM) and mixed at room temperature on a rocker overnight, followed by three runs of centrifugation (14,000 RPM, 5 min) to eliminate excess folate-PEG-maleimide and then re-suspension in MES buffer. Diagrams of SERS NPs and MNPs are shown in Fig. 2.

HeLa (cervical cancer, folate receptor positive) cells were cultured according to the standard procedure, and were incubated with serum-free medium containing both SERS NPs and MNPs at 37 °C for 4 hours before use.

8.3 Results

8.3.1 System performance

In our multimodality imaging system, the lateral optical resolution of PAM was evaluated by imaging a $\sim 7.5\text{-}\mu\text{m}$ carbon fiber using our previous reported method [21]. The corresponding lateral resolution was $\sim 50\mu\text{m}$. Demixing and quantitative analysis of Raman spectra were based on classic least-squares methods. Detected SERS NP concentrations presented a highly linear relationship with actual concentrations of SERS NPs with $R^2=0.99$, while the lowest concentration of SERS NPs detected by our imaging setup was 10 pM. Intralipid solution was used to mimic the turbidity of human tissue, where a maximum imaging depth of ~ 2.5 mm was obtained by using 1.3 nM SERS NPs inside Tygon tubing.

8.3.2 Phantom studies

In our phantom studies, HeLa cells ($\sim 5 \times 10^5$, in 1mL rat blood) incubated with both SERS NPs and MNPs flowed inside a 200- μm inner-diameter acrylic capillary tubing (CT200-250-5, Paradigm Optics). A syringe pump (NE-300, New Era Pump Systems, Inc.) was used to set the flow. An aspheric lens (lens 1 in Fig. 1) focused the excitation laser beam on the acrylic capillary tubing. A

cone magnet pointed at the aspheric lens focus was used for generating a high magnetic field gradient for magnetic trapping. PAM probe was co-focused with the aspheric lens to capture the structure image at the same focus location. Fig. 3 shows the co-registered image with pseudo-color, demonstrating a 2mm×2mm image of rat blood with targeted HeLa cells flowing inside a 200- μ m inner-diameter acrylic capillary tubing. Signal intensity is normalized. For demonstration, PAM and SERS signals are shown in red and blue color maps, respectively.

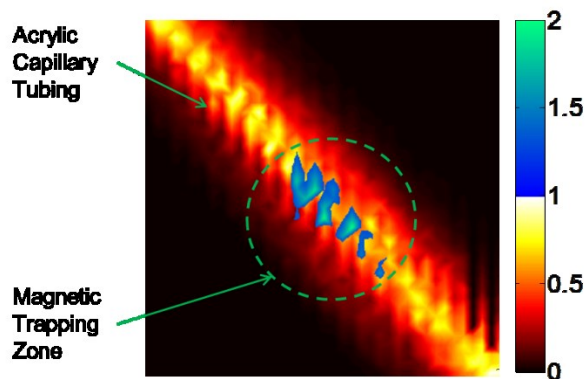


Fig.8.3 Co-registered image with pseudo-color showing 2mm×2mm image of rat blood with targeted HeLa cells floating inside a 200- μ m inner-diameter acrylic capillary tubing. Signal intensity is normalized. PAM and SERS signals are shown in red and blue color maps, respectively.

8.3.3 *In vivo* experiments

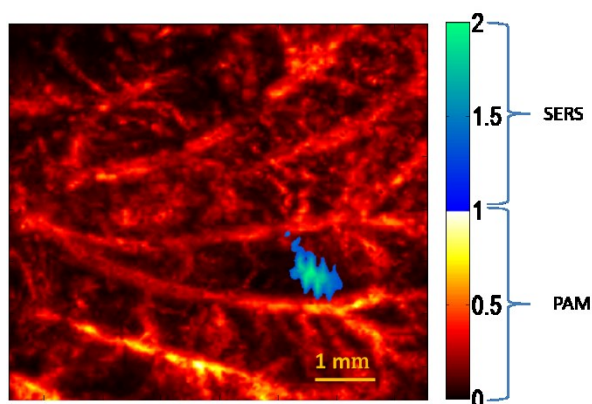


Fig.8.4 Co-registered image with pseudo-color showing 7mm×7mm image of rat ear subcutaneous injected with HeLa cells bound with SERS NPs and MNPs. Signal intensity is normalized. PAM and SERS signals are shown in red and blue color maps, respectively.

In our *in vivo* studies, all experimental animal procedures were conducted in conformity with the laboratory animal protocol approved by the University of Alberta Animal Use and Care Committee. The rat was anesthetized using isoflurane using a breathing anesthesia system (E-Z Anesthesia,

Euthanex Corp.) during image acquisition. HeLa cells ($\sim 5 \times 10^5$, in 50 μL PBS) previous incubated with both SERS NPs and MNPs were subcutaneously injected into a rat ear and imaged using the same setup as shown in phantom studies. Fig. 4 shows the co-registered image with pseudo-color, demonstrating a 7mm \times 7mm image of rat ear. Signal intensity is normalized. For demonstration, PAM signals are shown in red color map while SERS signals are illustrated in blue color map.

8.4 Discussion and conclusions

To our knowledge, this is the first report of using a multimodality photoacoustic and Raman imaging system to achieve co-registered PAM and SERS imaging using both SERS NPs and MNPs. This system is capable to perform PAM imaging with ~ 50 μm lateral resolution and SERS detection at 10 pM SERS NPs concentration limit and up to 2.5 mm imaging depth in tissue mimic phantom. In phantom studies, HeLa cells targeted with both SERS NPs and MNPs in 1 mL rat blood flowing inside a 200- μm inner-diameter acrylic capillary tubing were imaged. For *in vivo* studies, HeLa cells ($\sim 5 \times 10^5$, in 50 μL PBS) targeted with both SERS NPs and MNPs injected into a rat ear by subcutaneous injection were imaged.

The SERS detection limit of 10 pM can be further improved by up to 160 times when using a fiber bundle to fully utilize the 160 channels on our EMCCD. In addition, our present study is focused on one type of SERS NP. Future work should use multiple types of SERS NPs with different targeting to fully demonstrate high specificity and multiplexing capabilities. Also, we subcutaneously injected tumor cells pre-labelled with nanoparticles to the rat ear. In the future, we should work on intravenous injection to mimic magnetic enrichment and SERS detection of CTCs and native targeting CTCs with nanoparticles in whole blood should be further investigated.

We demonstrated a multimodality imaging system which may be used for clinic applications to identify the CTCs in the circulatory system and draw out appropriate amount of CTCs for *in vitro* studies. We hope that present experiments may pave the way to create new tools in the detection of and therefore prediction of high risk malignancy that requires early aggressive systemic therapy.

Bibliography

- [1] A. G. Bell, "On the Production and Reproduction of Sound by Light: the photophone", *Am. J. Sci.* 20, 305-324 (1880)
- [2] M.H. Xu, and L.H., V. Wang, "Photoacoustic imaging in biomedicine", *Rev. Sci. Instr.* 77, 041101 (2006)
- [3] G. Ku and L.H., V. Wang, "Deeply penetrating photoacoustic tomography in biological tissues enhanced with an optical contrast agent", *Optics Letters* 30 (5), 507-509 (2005).
- [4] S.A. Ermilov, T. Khampirad, A. Conjusteau, M.H. Leonard, and R. Laceywell, "Laser optoacoustic imaging system for detection of breast cancer", *Journal of Biomedical Optics* 14(2), 24007 (2009)
- [5] K. Maslov, G. Stoica, and L. H., V. Wang, "*In vivo* dark-field reflection-mode photoacoustic microscopy", *Optics Letters* 30, 625-627 (2005)
- [6] H.F. Zhang, K. Maslov, G. Stoica, and L. H., V. Wang, "Functional photoacoustic microscopy for high-resolution and noninvasive *in vivo* imaging", *Nature Biotechnology* 24, 848-851 (2006)
- [7] K. Maslov, H. F. Zhang, S. Hu, and L. H., V. Wang, "Optical-resolution photoacoustic microscopy for *in vivo* imaging of single capillaries", *Opt. Lett.* 33, 929-931 (2008)
- [8] B. Rao, K. Maslov, A. Danielli, R. Chen, K. K. Shung, Q. Zhou, and L. H., V. Wang, "Real-time four-dimensional optical-resolution photoacoustic microscopy with Au nanoparticle-assisted subdiffraction-limit resolution", *Opt. Lett.* 36, 1137-1139 (2011)
- [9] W. Shi, P. Hajireza, P. Shao, A. Forbrich, and R. J. Zemp, "*In vivo* near-realtime volumetric optical-resolution photoacoustic microscopy using a high-repetition-rate nanosecond fiber-laser", *Opt. Express* 19, 17143-17150 (2011)
- [10] W. Shi, P. Shao, P. Hajireza, A. Forbrich, and R. J. Zemp, "*In vivo* dynamic process imaging using real-time optical-resolution photoacoustic microscopy", *J. Biomed. Opt.* 18, 026001 (2013)
- [11] U.K. Sur, "Surface-Enhanced Raman Spectroscopy: Recent Advancement of Raman Spectroscopy", *Resonance*, 154-164 (2010)
- [12] M. K. Hossain, and Y. Ozaki, "Surface-enhanced Raman scattering: facts and inline trends", *Current Science* 2, 192-201 (2009)

- [13] S. Lin, X. Xie, M.R. Patel, Y.H. Yang, Z. Lin, F. Cao, O. Gheysens, Y. Zhang, S.S. Gambhir, J.H. Rao, and J.C. Wu, “Quantum dot imaging for embryonic stem cells”, *BMC Biotechnol.* 7, 67 (2007)
- [14] J. Rao, A. Dragulescu-Andrasi, H. Yao, “Fluorescence imaging in vivo: recent advances”, *Curr Opin Biotechnol.* 18, 17-25 (2007)
- [15] S. Keren, C. Zavaleta, Z. Cheng, A. de la Zerda, O. Gheysens, and S. S. Gambhir, “Noninvasive molecular imaging of small living subjects using Raman spectroscopy”, *Proc Natl Acad Sci USA.* 105, 5844-5849 (2008)
- [16] C. L. Zavaleta, B. R. Smith, I. Walton, W. Doering, G. Davis, B. Shojaei, M. J. Natan, and S. S. Gambhir, “Multiplexed imaging of surface enhanced Raman scattering nanotags in living mice using noninvasive Raman spectroscopy”, *PNAS* 106 (32), 13511–13516 (2009)
- [17] X. Wang, X. Qian, J. J. Beitler, G. Chen, F. R. Khuriet, M. M. Lewis, H. J. C. Shin, S. Nie, and D. M. Shin, “Detection of Circulating Tumor Cells in Human Peripheral Blood Using Surface-Enhanced Raman Scattering Nanoparticles”, *Cancer Res.*, 71, 1526-1532 (2011)
- [18] E. I. Galanzha, E. V. Shashkov, T. Kelly, J., Yang, L. Kim, and V. P. Zharov, “In vivo magnetic enrichment and multiplex photoacoustic detection of circulating tumor cells”, *Nat. Nano.* 4, 855-860 (2009)
- [19] C. Wei, J. Xia, I. Pelivanov, X. Hu, X. Gao, and M. O’Donnell, “Trapping and dynamic manipulation of polystyrene beads mimicking circulating tumor cells using targeted magnetic/ photoacoustic contrast agents”, *J. Biomed. Optics* 17(10), 101517(2012)
- [20] P.S. Low and A.C. Antony, “Folate receptor-targeted drugs for cancer and inflammatory diseases”, *Adv Drug Deliv Rev*, 56(8), 1055–1058 (2004)
- [21] W. Shi, S. Kerr, I. Utkin, J. C. Ranasinghesagara, L. Pan, Y. Godwal, R. J. Zemp, and R. Fedosejevs, “Optical resolution photoacoustic microscopy using novel high-repetition-rate passively Q-switched microchip and fiber lasers”, *J. Biomed. Opt.* 15, 056017(2010)

9. Conclusion and future prospects

9.1 Work done in this dissertation

The work presented in this dissertation contributes to the long-term vision of multi-modality tools to detect and characterize metastases. Hallmarks of metastases include circulating tumor cells (CTCs) and neoplasm angiogenesis. Angiogenesis is a factor in both invasion at the site of the primary tumor and vascular establishment of metastatic proliferation. To image microvasculature associated with angiogenesis we contributed to the development of novel photoacoustic microscopy (PAM) methods. To detect CTCs, we developed magnetic and surface-enhanced-Raman-scattering (SERS) nanoparticles (NPs) based methods for trapping and optically detecting CTCs with high multiplexing potential for enhanced specificity. Also, we developed a multimodality imaging system to achieve structural, functional and molecular imaging by combining PAM imaging with SERS imaging. Contributions in this dissertation can be divided into three parts: fast imaging speed optical-resolution PAM (OR-PAM), detection of CTCs and multimodality imaging system development.

9.1.1 Realtime OR-PAM

- We demonstrated improving imaging speed of OR-PAM by using various lasers, including a highly compact and potentially inexpensive diode-pumped microchip laser with pulse repetition rates around 10 kHz, and a passively Q-switched fiber laser producing 250 ns pulses at repetition rates of 100 - 300 KHz which is suitable for realtime OR-PAM imaging. Phantom studies demonstrate the ability to image with 7 μ m lateral spatial resolution with the microchip laser system and 15 μ m lateral spatial resolution with the fiber-laser system
- Combined a commercial diode-pumped nanosecond-pulsed Ytterbium-doped 532-nm fiber laser with PRR up to 600 kHz and a fast-scanning mirrors, we first reported a near realtime 3D *in vivo* OR-PAM imaging of mice ear microvasculature at frame rate of 4 frame per second with ~6- μ m optical lateral spatial resolution.
- With further development, we demonstrated our OR-PAM capable of *in vivo* near realtime substained imaging which can be potentially used for near realtime feedback for focusing and

positioning, and realtime imaging of cardiac-induced microhemodynamics in murine microvasculature at frame rate of 30 frames per second.

- We studied the effects of scanning speed and laser-repetition-rate on photoacoustic signals in OR-PAM system, with phantom studies on black tap, human hair and rat blood. The photoacoustic signal change caused by overlapping laser spots from adjacent laser pulses due to temperature-dependent Gruneisen parameter was demonstrated, which may be useful for improving imaging quality and super-resolution technique.

9.1.2 Detection of CTCs

- We demonstrated first time detection of CTCs in PBS or circulating blood with high specificity, ~ 1 pM sensitivity and 2.5 mm penetration depth by targeting cancer cells with both SERS NPs and MNPs and employing SERS imaging system.

9.1.3 Multimodality imaging system

- We developed a multimodality imaging system combined PAM imaging for visualizing vasculature with SERS imaging for detecting CTCs.

9.2 Possible applications

PAM is a multi-scale high contrast imaging tool for visualizing optically-absorbing structures with scalable resolution at accordingly imaging depth. OR-PAM is a novel PAM technique with microscale resolution at millimeter depth in tissue, which is capable to resolve the smallest vascular component as single capillaries. This makes OR-PAM a promising candidate for the diagnosis of cancer at early stages, especially for superficially structures. In addition, OR-PAM endoscopy has been investigated to image internal organs as well. Realtime imaging speed may pave the way of employing OR-PAM for clinical and biological applications. The application of realtime OR-PAM could involve locating the area of interest by using lower resolution imaging technique with large field of view, and then followed by high resolution OR-PAM for more detail information, including structural, functional and molecular imaging.

Detection of CTCs by using SERS detection and magnetic enrichment could have both *in vivo* and *ex vivo* applications. Both applications may involve magnetic enrichment of CTCs by the

subject wearing a magnet for an extended period of time, and then followed by high specificity SERS detection either on site or on samples extracted outside the subject.

Multimodality SERS and PAM imaging can be potentially used for both imaging the immobile metastasis and CTCs. For immobile metastasis, SERS imaging can be used for revealing the biomarker profile, while PAM can be used for providing vascular context. For the detection of CTCs, PAM can be used for guiding the placement of magnet to facilitate extraction of CTCs for further *ex vivo* SERS detection, or to assist in the optimal *in vivo* SERS detection of CTCs.

9.3 Direction of future work

Future work on realtime OR-PAM will involve increasing the imaging field of view, developing high-repetition-rate sources with wide tuning range of wavelength for functional imaging. In addition, a novel super-resolution technique with submicron level resolution may be developed based on present studies on the scanning speed dependence of realtime OR-PAM.

Future work on detection of CTCs will involve improving specificity by using antibodies or peptides to target multiple ligands, and demonstrating *in vivo* detection of CTCs.

Future work on multimodality imaging system will involve improving imaging speed of SERS imaging by using fiber bundle or cylindrical lens to achieve line illumination and detection, demonstrating SERS imaging for *in vivo* imaging with intravenous injection and native targeting CTCs with NPs in whole blood, developing NP-based contrast enhanced PAM imaging to improve the penetration depth and molecular imaging capability, and advancing multimodality imaging system for convenient use and with compact size.

Appendix

Demixing method

In our experiment, we use EMCCD to record the spectrum from different targets. Since there are 400 pixels along the wavelength direction on EMCCD, each spectrum acquired has accordingly 400 pixels within the spectrometer spectral range from 815 nm to 895 nm. The spectrum thus can be plotted based on the values acquired from each pixel.

We acquire pure SERS spectrum of each type of SERS NPs used in our experiment. For example, for SERS NP type A, we can use an array $[NPA] = [NPA_1 \ NPA_2 \ \dots \ NPA_n]$ to present its spectrum collected by the spectrometer, where the subscripts indicate each pixel along wavelength direction. In our experiments, n is 400. Also we collect autofluorescence spectrum before each experiment, which we use an array $[AF] = [AF_1 \ AF_2 \ \dots \ AF_n]$ to present the autofluorescence background. In addition, we use a third order polynomial to fit the back noise which can also be represented by $[B1] = [1/\lambda_1 \ 1/\lambda_2 \ \dots \ 1/\lambda_n]$, $[B2] = [1/\lambda_1^2 \ 1/\lambda_2^2 \ \dots \ 1/\lambda_n^2]$, and $[B3] = [1/\lambda_1^3 \ 1/\lambda_2^3 \ \dots \ 1/\lambda_n^3]$. The spectrum acquired from the target can be expressed as an array $[S] = [S_1 \ S_2 \ \dots \ S_n]$.

The spectrum from the target is a linear combination of SERS NP spectrum and background spectrum. We use an array of weight factors $[C] = [C_1 \ C_2 \ C_3 \ C_4 \ C_5 \ C_6]$ to describe the contribution of the background ($C_1 \ C_2 \ C_3$), the autofluorescence (C_4) and the relative SERS NP concentrations ($C_5 \ C_6$) to the target spectrum. Additional coefficients C_7, C_8, \dots would be needed for inclusion of more nanoparticles. Therefore, the linear relationship of the target spectrum with background, autofluorescence spectrum and spectrum of two types of SERS NPs can be expressed as an equation:

$$[S_1 \ S_2 \ \dots \ S_n] = [C_1 \ C_2 \ C_3 \ C_4 \ C_5 \ C_6] \begin{bmatrix} 1/\lambda_1 & 1/\lambda_2 & \dots & 1/\lambda_n \\ 1/\lambda_1^2 & 1/\lambda_2^2 & \dots & 1/\lambda_n^2 \\ 1/\lambda_1^3 & 1/\lambda_2^3 & \dots & 1/\lambda_n^3 \\ AF_1 & AF_2 & \dots & AF_n \\ NPA_1 & NPA_2 & \dots & NPA_n \\ NPB_1 & NPB_2 & \dots & NPB_n \end{bmatrix}$$

To solve the linear equation, we use classical linear least-squares method with an optional positivity constraint, by means of using matlab function `lsqnonneg`. Classic-linear-least-squares

method is used to find the linear combination of component spectra that most closely matches the SERS spectrum of the target. The weight factors derived by the linear-least-squares method are proportional related to the concentration of each component. This method can generate accurate results since the change of spectra of each component after mixing is neglectable.

Bibliography

A. A. Oraevsky and A. A. Karabutov, "Optoacoustic Tomography", in Biomedical Photonics Handbook, ed. by T. Vo-Dinh, CRC Press, Boca Raton, Florida, Vol. PM125, Chapter 34 (2003)

AC Silva, SG Kim, M Garwood, "Imaging blood flow in brain tumors using arterial spin labeling", *Magn Reson Med*, vol 44, 169–173 (2000)

A.F. Frangi, W.J. Niessen, P.D. Nederkoorn, J. Bakker, W.P.Th.M. Mali, and M.A. Viergever, "Quantitative analysis of vessel morphology from 3D MR angiograms: *in vitro* and *in vivo* results", *Magn. Reson. Med.* 45(2) 311 – 322 (2001).

A. Gabizon, H. Shmeeda, A. T. Horowitz, and S. Zalipsky, "Tumor cell targeting of liposome-entrapped drugs with phospholipid-anchored folic acid-PEG conjugates", *Advanced Drug Delivery Reviews*, 56, 1177–1192 (2004)

A. Gabizon, A.T. Horowitz, D. Goren, D. Tzemach, F. Mandelbaum- Shavit, M. M. Qazen, and S. Zalipsky, "Targeting folate receptor with folate linked to extremities of poly(ethylene glycol)-grafted liposomes: *in vitro* studies", *Bioconjug. Chem.* 10, 289–298 (1999)

A. G. Bell, "On the Production and Reproduction of Sound by Light: the photophone", *Am. J. Sci.* 20, 305-324 (1880)

A. L. Harris, "Antiangiogenesis for cancer therapy", *Lancet*, vol 349 (suppl II), 13-15 (1997)

Allen, T. M., "Ligand-targeted therapeutics in anticancer therapy", *Nat Rev Cancer* 2, 750–763 (2002)

A. Mariampillai, M.K.K. L. M. Jarvi, B.A. Standish, K. Lee, B.C. Wilson, A. Vitkin, and V.X.D. Yang, "Optimized speckle variance OCT imaging of microvasculature," *Opt. Lett.* **35(8)**, 1257-1259 (2010).

A. M. Iga, S. Sarkar, K. M. Sales, M. C. Winslet, and A. M. Seifalian, "Quantitating therapeutic disruption of tumor blood flow with intravital video microscopy," *Cancer Res.* **66(24)**, 11517-11519 (2006).

AM Pabst, M Ackermann, W Wagner, D Haberthür, T Ziebart, MA Konerding, "Imaging angiogenesis: Perspectives and opportunities in tumour research - A method display", *Journal of Cranio-Maxillo-Facial Surgery*, 1-9 (2014)

A.R. Hilgenbrink, and P.S. Low, "Folate receptor-mediated drug targeting: from therapeutics to diagnostics", *J. Pharm. Sci.* 94, 2135–2146 (2005)

A. Quintana, E. Raczka, L. Piehler, I. Lee, A. Myc, I. Majoros, et al., "Design and function of a dendrimer-based therapeutic nanodevice targeted to tumor cells through the folate receptor", *Pharmaceutical Research*, 19, 1310–1316 (2002)

A. Shakeri-Zadeh, et al., “Cancerous cells targeting and destruction using folate conjugated gold nanoparticles”, *Dynamic Biochemistry, (Process Biotechnology and molecular biology 4, (Special Issue I), 6-12 (2010)*

A Taruttis, V Ntziachristos, “Translational Optical Imaging”, *American Journal of Roentgenology*, vol 199, 263–271 (2012)

B. Jun, M. S. Noh, J. Kim, G. Kim, H. Kang, M. Kim, Y. Seo, J. Baek, J. Kim, J. Park, S. Kim, Y. Kim, T. Hyeon, M. Cho, D. H. Jeong, Y. Lee, “Multifunctional Silver-Embedded Magnetic Nanoparticles as SERS Nanoprobes and Their Applications,” *Small*, 6(1), 119–125 (2010).

B. K. Cho, E. J. Roy, T. A. Patrick, and D. M. Kranz, “Single-chain Fv/folate conjugates mediate efficient lysis of folatereceptor- positive tumor cells”, *Bioconjugate Chemistry*, 8, 338– 346 (1997)

B. Mostert, S. Sleijfer, J. A. Foekens, J. W. Gratama, “Circulating tumor cells (CTCs): Detection methods and their clinical relevance in breast cancer”, *Cancer Treatment Reviews*, vol 35 463–474 (2009)

B. P. Negin, S. J. Cohen, “Circulating tumor cells in colorectal cancer: past, present, and future challenges,” *Current Treatment Options in Oncology*, 11 (1-2), 1–13 (2010).

B. Rao, L. Li, K. Maslov, and L. H. Wang, “Hybrid-scanning optical-resolution photoacoustic microscopy for *in vivo* vasculature imaging”, *Opt. Lett.* vol.35, no. 10, 1521- 1523 (2010).

B. Rao, K. Maslov, A. Danielli, R. Chen, K. K. Shung, Q. Zhou, and L. H. V. Wang, “Real-time four-dimensional optical-resolution photoacoustic microscopy with Au nanoparticle-assisted subdiffraction-limit resolution”, *Opt. Lett.* 36(7), 1137-1139 (2011).

B Stella, S Arpicco, MT Peracchia, et al., “Design of folic acid-conjugated nanoparticles for drug targeting”, *J Pharm Sci.* 89: 1452–1464 (2000)

B. Wang et al., “Plasmonic intravascular photoacoustic imaging for detection of macrophages in atherosclerotic plaques”, *Nano Lett.* 9, 2212 (2008).

B. Weigelt, J. L. Peterse, and L. J. van’t Veer, “Breast cancer metastasis: markers and models,” *Nat. Rev. Cancer* 5, 591–602 (2005).

C Alix-Panabie`res, and K Pantel, “Circulating Tumor Cells: Liquid Biopsy of Cancer. *Clinical Chemistry.* 59, 110-118 (2013)

C. K. N. Patel and A. C. Tam, “Pulsed photoacoustic spectroscopy of condensed matter,” *Rev. Mod. Phys.* 53, 517–550 (1981)

C. L. Zavaleta, B. R. Smith, I. Walton, W. Doering, G. Davis, B. Shojaei, M. J. Natan, and S. S. Gambhir, “Multiplexed imaging of surface enhanced Raman scattering nanotags in living mice using noninvasive Raman spectroscopy”, *PNAS* 106 (32), 13511–13516 (2009)

- C. M. OBrien, K. D. Rood, K. Bhattacharyya, T. DeSouza, S. Sengupta, S. K. Gupta, J. D. Mosley, B. S. Goldschmidt, N. Sharma, J. A. Viator, "Capture of circulating tumor cells using photoacoustic flowmetry and two phase flow," *J. of Biomed. Optics*, 17, 061221 (2012).
- C. P. Leamon, J. A. Reddy, I. R. Vlahov, E. Westrick, A. Dawson, R. Dorton, et al., "Preclinical antitumor activity of a novel folate-targeted dual drug conjugate", *Molecular Pharmaceutics*, 4, 659–667 (2007)
- C. P. Leamon, J. A. Reddy, I. R. Vlahov, M. Vetzal, N. Parker, J. S. Nicoson, et al., "Synthesis and biological evaluation of EC72: a new folate-targeted chemotherapeutic", *Bioconjugate Chemistry*, 16, 803–811 (2005)
- C. P. Leamon and P. S. Low, "Cytotoxicity of momordin– folate conjugates in cultured human cells", *Journal of Biological Chemistry*, 267, 24966–24971. (1992).
- C. P., Leamon, and P. S., "LowFolate-mediated targeting: from diagnostics to drug and gene delivery", *Drug Discovery Today*, 6, 44–51 (2001)
- C. Leamon, and P.S. Low, "Membrane folate-binding proteins are responsible for folate-protein conjugate endocytosis into cultured cells", *Biochem. J.* 291, 855–860 (1993)
- C. Li, "A targeted approach to cancerimaging and therapy", *Nature Materials*, vol 13, 110-115 (2014)
- C. L. Zavaleta, B. R. Smith, I. Walton, W. Doering, G. Davis, B. Shojaei, M. J. Natan and S. S. Gambhir, "Multiplexed imaging of surface enhanced Raman scattering nanotags in living mice using noninvasive Raman spectroscopy," *PNAS* 106 (32), 13511–13516 (2009)
- C. Kim et al., "*In vivo* Molecular Photoacoustic Tomography of Melanomas Targeted by Bioconjugated Gold Nanocages", *ACS Nano* 4, 4559 (2010).
- C. P. Favazza, O. Jassim, L. A. Cornelius, L. V. Wang, "*In vivo* photoacoustic microscopy of human cutaneous microvasculature and a nevus", *J. Biomed. Opt.* 16, 016015 (2011).
- CR Crawford and KF King, "Computed tomography scanning with simultaneous patient translation", *Med Phys* 17(6), 967–982 (1990)
- C. Wei, J. Xia, I. Pelivanov, X. Hu, X. Gao, M. O'Donnell, "Trapping and dynamic manipulation of polystyrene beads mimicking circulating tumor cells using targeted magnetic/ photoacoustic contrast agents," *J. Biomed. Optics* 17(10), 101517(2012)
- C. Yeh, S. Hu, K. Maslov and L. V. Wang, "Photoacoustic microscopy of blood pulse wave," *J. Biomed. Opt.* 17(7), 070504 (2012)
- D. C. Danila, M. Fleisher, H. I. Scher, "Circulating tumor cells as biomarkers in prostate cancer," *Clin. Cancer Res.*, 17 (12), 3903–3912 (2011).

- D. F. Hayes, et al., “Circulating tumor cells at each follow-up time point during therapy of metastatic breast cancer patients predict progression-free and overall survival”, *Clin. Cancer Res.* 12, 4218–4224 (2006).
- D. Marrinucci, K. Bethel, R.H. Bruce, D.N. Curry, B. Hsieh, M. Humphrey, R.T. Krivacic, J. Kroener, L. Kroener, A. Ladanyi, et al., “Case study of the morphologic variation of circulating tumor cells. *Hum. Pathol.* 38, 514–519 (2007)
- D. Pan, J.L. Turner, and K.L. Wooley, “Folic acid-conjugated nanostructured materials designed for cancer cell targeting”, *Chem. Commun. (Camb.)* 7, 2400–2401 (2003)
- D Shweiki, A Itin, D Softer, E Keshet, “Vascular endothelial growth factor induced by hypoxia may mediate hypoxia-initiated angiogenesis”, *Nature* 359, 843-845 (1992)
- EB Brown, RB Campbell, Y Tsuzuki, L Xu, P Carmeliet, D Fukumura, et al., “*In vivo* measurement of gene expression, angiogenesis and physiological function in tumours using multiphoton laser scanning microscopy”, *Nat Med* 7, 864-868 (2001)
- E. Gormally, E. Caboux, P. Vineis, and P. Hainaut, “Circulating free DNA in plasma or serum as biomarker of carcinogenesis: practical aspects and biological significance”, *Mutat. Res.* 635, 105–117 (2007)
- E.I. Galanzha, E.V. Shashkov, P.M. Spring, J.Y. Suen, and V.P. Zharov, “*In vivo*, noninvasive, label-free detection and eradication of circulating metastatic melanoma cells using wo-color photoacoustic flow cytometry with a diode laser”, *Cancer Res.* 69, 7926–7934 (2009)
- E.I. Galanzha, E.V. Shashkov, T. Kelly, J.W. Kim, L. Yang, and V.P. Zharov, “*In vivo* magnetic enrichment and multiplex photoacoustic detection of circulating tumour cells”, *Nat. Nanotechnol.* 4, 855–860 (2009)
- E.I. Galanzha, E.V. Shashkov, P.M. Spring, J.Y. Suen, and V.P. Zharov. “*In vivo*, noninvasive, label-free detection and eradication of circulating metastatic melanoma cells using two-color photoacoustic flow cytometry with a diode laser”, *Cancer Res.*, vol 69, 7926–7934 (2009)
- E. I. Sega, and P. S. Low, “Tumor detection using folate receptor-targeted imaging agents”, *Cancer Metastasis Rev* 27, 655–664 (2008)
- E.J. Battegay, “Angiogenesis: mechanistic insights, neovascular diseases and therapeutic prospects”, *J Mol Med*, vol 73, 333-346 (1995)
- EJ Hannen, JA Van Der Laak, JJ Manni, HP Freihofer, PJ Slootweg, R Koole, PC de Wilde, “Computer assisted analysis of the microvasculature in metastasised and nonmetastasised squamous cell carcinoma of the tongue”, *Head Neck*, vol 24, 643-650 (2002)
- E.J. Roy, U. Gawlick, B. A. Orr, and D. M. Kranz, “Folate-mediated targeting of T cells to tumors”, *Advanced Drug Delivery Reviews*, 56, 1219–1231 (2004)

EM Rohren, TG Turkington, RE Coleman, “Clinical applications of PET in oncology”, *Radiology*, vol 231, 305 – 32 (2004)

E. Papadopoulou, E. Davilas, V. Sotiriou, E. Georgakopoulos, S. Georgakopoulou, A. Koliopanos, F. Aggelakis, K. Dardoufas, N.J. Agnanti, I. Karydas, and G. Nasioulas, “Cell-free DNA and RNA in plasma as a new molecular marker for prostate and breast cancer”, *Ann. NY Acad. Sci.* 1075, 235– 243 (2006)

E. Soeth, et al., “Detection of tumor cell dissemination in pancreatic ductal carcinoma patients by CK 20 RT-PCR indicates poor survival”, *J. Cancer Res. Clin. Oncol.* 131, 669–676 (2005)

E. Zhang, J. Laufer, and P. Beard, “Backward-mode multiwavelength photoacoustic scanner using a planar Fabry-Perot polymer film ultrasound sensor for high-resolution three-dimensional imaging of biological tissues”, *Applied Optics* 47, 561(2008)

E. Zhang, and P. Beard, “Ultra high sensitivity, wideband Fabry Perot ultrasound sensors as an alternative to piezoelectric PVDF transducers for biomedical photoacoustic detection”, *Proc. SPIE* 5320, 222-229 (2004)

E. Z. Zhang et al., “Multimodal photoacoustic and optical coherence tomography scanner using an all optical detection scheme for 3D morphological skin imaging”, *Biomed. Opt. Express* 2, 2202 (2011)

F. A. Duck, *Physical Properties of Tissue* (Academic, London, 1990)

F Kiessling, M Krix, M Heilmann, S Vosseler, M Lichy, C Fink, et al., “Comparing dynamic parameters of tumor vascularization in nude mice revealed by magnetic resonance imaging and contrast-enhanced intermittent power Doppler sonography”, *Invest Radiol*, vol 38, 516 – 524 (2003)

F. Tanaka, K. Yoneda, N. Kondo, M. Hashimoto, T. Takuwa, S. Matsumoto, Y. Okumura, S. Rahman, N. Tsubota, T. Tsujimura, K. Kuribayashi, K. Fukuoka, T. Nakano, S. Hasegawa, “Circulating tumor cell as a diagnostic marker in primary lung cancer,” *Clin. Cancer Res.*, 15 (22): 6980–6986 (2009)

F. Wolfrum, I. Vogel, F. Fandrich, and H. Kalthoff, “Detection and clinical implications of minimal residual disease in gastro-intestinal cancer”, *Langenbecks Arch. Surg.* 390, 430–441 (2005)

G Ascani, P Balercia, M Messi, L Lupi, G Goteri, A Filosa, et al., “Angiogenesis in oral squamous cell carcinoma”, *Acta Otorhinolaryngol Ital*, vol 25, 13-17 (2005)

G. Attard, J.F. Swennenhuis, D. Olmos, A.H. Reid, E. Vickers, R. A’Hern, R. Levink, F. Coumans, J. Moreira, R. Riisnaes, et al., “Characterization of ERG, AR and PTEN gene status in circulating tumor cells from patients with castration-resistant prostate cancer”, *Cancer Res.* 69, 2912– 2918 (2009)

- G. Destito, R. Yeh, C. S. Rae, M.G. Finn, and M. Manchester, “Folic Acid-Mediated Targeting of Cowpea Mosaic Virus Particles to Tumor Cells”, *Chemistry & Biology* 14, 1152–1162 (2007)
- GD Rubin, AJ Schmidt, LJ Logan, et al., “Multidetector-row CT angiography of lower extremity occlusive disease: a new application for CT scanning”, *Radiology* 210(P), 588 (1999)
- GD. Rubin, J Leipsic, UJ Schoepf, D Fleischmann, S Napel, “CT Angiography after 20 Years: A Transformation in Cardiovascular Disease Characterization Continues to Advance”, *Radiology*, vol 271, 633-652 (2014)
- GD Rubin, MC Shiau, AN Leung, ST Kee, LJ Logan, MC Sofilos, “Aorta and iliac arteries: single versus multiple detector-row helical CT angiography”, *Radiology* 215(3), 670–676 (2000)
- G Gasparini, M Toi, M Gion, et al., “Prognostic significance of vascular endothelial growth factor protein in node-negative breast carcinoma”, *J Natl Cancer Inst*, vol 89, 139–147 (1997)
- G. Liu, W. Jia, V. Sun, B. Choi, and Z. Chen, “High-resolution imaging of microvasculature in human skin in-vivo with optical coherence tomography,” *Opt. Express* **20(7)**, 7694-7705 (2012).
- G. Ku and L.H., V. Wang, “Deeply penetrating photoacoustic tomography in biological tissues enhanced with an optical contrast agent”, *Optics Letters* 30 (5), 507-509 (2005).
- G. Ku and L. V. Wang, “Scanning thermoacoustic tomography in biological tissue”, *Med. Phys.* 27, 1195-1202 (2000)
- G. Ku, X. Wang, G. Stoica, and L.-H. Wang, “Multiple-Bandwidth Photoacoustic Tomography”, *Phys. Med. Biol.*, vol 49, 1329-1338 (2004)
- G. Ku, X. Wang, X. Xie, G. Stoica, and L.-H. Wang, “Imaging of tumor angiogenesis in rat brains *in vivo* by photoacoustic tomography”, *Appl. Opt.*, vol 44, 770-775 (2005)
- G. Niu, X. Chen, “PET imaging of angiogenesis”, *PET Clin*, vol 4, 17–38 (2009)
- G. P. Gupta¹ and J. Massagué, “Cancer Metastasis: Building a Framework”, *Cell* 127, 679-695 (2006)
- G Vassaux, T Groot-Wassink, “*In vivo* noninvasive imaging for gene therapy”, *J Biomed Biotechnol*, vol 2003, 92–101 (2003)
- H.F. Zhang, K. Maslov, G. Stoica, and L. H., V. Wang, “Functional photoacoustic microscopy for high-resolution and noninvasive *in vivo* imaging”, *Nature Biotechnology* 24, 848-851 (2006)
- HMW Verheul, EE Voest, and RO Schlingemann, “Are tumors angiogenesis-dependent”, *J Pathol* 202, 5–13 (2004)

- H. Schwarzenbach, C. Alix-Panabières, I. Müller, N. Letang, J.P. Vendrell, X. Rebillard, and K. Pantel, “Cell-free tumor DNA in blood plasma as a marker for circulating tumor cells in prostate cancer”, *Clin. Cancer Res.* 15, 1032–1038 (2009)
- H. Schwarzenbach, D.S.Hoon, and K. Pantel, “Cell-free nucleic acids as biomarkers in cancer patients”, *Nat. Rev. Cancer* 11, 426–437 (2011)
- H. Schwarzenbach, F.K. Chun, I. Lange, S. Carpenter, M. Gottberg, A. Erbersdobler, M.G. Friedrich, H. Huland, and K. Pantel, “Detection of tumor-specific DNA in blood and bone marrow plasma from patients with prostate cancer”, *Int. J. Cancer.* 120, 1465–1471 (2007)
- IARC, “Globocan 2012: Estimated Cancer Incidence, Mortality and Prevalence Worldwide in 2012,” http://globocan.iarc.fr/Pages/fact_sheets_cancer.aspx (accessed May 8, 2014)
- I. V. Larina, K. V. Larin and R. O. Esenaliev, “Real-time optoacoustic monitoring of temperature in tissues”, *J. Phys. D: Appl. Phys.* 38, 2633–2639 (2005)
- J.A. Aguirre-Ghiso, “Models, mechanisms and clinical evidence for cancer dormancy”, *Nat. Rev. Cancer*, vol 7, 834–846 (2007)
- J. A. Reddy, and P. S. Low, “Enhanced folate receptor mediated gene therapy using a novel pH-sensitive lipid formulation”, *Journal of Controlled Release*, 64, 27–37 (2000)
- J.A. Reddy, and P.A. Low, “Folate-mediated targeting of therapeutic and imaging agents to cancers”, *Crit. Rev. Ther. Drug Carrier Syst.* 15, 587–627 (1998)
- J. A. Reddy, R. Dorton, E. Westrick, A. Dawson, T. Smith, L. C. Xu, et al., “Preclinical evaluation of EC145, a folate– vinca alkaloid conjugate”, *Cancer Research*, 67, 4434–4442 (2007)
- J. B. Pawley, *Handbook of Biological Confocal Microscopy*, 3rd ed. Springer Science + Business Media, LLC, New York (2006).
- J. C. Miller , H. H. Pien , D. Sahani , A. G. Sorensen, J. H. Thrall, “Imaging Angiogenesis Applications and Potential for Drug Development”, *Journal of the National Cancer Institute*, vol 97, 172 (2005)
- J. C. Ranasinghesagara, Y. Jian, X. H. Chen, K. Mathewson, and R. J. Zemp, “Photoacoustic technique for assessing optical scattering properties of turbid media,” *J. Biomed. Opt.* 14(4), 040504 (2009).
- J. F. Ross, P. K. Chaudhuri, and M. Ratnam, “Differential regulation of folate receptor isoforms in normal and malignant tissues *in vivo* and in established cell lines”, *Physiologic and clinical implications. Cancer* 73, 2432–2443 (1994)
- J. Folkman, “Tumor Angiogenesis”, *Advan. Cancer Res.*, vol 19, 331- 357 (1974)
- J Folkman, Y Shing, “Angiogenesis”, *J Biol Chem*, vol 267, 10931 – 10934 (1992)

- JM. Provenzale, "Imaging of angiogenesis clinical techniques and novel imaging methods", American Journal of Roentgenology, vol 188, 11-23 (2007)
- J.-M. Yang et al., "Photoacoustic endoscopy", Opt. Lett. 34, 1591 (2009).
- J.-M. Yang et al., "Toward dual-wavelength functional photoacoustic endoscopy: laser and peripheral optical systems development", Proc. SPIE 8223, 822316 (2012).
- J Rak, J Filmus, RS Kerbel, "Reciprocal paracrine interactions between tumour cells and endothelial cells: the "angiogenesis progression" hypothesis", Eur J Cancer 32A, 2438-2450 (1996)
- J. Rao, A. Dragulescu-Andrasi, H. Yao, "Fluorescence imaging *in vivo*: recent advances", Curr Opin Biotechnol. 18, 17-25 (2007)
- J. Rao, A. Dragulescu-Andrasi, H. Yao, "Fluorescence imaging *in vivo*: recent advances", Curr Opin Biotechnol. 18, 17-25 (2007)
- J Rebol, "The vascularisation of oral cavity tumours and tumour shell tissue determined by three-dimensional power Doppler sonography", Ultrasound Med Biol 33, 493-499 (2007)
- J Rebol, B Brkljaci, Z Bumber, S Psenicnik, P Povalej, "3D power Doppler analysis of the vascularisation in tumours of the oral cavity", Ultraschall Med, vol 28, 40-44 (2007)
- J. Shah, S. Park, S. Aglyamov, T. Larson, L. Ma, K. Sokolov, K. Johnston, S. Y. Emelianov, "Photoacoustic imaging and temperature measurement for photothermal cancer therapy", J Biomed Opt. 13(3), 034024 (2008)
- J. Yao, C. H. Huang, L. Wang, J. M. Yang, L. Gao, K. I. Maslov, J. Zou and L. V. Wang, "Wide-field fast-scanning photoacoustic microscopy based on a water-immersible MEMS scanning mirror", J. Biomed. Opt. 17(8), 080505 (2012)
- J. Yao, K. Maslov, Y. Shi, L. Taber, and L. V. Wang, "*In vivo* photoacoustic imaging of transverse blood flow using Doppler broadening of bandwidth," Opt. Lett. 35, 1419–1421 (2010)
- J. Yao and L. V. Wang, "Photoacoustic tomography fundamentals, advances and prospects", Contrast Media Mol. Imaging 6, 332 - 345 (2011)
- J. Y. Lu, D. A. Lowe, M. D. Kennedy, and P. S. Low, "Folate-targeted enzyme prodrug cancer therapy utilizing penicillin- V amidase and a doxorubicin prodrug", Journal of Drug Targeting, 7, 43–53 (1999)
- KA Miles, BB Kelley, "CT measurements of capillary permeability within nodal masses: a potential technique for assessing the activity of lymphoma", Br J Radio1, vol 70, 74-79 (1997)
- K.A. Yoon, S. Park, S.H. Lee, J.H. Kim, and J.S. Lee, "Comparison of circulating plasma DNA levels between lung cancer patients and healthy controls", J. Mol. Diagn. 11, 182–185 (2009)

- K.B. Hartman, L.J. Wilson, M.G. Rosenblum, “Detecting and treating cancer with nanotechnology”, *Mol Diagn Ther.* 12(1), 1-14(2008)
- K. E. Anderson, L. A. Eliot, B. R. Stevenson, and J. A. Rogers, “Formulation and evaluation of a folic acid receptor targeted oral vancomycin liposomal dosage form”, *Pharmaceutical Research*, 18, 316–322 (2001)
- KH Plate, G Breier, B Millauer, A Ullrich, W Risau, “Up-regulation of vascular endothelial growth factor and its cognate receptors in a rat glioma model of tumor angiogenesis”, *Cancer Res.*, vol 53, 5822-5827 (1993)
- K. Jansen, A. F. W. van der Steen, H. M. M. van Beusekom, J. W. Oosterhuis, G. van Soest, “Intravascular photoacoustic imaging of human coronary atherosclerosis”, *Opt. Lett.* 36, 597 (2011).
- K.K. Jain, “Nanomedicine: application of nanobiotechnology in medical practice”, *Med Princ Pract.* 17(2), 89-101 (2008)
- K.K. Jain, “Recent advances in nanooncology”, *Technol Cancer Res Treat.* 7(1), 1-13 (2008)
- K. Kazunori, Y. Y. Huang, N. Lane, M. Huebschman, J. W. Uhr, E. P. Frenkel, X. Zhang, “Microchip-based immunomagnetic detection of circulating tumor cells,” *Lab on a Chip*, 11 (20), 3449–3457 (2011).
- K. Maslov, G. Stoica, and L.V. Wang, “*In vivo* dark-field reflection-mode photoacoustic microscopy”, *Opt. Lett.* 30, 625–627 (2005)
- K. Maslov, H. F. Zhang, S. Hu and L. H., V., Wang, “Optical-resolution photoacoustic microscopy for *in vivo* imaging of single capillaries”, *Opt. Lett.* 33, 929-931 (2008)
- K. Pachmann, J.H. Clement, C.P. Schneider, B. Willen, O. Camara, U. Pachmann, and K. Höffken, “Standardized quantification of circulating peripheral tumor cells from lung and breast cancer”, *Clin. Chem. Lab. Med.* 43, 617–627 (2005)
- K. Pantel and R.H. Brakenhoff, “Dissecting the metastatic cascade”, *Nat. Rev. Cancer*, vol 4, 448–456 (2004)
- K. Pantel, R. H. Brakenhoff, and B. Brandt, “Detection, clinical relevance and specific biological properties of disseminating tumour cells”, *Nat Rev Cancer*, vol 8, 329-40 (2008)
- Laser Institute of America, American National Standard for Safe Use of Lasers ANSI Z136.1-2007 (American National Standards Institute, Inc. 2007).
- L. Harris, H. Fritsche, R. Mennel, et al., “American Society of Clinical Oncology 2007 Update of Recommendations for the Use of Tumor Markers in Breast Cancer”, *Journal of Clinical Oncology*, vol 25, 5287-5312 (2007)

- L. Holmgren, MS O'Reilly, J. Folkman, "Dormancy of micrometastases: balanced proliferation and apoptosis in the presence of angiogenesis suppression", *Nat Med*, vol 1, 149-153 (1995)
- L. Li, R. J. Zemp, G. Lungu, G. Stoica, and L. H. V. Wang, "Photoacoustic imaging of lacZ gene expression *in vivo*", *Journal of Biomedical Optics* 12, 020504(2007). [1] L.V. Wang, *Photoacoustic Imaging and Spectroscopy* (CRC, 2009)
- L. Pan, I. Utkin, and R. Fedosejevs, "Passively Q-switched ytterbium-doped double-clad fiber laser with a Cr⁴⁺: YAG saturable absorber", *IEEE Photonics Technology Letters* 19, 1979 (2007).
- L. Pan, I. Utkin, R.J. Lan, Y. Godwal, and R. Fedosejevs, "High peak power sub-nanosecond passively Q-switched ytterbium doped fiber laser", *Opt. Lett.*, 35 (7) 895 (2010).
- L. Pan, I. Utkin, and R. Fedosejevs, "Two-wavelength passively Q-switched ytterbium doped fiber laser", *Optics Express* 16, 11858 (2008).
- L. Song, K. Maslov, and L. V. Wang, "Multifocal optical-resolution photoacoustic microscopy *in vivo*," *Opt. Lett* 36, 1236-1237 (2011).
- L. V. Wang and H. Wu, *Biomedical Optics: Principles and Imaging* (John Wiley & Sons, Inc., Hoboken, 2007)
- L. V. Wang and S. Hu, "Photoacoustic tomography *in vivo* imaging from organelles to organs", *Science* 335, 1458 (2012);
- L.V. Wang, K. Maslov, J. Yao, B. Rao, and L. H., V. Wang, "Fast voice-coil scanning optical-resolution photoacoustic microscopy", *Opt. Lett.* 36, 139-141 (2011).
- L. Wan, K. Pantel, and Y. Kang, "Tumor metastasis moving new biological insights into the clinic", *Nature Medicine*, vol 19, 1450-1464 (2013)
- L. Xu, K. F. Pirollo, W. H. Tang, A. Rait, and E. H. Chang, "Transferrin-liposome-mediated systemic p53 gene therapy in combination with radiation results in regression of human head and neck cancer xenografts", *Human Gene Therapy*, 10, 2941– 2952 (1999)
- MA Bogdan, MB Klein, GD Rubin, TR McAdams, J Chang, "CT angiography in complex upper extremity reconstruction", *J Hand Surg*, 29(5), 465–469 (2004)
- MB Lowry, AM Duchemin, JM, Robinson, and CL Anderson, "Functional separation of pseudopod extension and particle internalization during Fc gamma receptor-mediated phagocytosis", *J Exp Med.* 187, 161–176 (1998)
- M. C. Miller, G. V. Doyle, L. W. Terstappen, "Significance of Circulating Tumor Cells Detected by the CellSearch System in Patients with Metastatic Breast Colorectal and Prostate Cancer", *J. of oncology*, vol. 2010, 617421, 8 pages, (2010)

M. Cristofanilli, G.T. Budd, M.J. Ellis, A. Stopeck, et al., et al., “Circulating tumor cells, disease progression, and survival in metastatic breast cancer”, *N. Engl. J. Med.* 351, 781–791 (2004).

M. Fleischmann, P. J. Hendra, A. J. McQuiUan, “Raman spectra of pyridine adsorbed at a silver electrode”, *Chew. Phys. Lett.* 26 (2), 163-166 (1974)

M.-H. Xu and L.-H. V. Wang, “Photoacoustic imaging in biomedicine”, *Rev. Sci. Instr.* 77, 041101 (2006)

M. Ignatiadis, et al., “Different prognostic value of cytokeratin-19 mRNA positive circulating tumor cells according to estrogen receptor and HER2 status in early-stage breast cancer”, *J. Clin. Oncol.* 25, 5194–5202 (2007)

MK Brawer, RE Deering, M Brown, SD Preston, SA Bigler, “Predictors of pathologic stage in prostatic carcinoma”, *Cancer* 73, 678-687 (1994)

M. K. Hossain and Y. Ozaki, “Surface-enhanced Raman scattering: facts and inline trends”, *Current Science* 2, 192-201 (2009)

M.O. Oyewumi, R.A. Yokel, M. Jay, T. Coakley, and R.J. Mumper, “Comparison of cell uptake, biodistribution and tumor retention of folate-coated and PEG-coated gadolinium nanoparticles in tumor-bearing mice”, *J. Control. Release* 95, 613–626 (2004)

M Rudin, PMJ McSheehy, PR Allegrini, M Rausch, D Baumann, M Becquet, et al., “PTK787/ZK222584, a tyrosine kinase inhibitor of vascular endothelial growth factor receptor, reduces uptake of the contrast agent GdDOTA by murine orthotopic B16/Bl6 melanoma tumours and inhibits their growth *in vivo*”, *NMR Biomed*, vol 18, 308-321 (2005)

MS Pearce, JA Salotti, MP Little, et al., “Radiation exposure from CT scans in childhood and subsequent risk of leukaemia and brain tumours: a retrospective cohort study”, *Lancet* 380 (9840), 499–505 (2012)

M. Yu, S. Stott, M. Toner, S. Maheswaran, and D. A. Haber, “Circulating tumor cells: approaches to isolation and characterization”, *J. Cell Biol.*, vol. 192, 373–382 (2011)

N Lassau, C Paturel-Assehn, JM Guinebretiere, et al., “New hemodynamic approach to angiogenesis: color and pulsed Doppler ultrasonography”, *Invest Radio*1, vol 34, 194-198 (1999)

N McKenna, “*In vivo* imaging shines”, *Genetic Engineering & Biotechnology News*, vol 34, 28-30 (2014)

N. Nishida, H. Yano, T. Nishida, T. Kamura, M. Kojiro, “Angiogenesis in cancer”, *Vascular Health and Risk Management*, vol 2(3), 213–219 (2006)

N. Weidner, “Tumoural vascularity as a prognostic factor in cancer patients: the evidence continues to grow”, *J Pathol*, vol 184, 119–122 (1998)

- N Weidner, J Folkman, F Pozza, et al., “Tumor angiogenesis: a new significant and independent prognostic indicator in early-stage breast carcinoma”, *J Natl Cancer Inst*, vol 84, 1875–1887 (1992)
- P. Beard, “Biomedical photoacoustic imaging”, *Interface Focus*, 1, 602-631 (2011)
- P Carmeliet, RK Jain, “Angiogenesis in cancer and other diseases”, *Nature* vol 407, 249–257 (2000)
- P. Carmeliet and R. K. Jain, “Molecular mechanisms and clinical applications of angiogenesis nature”, *Nature*, vol 473, 298 (2011)
- P. Fortina, L.J. Kricka, S. Surrey, P. Grodzinski, “Nanobiotechnology: the promise and reality of new approaches to molecular recognition”, *Trends Biotechnol.* 23 (4), 168-173(2005)
- P. Friedl, and K. Wolf, “Tumour-cell invasion and migration: diversity and escape mechanisms”, *Nat. Rev. Cancer* 3, 362–374 (2003)
- P. Hajireza, W. Shi and R. J. Zemp, “Label-Free *In vivo* GRIN-Lens optical resolution photoacoustic micro-endoscopy”, *Laser Phys. Lett.* 10 055603 (2013).
- P. Hajireza, W. Shi, P. Shao, S. Kerr, and R.J. Zemp, “Optical-resolution photoacoustic micro-endoscopy using image-guide fibers and fiber laser technology”, *Proc. SPIE* 78990P (2011)
- P. Li, C. C. Wang, D. Shieh, C. Wei, C. Liao, C. Poe, S. Jhan, A. Ding and Y. Wu, “*In vivo* Photoacoustic Molecular Imaging with Simultaneous Multiple Selective Targeting Using Antibody-Conjugated Gold Nanorods”, *Opt. Express* 23 (16), 18605-18615 (2008)
- P Macchiarini, G Fontanini, MJ Hardin, F Squartini, CA Angeletti, “Relation of neovascularization to metastasis of non-small-cell lung cancer”, *Lancet* 340, 145- 146 (1992)
- P. N. T. Wells, “Ultrasonic imaging of the human body”, *Rep. Prog. Phys.* 62, 671 (1999).
- P. Quaresma, I. Os´orio, G. D´oria, P. A. Carvalho, A. Pereira, J. Langer, J. P. Ara´ujo, e I. Pastoriza-Santos, L. M. Liz-Marz´an, R. Franco, P. V. Baptistac, E. Pereira, “Star-shaped magnetite@gold nanoparticles for protein magnetic separation and SERS detection,” *RSC Adv.*, 4, 3659-3667 (2013).
- P. Shao, W. Shi, R. K. Chee, and R. J. Zemp, “Mosaicing acquisition and processing for optical resolution photoacoustic microscopy,” *J. Biomed. Opt.* **17(8)**, 080503 (2012).
- P. S. Low, and A. C. Antony, “Folate receptor-targeted drugs for cancer and inflammatory disease”, *Adv Drug Deliv Rev* 56, 1055–1058 (2004)
- P. Wülfing, J. Borchard, H. Buerger, S. Heidl, K.S. Zänker, L. Kiesel, and B. Brandt, “HER2-positive circulating tumor cells indicate poor clinical outcome in stage I to III breast cancer patients”, *Clin. Cancer Res.* 12, 1715–1720 (2006)

- P. Z. McVeigh, R. J. Mallia, I. Veilleux, and B. C. Wilsona, “Widefield quantitative multiplex surface enhanced Raman scattering imaging *in vivo*,” *J. Biomed. Opt.*, 18(4), 046011 (2013)
- Q Zhu, N Chen, SH Kurtzman, “Imaging tumor angiogenesis by use of combined near-infrared diffusive light and ultrasound”, *Opt Lett* 28, 337–339 (2003)
- R Abramovitch, D Frenkiel, M Neeman, “Analysis of subcutaneous angiogenesis by gradient echo magnetic resonance imaging”, *Magn Reson Med*, vol 39, 813-824 (1998)
- R. A. Ghossein, S. Bhattacharya, J. Rosai, “Molecular detection of micrometastases and circulating tumor cells in solid tumors,” *Clin. Cancer Res.* 5, 1950–1960 (1999).
- R. C. Brasch, K. C. P. Li, et al., “*In vivo* monitoring of tumor angiogenesis with MRI”, *Acad Radiol*, vol 7, 812-823 (2000)
- R. F. Swaby, M. Cristofanilli, “Circulating tumor cells in breast cancer: a tool whose time has come of age,” *BMC medicine* 9, 43 (2011).
- R. Gangnus, , S. Langer, E. Breit, K. Pantel, and M.R. Speicher, “Genomic profiling of viable and proliferative micrometastatic cells from early-stage breast cancer patients”, *Clin. Cancer Res.* 10, 3457–3464 (2004).
- R. Gertler, R. Rosenberg, K. Fuehrer, M. Dahm, H. Nekarda, and J.R. Siewert, “Detection of circulating tumor cells in blood using an optimized density gradient centrifugation”, *Recent Results Cancer Res.* 162, 149–155 (2003)
- R.J. Zemp, L. Song, R. Bitton, K.K Shung, and L.V. Wang, “*In vivo* realtime photoacoustic microscopy with a 30-MHz ultrasound array transducer”, *Optics Express* 16 (11), 7915 (2008)
- R.M. Weight, P.S. Dale, and J.A. Viator, “Detection of circulating melanoma cells in human blood using photoacoustic flowmetry”, *Conf. Proc. IEEE Eng. Med. Biol. Soc.* 2009, 106–109 (2009)
- RO Schlingemann, FJ Rietveld, RM de Waa, et al., “Leukocyte antigen CD34 is expressed by a subset of cultured endothelial cells and on endothelial abluminal microprocesses in the tumor stroma”, *Lab Invest*, vol 62, 690–696 (1990)
- RO Schlingemann, FJ Rietveld, RM deWaal, S Ferrone, DJ Ruiten, “Expression of the high molecular weight melanoma-associated antigen by pericytes during angiogenesis in tumors and in healing wounds”, *Am J Pathol*, vol 136, 1393–1405 (1990)
- R. S. C. Cobbold, *Foundations of Biomedical Ultrasound* (Oxford University Press, Inc., New York, 2007)
- R.T. Krivacic, A. Ladanyi, D.N. Curry, H.B. Hsieh, P. Kuhn, D.E. Bergsrud, J.F. Kepros, T. Barbera, M.Y. Ho, L.B. Chen, et al., “A rare-cell detector for cancer”, *Proc. Natl. Acad. Sci. USA.* 101, 10501–10504 (2004)

- S.A. Ermilov, T. Khamapirad, A. Conjusteau, M.H. Leonard, and R. Laceywell, “Laser optoacoustic imaging system for detection of breast cancer”, *Journal of Biomedical Optics* 14(2), 24007 (2009)
- S. D. Weitman, R. H. Lark, L. R. Coney, D. W. Fort, V. Frasca, V. R. Zurawski, and B. A. Kamen, “Distribution of the folate receptor GP38 in normal and malignant cell lines and tissues”, *Cancer Res* 52, 3396–3401 (1992)
- S. F. Atkinson, T. Bettinger, L. W. Seymour, J. P. Behr, and C. M. Ward, “Conjugation of folate via gelonin carbohydrate residues retains ribosomal-inactivating properties of the toxin and permits targeting to folate receptor positive cells”, *Journal of Biological Chemistry*, 276, 27930–27935 (2001)
- S. Hu, B. Rao, K. Maslov, L. V. Wang, “Label-free photoacoustic ophthalmic angiography”, *Opt. Lett.* 35, 1 (2010).
- S. Hu, J. Yao, K. Maslov, and L. H., V. Wang, “Optical-resolution photoacoustic microscopy of angiogenesis in a transgenic mouse model”, *Proc. SPIE* 7564, 756406 (2010).
- S. Hu, K. Maslov, and L. V. Wang, “*In vivo* functional chronic imaging of a small animal model using optical-resolution photoacoustic microscopy,” *Med. Phys.* 36, 2320–2323 (2009).
- S. Hu, K. Maslov, and L. V. Wang, “Noninvasive label-free imaging of microhemodynamics by optical-resolution photoacoustic microscopy,” *Opt. Express* 17, 7688–7693 (2009)
- S. Hu, K. Maslov, and L. V. Wang, “Second-generation optical-resolution photoacoustic microscopy with improved sensitivity and speed”, *Opt. Lett.*, vol 16, 1134 (2011)
- S. Hu, K. Maslov, V. Tsytarev, and L. V. Wang, “Functional transcranial brain imaging by optical-resolution photoacoustic microscopy,” *J. Biomed. Opt.* 14, 040503 (2009)
- S. Hu, L. V. Wang, “Neurovascular photoacoustic tomography”, *Front. Neuroenerg.* 2, (2010).
- S. Hu, P. Yan, K. Maslov, J. M. Lee, and L. H. V. Wang, “Intravital imaging of amyloid plaques in a transgenic mouse model using optical-resolution photoacoustic microscopy,” *Opt. Lett.* 34 (24), 3899-3901 (2009)
- S. Hu, P. Yan, K. Maslov, J.M. Lee, and L. H., V. Wang, “Optical-resolution photoacoustic microscopy of amyloid- β deposits *in vivo*”, *Proc. SPIE* 7564, 75643D (2010).
- S Hu, LV.Wang, “Photoacoustic imaging and characterization of the microvasculature”, *J Biomed Opt* 15(1), 011101 (2010)
- SI Hajdu, MJ Thun, LM Hannan, A Jemal, “A note from history: landmarks in history of cancer, part 1”, *Cancer* 117 (5), 1097–102. (2011)

- S. Jiao et al., “Photoacoustic ophthalmoscopy for *in vivo* retinal imaging”, *Opt. Express* 18, 3967 (2010).
- S. Lin, X. Xie, M.R. Patel, Y.H. Yang, Z. Lin, F. Cao, O. Gheysens, Y. Zhang, S.S. Gambhir, J.H. Rao, and J.C. Wu, “Quantum dot imaging for embryonic stem cells”, *BMC Biotechnol.* 7, 67 (2007)
- S. Keren, C. Zavaleta, Z. Cheng, A. de la Zerda, O. Gheysens, and S. S. Gambhir, “Noninvasive molecular imaging of small living subjects using Raman spectroscopy,” *Proc Natl Acad Sci USA.* 105, 5844-5849 (2008)
- S. Lin, X. Xie, M.R. Patel., Y.H. Yang, Z. Lin, F. Cao, O. Gheysens, Y. Zhang, S.S. Gambhir, J.H. Rao and J.C. Wu, “Quantum dot imaging for embryonic stem cells”, *BMC Biotechnol.* 7, 67 (2007)
- S.M. Stephenson, P.S. Low, and R.J. Lee, “Folate receptor- mediated targeting of liposomal drugs to cancer cells”, *Methods Enzymol.* 387, 33–50 (2004)
- S. Nagrath, L. V. Sequist, S. Maheswaran, D. W. Bell, D. Irimia¹, L. Ulkus, M. R. Smith, E. L. Kwak, S. Digumarthy, A. Muzikansky, P. Ryan, U. J. Balis, R. G. Tompkins, D. A. Haber, M. Toner, “Isolation of rare circulating tumor cells in cancer patients by microchip technology,” *Nature*, 450, 1235–1239 (2007).
- S. Nie, S. R. Emory, “Probing Single Molecules and Single Nanoparticles by Surface-Enhanced Raman Scattering,” *Science*, 275, 1102-1106 (1997).
- S. Oladipupo, S. Hu, A. C. Santeford, J. Yao, J. Kovalski, R. V. Shohet, K. Maslov, L. V. Wang, and J. M. Arbeit, “Conditional HIF-1 induction produces multistage neovascularization with stage-specific sensitivity to VEGFR inhibitors and myeloid cell independence, ” *Blood* 117(15), 4142-4153 (2011).
- S. Oladipupo, S. Hu, J. Kovalski, J. Yao, A. C. Santeford, R. Sohn, R. V. Shohet, K. Maslov, L. V. Wang, and J. M. Arbeit, “VEGF is essential for hypoxia-inducible factor mediated neovascularization but dispensable for endothelial sprouting, ” *P NAS* 108(32), 13264-13269 (2011).
- S.-P Lin, L.V. Wang, S. L. Jacques, and F. K. Tittel, “Measurement of tissue optical properties using oblique incidence optical fiber reflectometry”, *Applied Optics* 36, 136 (1997).
- S. Riethdorf, , H. Fritsche, V. Müller, T. Rau, C. Schindlbeck, B. Rack, W. Janni, C. Coith, K. Beck, F. Jänicke, et al., “Detection of circulating tumor cells in peripheral blood of patients with metastatic breast cancer: a validation study of the CellSearch system”, *Clin. Cancer Res.* 13, 920–928 (2007)
- S. Salmaso, A. Semenzato, P. Caliceti, J. Hoebeke, F. Sonvico, C. Dubernet, and P. Couvreur, “Specific antitumor targetable beta-cyclodextrin-poly(ethylene glycol)-folic acid drug delivery bioconjugate”, *Bioconjug. Chem.* 15, 997–1004 (2004)

- S Valastyan and RA Weinberg, "Tumor metastasis molecular insights and evolving paradigms", *Cell* 147, 275-292 (2011)
- S. Wang, and P.S. Low, "Folate-mediated targeting of antineoplastic drugs, imaging agents, and nucleic acids to cancer cells", *J. Control. Release* 53, 39–48 (1998)
- S. Zheng, H. Lin, J. Q. Liu, M. Balic, R. Datar, R. J. Cote, T. C. Tai, "Membrane microfilter device for selective capture, electrolysis and genomic analysis of human circulating tumor cells," *J. Chromatogr.* 1162(2), 154–161 (2007).
- T.M. Morgan, P.H. Lange, and R.L. Vessella, "Detection and characterization of circulating and disseminated prostate cancer cells", *Front. Biosci.* 12, 3000–3009 (2007)
- T. N. Erpelding et al., "Sentinel lymph nodes in the rat: noninvasive photoacoustic and US imaging with a clinical US system", *Radiology* 256, 102 (2010).
- U. K. Sur, Resonance. "Surface-Enhanced Raman Spectroscopy: Recent Advancement of Raman Spectroscopy", *Resonance*, 154- 164(2010)
- V. Dixit, J. Van den Bossche, D.M. Sherman, D.H. Thompson, and R.P. Andres, "Synthesis and grafting of thioctic acid- PEG-folate conjugates onto Au nanoparticles for selective targeting of folate receptor-positive tumor cells", *Bioconjug. Chem.* 17, 603–609 (2006)
- V. E. Gusev and A. A. Karabutov, *Laser Optoacoustics* (American Institute of Physics, New York, 1993)
- V. Müller, N. Stahmann, S. Riethdorf, T. Rau, T. Zabel, A. Goetz, F. Jänicke, and K. Pantel, "Circulating tumor cells in breast cancer: correlation to bone marrow micrometastases, heterogeneous response to systemic therapy and low proliferative activity", *Clin. Cancer Res.* 11, 3678–3685 (2005)
- V. P. Zharov, E. I. Galanzha, E. V. Shashkov, N. G. Khlebtsov, and V. V. Tuchin, "*In vivo* photoacoustic flow cytometry for monitoring of circulating single cancer cells and contrast agents," *Opt. Lett.* 31(24), 3623-3625 (2006).
- W. A. Henne, D. D. Doorneweerd, A. R. Hilgenbrink, S. A. Kularatne, and P. S. Low, "Synthesis and activity of a folate peptide camptothecin prodrug", *Bioorganic & Medicinal Chemistry Letters*, 16, 5350–5355 (2006)
- WA Kalender, W Seissler, E Klotz, P Vock, "Spiral volumetric CT with single-breathhold technique, continuous transport, and continuous scanner rotation", *Radiology*, 176(1), 181–183 (1990)
- WF Cheng, CN Lee, JS Chu, et al., "Vascularity index as a novel parameter for the *in vivo* assessment of angiogenesis in patients with cervical carcinoma", *Cancer*, vol 85, 651-657 (1999)

- WF Cheng, TM Chen, CA Chen, et al., “Clinical application of intratumoral blood flow study in patients with endometrial carcinoma”, *Cancer* 82, 1881-1886 (1998)
- W. He, H. Wang, L.C. Hartmann, J.X. Cheng, and P.S. Low, “*In vivo* quantitation of rare circulating tumor cells by multiphoton intravital flow cytometry”, *Proc. Natl. Acad. Sci. USA*, 104, 11760–11765 (2007)
- W.J. Allard, J. Matera, M.C. Miller, M. Repollet, M.C. Connelly, C. Rao, A.G. Tibbe, J.W. Uhr, and L.W. Terstappen, “Tumor cells circulate in the peripheral blood of all major carcinomas but not in healthy subjects or patients with nonmalignant diseases”, *Clin. Cancer Res.* 10, 6897–6904 (2004)
- W. Risau, “Mechanisms of angiogenesis”, *Nature* 386, 671–674 (1997)
- W. Shi, P. Hajireza, P. Shao, A. Forbrich, and R. J. Zemp, “*In vivo* near-realtime volumetric optical-resolution photoacoustic microscopy using a high-repetition-rate nanosecond fiber-laser”, *Opt. Express*, vol 19, 17143(2011).
- W. Shi, P. Shao, P. Hajireza, A. Forbrich, and R. J. Zemp, “*In vivo* dynamic process imaging using real-time optical-resolution photoacoustic microscopy”, *J. Biomed. Opt.*, vol 18, 026001 (2013)
- W. Shi, P. Shao, R. J. Paproski, A. Forbrich, R. Moore, and R. J. Zemp, “Multimodality photoacoustic and Raman imaging of magnetically-trapped tumor cells”, *Proc. SPIE* 8943, 894367 (SPIE Photonics West, San Francisco, 2014).
- W. Shi, P. Shao, and R. J. Zemp, “Investigation of Photoacoustic Signal Strength as a Function of Scan-Speed and Laser-Repetition-Rate”, 2013 Joint UFFC, EFTF and PFM Symposium, 1534 (Prague, 2013).
- W. Shi, R. J Paproski, R. Moore, and R. J. Zemp, “Detection of circulating tumor cells using targeted surface-enhanced Raman scattering nanoparticles and magnetic enrichment”, *Journal of Biomedical Optics* 19(5), 056014 (2014)
- W. Shi, S. Kerr, I. Utkin, J. C. Ranasinghesagara, L. Pan, Y. Godwal, R. J. Zemp, and R. Fedosejevs, “Optical resolution photoacoustic microscopy using novel high-repetition-rate passively Q-switched microchip and fiber lasers”, *J. Biomed. Opt.* 15, 056017(2010).
- W. W. Li, “Tumor Angiogenesis: Molecular Pathology, Therapeutic Targeting, and Imaging”, *Acad Radiol*, vol 7, 800-811 (2000)
- X.B. Zhao, and R.J. Lee, “Tumor-selective targeted delivery of genes and antisense oligodeoxyribonucleotides via the folate receptor”, *Adv. Drug Deliv. Rev.* 56, 1193–1204(2004)
- X. D. Wang, Y. J. Pang, G. Ku, X. Y. Xie, G. Stoica, and L.-H. V. Wang, “Noninvasive laser-induced photoacoustic tomography for structural and functional *in vivo* imaging of the brain”, *Nat. Biotechnol.*, vol 21, 803-806 (2003).

- X. Michalet, F. F. Pinaud, L. A. Bentolila, J. M. Tsay, S. Doose, J. J. Li, G. Sundaresan, A. M. Wu, S. S. Gambhir, S. Weiss, “Quantum Dots for Live Cells, *in vivo* Imaging, and Diagnostics”, *Science*. 307, 538-544(2005)
- X. Q. Pan, X. Zheng, G. Shi, H. Wang, M. Ratnam, and R. J. Lee, “Strategy for the treatment of acute myelogenous leukemia based on folate receptor beta-targeted liposomal doxorubicin combined with receptor induction using all-trans retinoic acid”, *Blood*, 100, 594–602 (2002)
- X. Wang, Y. J. Pang, G. Ku, X. Y. Xie, G. Stoica, and L.-H. V. Wang, “Noninvasive laser-induced photoacoustic tomography for structural and functional *in vivo* imaging of the brain”, *Nat. Biotechnol.*, vol 21, 803-806 (2003).
- X. Wang, X. Qian, J. J. Beitler, G. Chen, F. R. Khuriel, M. M. Lewis, H. J. C. Shin, S. Nie, D. M. Shin, “Detection of Circulating Tumor Cells in Human Peripheral Blood using Surface-Enhanced Raman Scattering Nanoparticles,” *Cancer Res.*, 71(5), 1526–1532 (2011).
- Y. Bae, W. D. Jang, N. Nishiyama, S. Fukushima, and K. Kataoka, “Multifunctional polymeric micelles with folate-mediated cancer cell targeting and pH-triggered drug releasing properties for active intracellular drug delivery”, *Mol. Biosyst.* 1, 242–250 (2005)
- Y. Lu, E. Segal, C. P. Leamon, and P. S. Low, “Folate receptor-targeted immunotherapy of cancer: mechanism and therapeutic potential”, *Advanced Drug Delivery Reviews*, 56, 1161–1176 (2004)
- Y. Lu, and P. S. Low, “Folate-mediated delivery of macromolecular anticancer therapeutic agents”, *Adv. Drug Deliv. Rev.* 54, 675–693 (2002)
- Y. Lu, and P. S. Low, “Folate targeting of haptens to cancer cell surfaces mediates immunotherapy of syngeneic murine tumors”, *Cancer Immunology and Immunotherapy*, 51, 153–162 (2002)
- Y. N. Billeh, M. Y. Liu, and T. Buma, “Multispectral photoacoustic microscopy using a photonic crystal fiber super-continuum source”, *Proc. SPIE*, Vol. 7564, 75642T (2010).
- Y. N. Billeh, M. Liu, and T. Buma, “Spectroscopic photoacoustic microscopy using a photonic crystal fiber supercontinuum source”, *Opt. Express* 18, 18519-18524 (2010).
- Y. Wang, K. Maslov, Y. Zhang, S. Hu, L. Yang, Y. Xia, J. Liu, and L. H. V. Wang, “Fiber-laser-based photoacoustic microscopy and melanoma cell detection”, *J. Biomed. Opt.*, vol 16, 011014 (2011)
- Zanetti-Dällenbach, R., E. Wight, A. X. Fan, O. Lapaire, S. Hahn, W. Holzgreve, and X. Y. Zhong, “Positive correlation of cell-free DNA in plasma/ serum in patients with malignant and benign breast disease”, *Anticancer Res.* 28:921–925 (2008)
- Z. X. Xie, S. L. Jiao, H. F. Zhang and C. A. Puliafito, “Laser-scanning optical-resolution photoacoustic microscopy”, *Opt. Lett.* 34, 1771-1773 (2009)

Z. Zhang, J. Jia, Y. Lai, et al., “Conjugating folic acid to gold nanoparticles through glutathione for targeting and detecting cancer cells”, *Bioorg. Med. Chem.* 18, 5528–5534 (2010)